Beauty in photoproduction at HERA II with the ZEUS detector

Sarah Boutle
University College London
August 2009

PhD thesis

Thesis submitted to University College London
in fulfilment of the requirements for the award of
the degree of Doctor of Philosophy

I, Sarah Boutle confirm that the work presented in this thesis is my own. Where information has been derived from other sources, I confirm that this has been indicated in the thesis.

Abstract

The production of beauty quarks in ep collisions should be accurately calculable in perturbative Quantum Chromodynamics (QCD) since the large mass of the b quark provides a hard scale. Therefore it is interesting to compare such predictions to results using photoproduction events where a low-virtuality photon, emitted by the incoming lepton, collides with a parton from the incoming proton. A measurement of beauty in photoproduction has been made at HERA with the ZEUS detector using an integrated luminosity of 126 pb^{-1}. Beauty was identified in events with a muon in the final state by using the transverse momentum of the muon relative to the closest jet. Lifetime information from the silicon vertex detector was also used; the impact parameter of the muon with respect to the primary vertex was exploited to discriminate between signal and background. Cross sections for beauty production as a function of the muon and the jet variables were measured and compared to QCD predictions and to previous measurements. The data were found to be well described by the predictions from next-to-leading-order QCD. The dijet sample of beauty photoproduction events was also used to study higher-order QCD topologies. At leading order, the two jets in the event are produced back-to-back in azimuthal angle, such that $\Delta\phi^{jj} = \phi^{j1} - \phi^{j2} = \pi$. Additional soft radiation causes small azimuthal decorrelations, whilst $\Delta\phi^{jj}$ significantly lower than π is evidence of additional hard radiation. In this thesis, the cross section versus $\Delta\phi^{jj}$ for beauty photoproduction and the comparison to NLO QCD predictions and Monte Carlo models are presented.

To my parents

Outline

An analysis of beauty production in ep collisions at HERA is presented in this thesis. The measurement used data collected in 2005 using the ZEUS detector and is published in [1]. In chapter 1 a theoretical overview of ep scattering and the processes under study in this thesis is given. Chapter 2 begins with a description of theoretical calculations of beauty production and then moves on to give a summary of previous relevant experimental results. The HERA collider and the ZEUS detector are described in chapter 3. In chapter 4, the reconstruction of the event objects to be used in this analysis is described while chapter 5 describes how interesting events were selected. Chapter 5 also describes the Monte Carlo samples used. Chapter 6 gives details of the analysis method used to identify beauty events and, finally, the results are given in chapter 7.

Contents

List of Figures

List of Tables

Chapter 1

Quantum chromodynamics and ep scattering

Quantum Chromodynamics (QCD) is the theory of the strong interaction, a fundamental force which governs the interactions of particles which possess colour charge known as quarks and gluons, the constituents of hadrons such as protons or neutrons. The strength of the interaction, characterised by the strong coupling constant, α_s, increases with distance, a phenomenon known as asymptotic freedom. As a consequence, quarks can only exist in bound states, a property known as colour confinement.

Studying ep scattering at HERA provides a good means by which to test the theory of QCD. For large momentum transfer, it is possible to calculate QCD processes accurately using a perturbative expansion in α_s. This large momentum transfer is known as a hard scale which can also be defined as the transverse energy of a jet or the mass of a heavy quark. The measurements made can therefore be used to verify predictions made by such calculations.

1.1 Electron proton scattering

The interaction of an electron and a proton at leading order (LO) occurs with the exchange of a photon, through the electromagnetic force, or a $Z^0/W^{\pm}$ boson, through the weak force. Such interactions can be classified into 2 types: neutral and charged current processes which are mediated by the photon/Z^0 and $W^{\pm}$ respectively and are shown in Fig. 1.1.

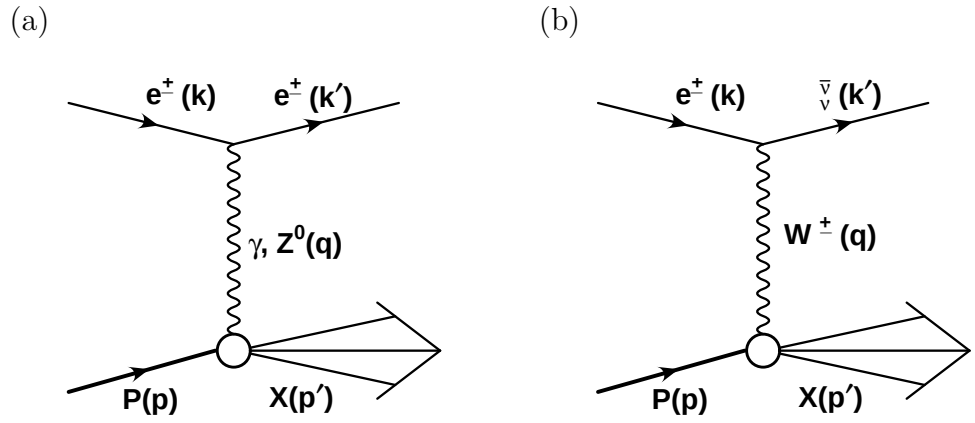

Figure 1.1: (a) Neutral current and (b) charged current interactions.

We can define the kinematics of such processes using the four-momenta of the incoming and the scattered lepton, k and k', and the four-momenta of the proton, P, and the exchanged boson, $q = k' - k$. The scattering process can therefore be described by the following quantities:

$$Q^2 = -q^2 = (k - k')^2, \tag{1.1}$$

$$y = \frac{P \cdot q}{P \cdot k}, \tag{1.2}$$

$$x = \frac{Q^2}{2P \cdot q}. \tag{1.3}$$

Q^2 is the virtuality of the exchanged boson and can be seen as a measure of the resolving power of the probe where larger values of Q^2 can resolve smaller objects. The variables y and x are the Bjorken scaling variables where y is the fraction of the lepton energy which is transferred to the interaction in the rest frame of the proton and x is the fraction of the proton momentum carried by the struck quark. These quantities are related to the square of the centre of mass energy, s, by:

$$Q^2 = sxy. \tag{1.4}$$

For $Q^2 \gg \Lambda_{QCD}$ where $\Lambda_{QCD} \simeq 0.2$ GeV, the scale is provided by Q^2 itself and so perturbative calculations can be performed. These events are known as Deep Inelastic Scattering (DIS) events.

When $Q^2 \sim 0$ GeV^2, the electron scatters through a very small angle and the boson exchanged is an almost real photon. This process is referred to as photoproduction. In this case, Q^2 cannot be used to define a hard scale and so quantities such as the transverse momentum of the jet or the mass of the quark, as in heavy quark production, can be used so that measurements can be compared to theoretical calculations.

1.2 The quark parton model

In the quark parton model, the proton is assumed to be composed of point-like free objects called partons. In this way, the inelastic electron-proton scattering process can be described in terms of the elastic scattering of the electron with a parton, i, and the probability, $f_i(x)$ of finding this parton with momentum, x, inside the proton, known as the Parton Distribution Function (PDF).

The neutral current cross section is given by

$$\frac{d\sigma^2}{dQ^2dx} = \frac{4\pi\alpha^2}{xQ^4}\left[\frac{y^2}{2}2xF_1 \mp (1-(1-y)^2)F_2 \mp \left(y - \frac{y^2}{2}\right)xF_3\right], \tag{1.5}$$

and using $F_L = F_2 - 2xF_1$,

$$\frac{d\sigma^2}{dQ^2dx} = \frac{2\pi\alpha^2}{xQ^4}[Y_+F_2 - y^2F_L \mp Y_-xF_3], \tag{1.6}$$

where $Y_\pm = 1 \pm (1-y)^2$. F_2 is the structure function describing neutral current scattering, F_L describes the coupling to longitudinally polarised photons and F_3 is the parity violation structure function which arises from Z^0 exchange. The $\mp$ sign of last term in Equation 1.6 corresponds to the case where the initial lepton is either a positron (-) or and electron (+). It was predicted [4] that, in the limit $Q^2 \to \infty$ and $P \cdot q \to \infty$ (but their ratio $Q^2/P \cdot q$ does not tend to infinity) the structure functions would depend only on x such that:

$$F_1(Q^2, x) = F_1(x) = \frac{1}{2}\sum_i e_i^2 f_i(x), \tag{1.7}$$

$$F_2(Q^2, x) = F_2(x) = \sum_i e_i^2 x f_i(x), \tag{1.8}$$

where e_i is the charge on the parton. This prediction is known as Bjorken scaling and was verified experimentally at SLAC [5] confirming the presence of charged constituents in the proton. Comparing the two expressions yields the Gallan-Cross relation:

$$F_2(x) = 2xF_1(x), \tag{1.9}$$

which is a consequence of the charged constituents carrying spin-1/2 and results in F_L being zero. The experimental verification of these predictions identified the partons as quarks and hence the model is known as the Quark Parton Model.

1.3 The improved parton model

If the proton were composed only of charged particles then the sum of their momenta would equal the proton momentum, i.e. the sum of their fractional momenta would be unity:

$$\sum_i \int_0^1 dx f_i(x) x = 1. \tag{1.10}$$

Experimentally, quarks were found to constitute only $\sim 50\%$ of the proton's momentum [6] suggesting that neutral particles also existed in the proton. These were identified as gluons and direct evidence of their existence was observed in e^+e^- collisions in the form of 3-jet events [7]. The modification of the quark parton model to include gluons formed what became QCD.

In QCD, the proton can be described as a dynamical system of quarks and gluons. Gluons can be emitted and absorbed by the quarks and can split to produce pairs of quarks or gluons. In this way it is possible for a parton to gain transverse momentum relative to the proton direction leading to the violation of the Gallan-Cross relation and a non-zero value of F_L.

Because of this gluon radiation, the structure function F_2 has a dependence on Q^2 as well as on x as shown in Fig. 1.2. In low Q^2 events the photon can resolve the valence quark substructure of the proton whereas in high Q^2 events more and more partons can be resolved. As Q^2 increases there is a decreased probability of finding a quark at large x values because high-momentum quarks would lose momentum by radiating gluons. So for large values of x the value of F_2 decreases as a function of Q^2. Consequently there is an increased probability of finding a quark at low x and so here F_2 rises as a function of Q^2. This behaviour of the structure function is known as scaling violation and can be clearly seen in Fig. 1.2 [8].

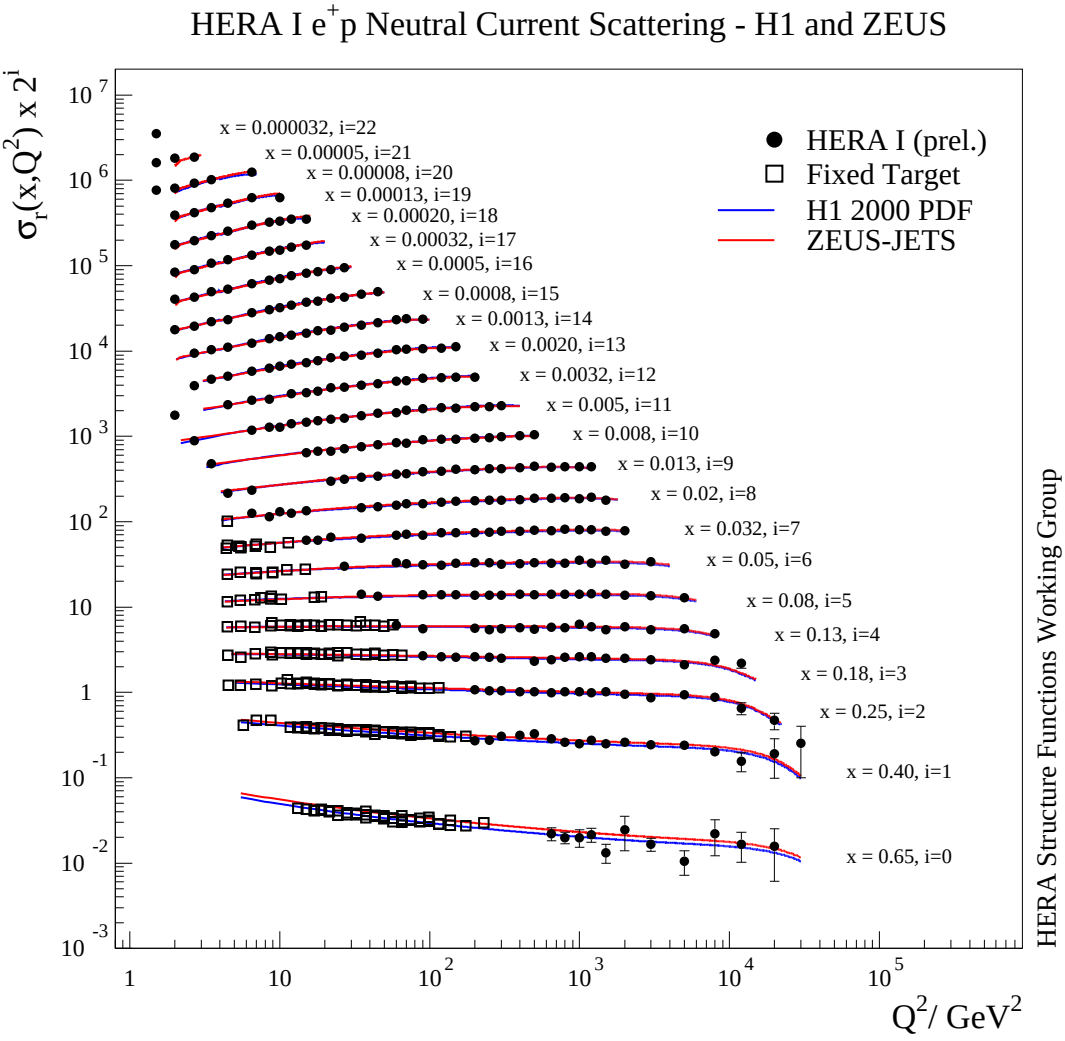

Figure 1.2: The reduced cross section $\sigma_r(x, Q^2)$ as a function of Q^2 for fixed values of x. Results from fixed target experiments and the combined ZEUS-H1 HERA I measurements are compared to an NLO QCD fit from each of the experiments, H12000PDF and ZEUS-JETS.

1.4 Evolution of parton densities

Although the precise mathematical form of PDFs cannot be calculated from first principles, a functional form can be postulated and then used to fit experimental data. A functional form of the dependence of the structure functions on $\log Q^2$ can be found by incorporating a term due to gluon emission into equation 1.8:

$$\frac{F_2(Q^2,x)}{x} = \sum_i e_i^2 \left(q_i(x) + \frac{\alpha_s}{2\pi} \log \frac{Q^2}{\mu^2} \int_x^1 \frac{dy}{y} q_i(y) P_{qq}\left(\frac{x}{y}\right) \right), \tag{1.11}$$

where $q_i = f_i$, the quark structure function and μ is an appropriate scale, typically chosen to avoid singularities when transverse momentum squared tends to zero. $P_{qq}\left(\frac{x}{y}\right)$ is known as the splitting function which is the probability of a quark with momentum y emitting a gluon and emerging with momentum x. Predictions of the structure function which have been measured at one experiment can be used at another, as long as it is evolved to the correct scale. Given some reference value of the quark density, the evolution of q_i with $\log Q^2$ can be calculated as:

$$\frac{dq_i(x,Q^2)}{d\log Q^2} = \frac{\alpha_s}{2\pi} \int_x^1 \frac{dy}{y} q_i(y,Q^2) P_{qq}\left(\frac{x}{y}\right). \tag{1.12}$$

In addition, there can be a contribution to the quark density from quarks produced in a pair originating from a gluon, modifying Equation 1.12 to give:

$$\frac{dq_i(x,Q^2)}{d\log Q^2} = \frac{\alpha_s}{2\pi} \int_x^1 \frac{dy}{y} \left[q_i(y,Q^2) P_{qq}\left(\frac{x}{y}\right) + g(y,Q^2) P_{qg}\left(\frac{x}{y}\right) \right], \tag{1.13}$$

where $g(y,Q^2)$ is the gluon density function. Similarly, the gluon density evolution equations can be found using the same procedure:

$$\frac{dg(x,Q^2)}{d\log Q^2} = \frac{\alpha_s}{2\pi} \int_x^1 \frac{dy}{y} \left[\sum_i q_i(y,Q^2) P_{gq}\left(\frac{x}{y}\right) + g(y,Q^2) P_{gg}\left(\frac{x}{y}\right) \right]. \tag{1.14}$$

Equations 1.13 and 1.14 are called the DGLAP equations [9] and are used to describe the evolution of the parton densities. The terms P_{ij} are the splitting functions for the processes shown in Fig. 1.3 and can be interpreted as the probability of a parton j with momentum fraction y emitting a parton and emerging with momentum fraction x.

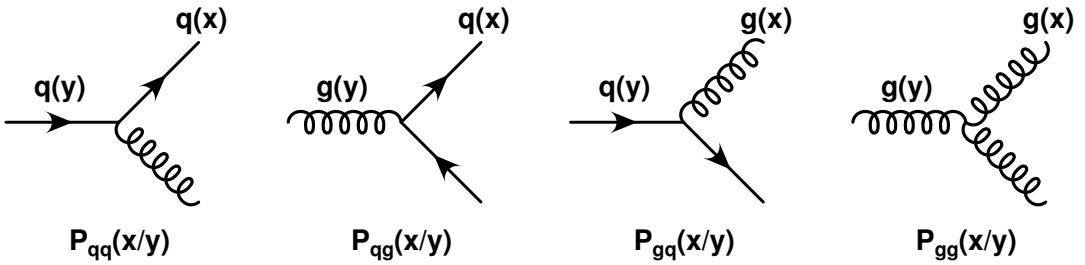

Figure 1.3: The first order splitting functions P_{ij} used in the DGLAP equations.

The DGLAP equations are valid at high Q^2 and high x but not at low x where $\log\left(\frac{1}{x}\right)$ terms become important.

1.5 Photoproduction

As mentioned in Sec. 1.1, for $Q^2 \sim 0$ GeV^2 the electron scatters through a very small angle emitting an almost real photon. This is known as photoproduction. For these low-virtuality processes the average lifetime of the photon appears to be long with respect to the characteristic time of the hard scattering process. Hence we can think of this process as photon-proton scattering due to the exchange of a virtual photon and the ep cross section can be expressed in terms of the γp cross section by the Equivalent Photon Approximation (EPA). When $Q^2 \to 0$, the longitudinal component of $\sigma_{tot}^{\gamma p}$ can be neglected and we can write

$$\frac{d^2\sigma^{ep}}{dydQ^2} = f_{e\to\gamma}^{T}(y, Q^2)\sigma_{tot}^{\gamma p}(y, Q^2), \tag{1.15}$$

where $f_{e\to\gamma}^{T}(y, Q^2)$, the probability of finding a transverse polarised photon in the electron of energy $E_\gamma = yE_e$, is given by:

$$f_{e\to\gamma}^{T}(y, Q^2) = \frac{\alpha}{2\pi}\left(\frac{1+(1-y)^2}{y}\frac{1}{Q^2} - 2\frac{(1-y)}{y}\frac{Q_{min}^2}{Q^4}\right), \tag{1.16}$$

using the Weizsäcker-Williams approximation [10]. In the above equation Q_{min}^2 represents the lower kinematic limit and is given by:

$$Q_{min}^2 = \frac{m_e^2 y^2}{(1-y)}. \tag{1.17}$$

The photon can be considered to have structure. In photoproduction, the photon's lifetime is long enough that it can fluctuate into quark-antiquark pairs. This means that the photon can behave as a source of partons and can be treated with the same formalism as hadron-hadron scattering. Hence $\gamma\gamma$ processes in e^+e^- scattering can be treated as deep inelastic $e\gamma$ scattering for the case where one photon is almost real and one is virtual. The cross section for this process is given by

$$\frac{d\sigma^2_{e\gamma\to eX}}{dQ^2dx} = \frac{2\pi\alpha^2}{Q^4}[(1+(1-y)^2)F_2^\gamma - y^2F_L^\gamma], \tag{1.18}$$

where, in analogy to the proton structure function, we define a photon structure function, F_2^γ. This is given by

$$F_2^\gamma(Q^2,x) = 2x\sum_i e_{q_i}^2\, q_i(Q^2,x), \tag{1.19}$$

where $q_i(Q^2,x)$ are the quark densities in the photon summed over the all the quark flavours of charge e_{q_i}.

1.6 Direct and resolved photon processes

In leading order QCD, γp interactions can be classified into two types of process known as direct and resolved photoproduction. In direct photoproduction, the photon behaves as a point-like object and couples directly to a parton in the proton. Whereas in resolved photoproduction, the photon acts as a source of partons, one of which takes part in the hard scatter. The LO direct photoproduction diagrams and examples of resolved processes can be seen in Fig. 1.4. QCD compton scattering, in Fig. 1.4(a), is the coupling of the photon with a quark in the proton which then radiates a gluon. Figure 1.4(b) shows a gluon in the proton splitting to produce a quark-antiquark pair. The quark then couples with the photon. This is known as boson-gluon fusion. In both of the LO direct photon processes the final state consists of a scattered lepton, proton remnant and two high-transverse momentum jets: a gluon and a quark jet in the case QCD compton scattering and two quark jets in the case of boson-gluon fusion.

In the examples of resolved photon processes shown in Fig. 1.4, a gluon in the proton interacts with a quark or gluon in the photon producing a final state of a gluon and a quark jet or two quark jets. This is similar to the final state of direct photon events except that there will be, in addition, a photon remnant. In direct events all of the photon energy is involved in the hard subprocess and so they are expected to be characterised by a higher final-state transverse momentum compared

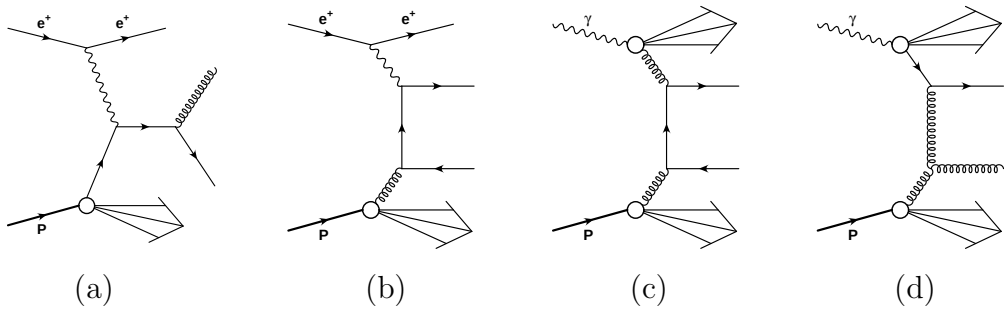

Figure 1.4: Leading order direct ((a) and (b)) and examples of resolved ((c) and (d)) photoproduction processes.

to resolved photon interactions in which only a fraction of the photon energy participates in the hard scatter.

In LO QCD, direct and resolved photoproduction are distinct and well-defined processes. However it should be noted that at higher orders the distinction between the two becomes ambiguous. The contributions of the two processes in the photoproduction of jets were studied [11] in a comparison to fixed target experiments. It was found that the resolved component was small. At HERA, where the resolved contribution to the cross section was larger, the observation of resolved photon processes was possible through the observation of large energy deposits in the electron direction consistent with a photon remnant [12]. Moreover a distinction between the two components was made [13] and an experimental separation based on the fraction of photon energy participating in the interaction, x_γ, can be defined as

$$x_\gamma = \frac{\sum_i E_T^i e^{-\eta^i}}{2yE_e}, \tag{1.20}$$

summed over the outgoing partons where yE_e is the initial photon energy. For direct photon events $x_\gamma = 1$ whereas for resolved photon events $x_\gamma < 1$. Translating this into an experimentally observable quantity, x_γ^{obs} [14], the sum is made over the jets instead of over the partons:

$$x_\gamma^{obs} = \frac{\sum_{j=j1,j2} E_T^j e^{-\eta^j}}{2yE_e}, \tag{1.21}$$

where $j1$ and $j2$ are the two highest-E_T jets, where E_T is the transverse component of the energy with respect to the z-axis. Due to hadronisation effects, the value of x_γ^{obs} is no longer exactly unity for direct photon events but rather populates the high-x_γ^{obs} region. An experimental cut-off is used

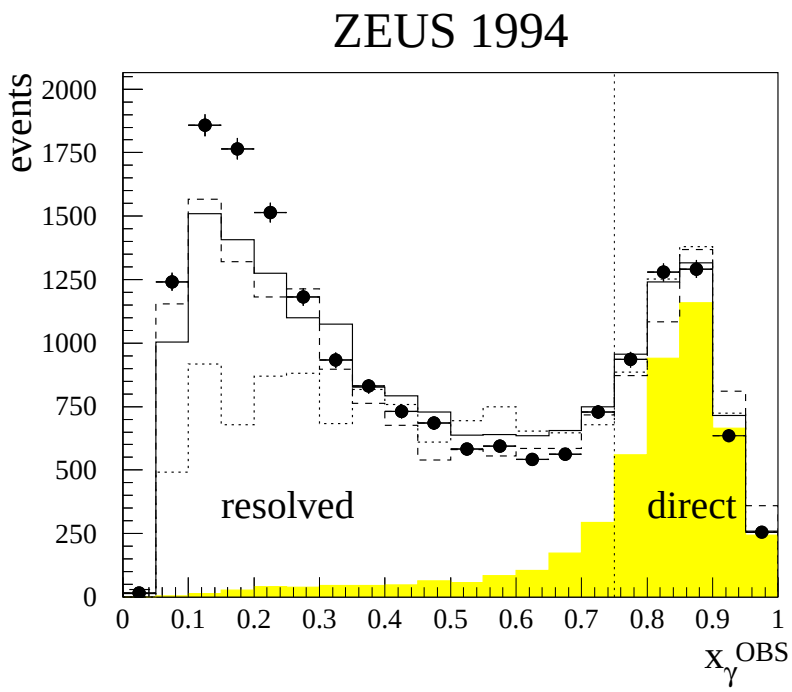

Figure 1.5: Distribution of x_γ^{obs} in dijet events for ZEUS data compared with HERWIG with (solid line) and without (dotted line) the inclusion of a model for multi-parton interactions (MPI) and also compared to PYTHIA with MPI (dashed line). The shaded area represents the direct photon events generated by HERWIG. Also shown is a vertical line which defines the experimental distinction between direct and resolved photon events.

to define event samples enriched in direct and resolved photon events. An event is said to be a direct photon process for values of $x_\gamma^{obs} \geq 0.75$ and a resolved photon process when $x_\gamma^{obs} < 0.75$. Figure 1.5 shows Monte Carlo simulations of the two types of process fitted to data and also the experimental cut-off [15].

Chapter 2

Beauty production

2.1 Photoproduction of heavy quarks at HERA

The production of heavy quarks, namely of charm and beauty, gives rise to an additional hard scale in perturbative calculations, that of the mass of the quark, and so should be accurately calculable in perturbative QCD. Heavy quark production measurements therefore provide a good means by which to test such calculations. With the large mass of the beauty quark compared to that of the charm quark, $m_b \sim 3m_c$, even greater reliability is ensured in QCD calculations for beauty production. At HERA, heavy quarks are produced predominantly, at LO, through boson-gluon fusion

$$\gamma g \rightarrow Q\bar{Q}, \tag{2.1}$$

since their large mass leads to their suppression in the quark-gluon sea in the proton. In resolved photoproduction at LO, it is necessary to consider not only gluon-gluon fusion,

$$gg \rightarrow Q\bar{Q}, \tag{2.2}$$

but also contributions in which the photon splits to a $Q\bar{Q}$ pair, one of which takes part in the hard scatter, for example:

$$Qg \rightarrow Qg. \tag{2.3}$$

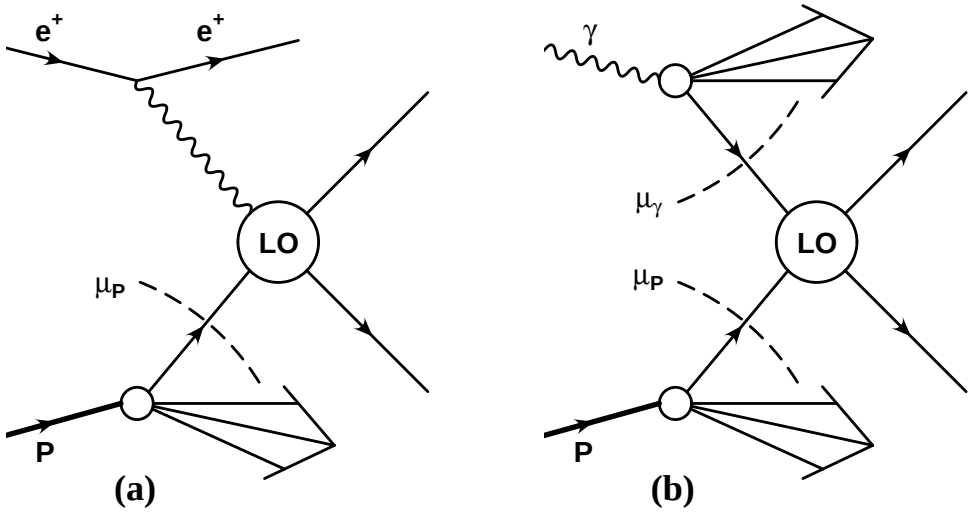

Figure 2.1: General diagrams for (a) direct and (b) resolved photoproduction.

At LO, both direct and resolved processes contribute to heavy quark photoproduction. The relative contributions of direct and resolved processes and, in fact, the definition of what constitutes a LO resolved process or a next-to-leading order (NLO) direct process can differ in theoretical models.

Figure 2.1 shows the general diagrams for LO direct and resolved processes. The dashed lines represent the separation between the hard scattering process which can be perturbatively calculated and the non-perturbative part of the interactions which are described by the PDFs. The factorisation scales μ_p and μ_γ are chosen arbitrarily to allow the parton a large phase space in which to evolve, typically $\mu_p = \mu_\gamma = \mu \sim E_T$. At NLO there are also diagrams involving a $2 \rightarrow 3$ parton scattering process. The distinction of $2 \rightarrow 3$ processes at NLO and those which are simply LO processes depends on the value of μ. Therefore, by considering NLO instead of LO the dependence on the choice of μ in a calculation is reduced.

2.2 Perturbative formalism of the photoproduction of heavy quarks

The total cross section for inclusive photoproduction of heavy quark, Q, at $\mathcal{O}(\alpha_s^2\alpha)$ [16], i.e. for:

$$\gamma + H \rightarrow Q + X, \tag{2.4}$$

at a photon-hadron centre-of-mass energy, S, is given by the sum of the direct and resolved diagrams:

$$\sigma(S) = \sum_j \int dx \hat{\sigma}_{\gamma j}(xS, m^2, \mu^2) F_j^H + \sum_{i,j} \int dx_1 dx_2 \hat{\sigma}_{ij}(x_1 x_2 S, m^2, \mu^2) F_i^\gamma(x_1, \mu) F_j^H(x_2, \mu), \quad (2.5)$$

where F_j^H and F_i^γ are the proton and photon parton densities and μ is the factorisation scale. The $\hat{\sigma}$s represent the perturbatively calculable $2 \to 2$ scattering matrix element. The γ-parton cross section is given by:

$$\hat{\sigma}_{\gamma j}(s, m^2, \mu^2) = \frac{\alpha \alpha_s(\mu^2)}{m^2} f_{\gamma j}(\rho, \frac{\mu^2}{m^2}), \quad (2.6)$$

where $\rho = \frac{4m^2}{s}$ and s is the partonic centre-of-mass energy and the function $f_{\gamma j}$ can be expanded perturbatively as,

$$f_{\gamma j}(\rho, \frac{\mu^2}{m^2}) = f_{\gamma j}^{(0)}(\rho) + g^2(\mu^2) \left[f_{\gamma j}^{(1)}(\rho) + \bar{f}_{\gamma j}^{(1)}(\rho) \log \left(\frac{\mu^2}{m^2} \right) \right] + \mathcal{O}(g^4), \quad (2.7)$$

where g is the coupling strength ($\alpha_s = \frac{g^2}{4\pi}$). In Equation 2.5, the second term can be considered to be analogous to hadroproduction [17] but with the proton parton density replaced by the photon parton density and the parton-parton cross section, $\hat{\sigma}_{ij}$, is given by:

$$\hat{\sigma}_{ij}(s, m^2, \mu^2) = \frac{\alpha_s(\mu^2)}{m^2} f_{ij}(\rho, \frac{\mu^2}{m^2}). \quad (2.8)$$

In a similar way to $f_{\gamma j}$, the function f_{ij} can be written as a perturbative expansion:

$$f_{ij}(\rho, \frac{\mu^2}{m^2}) = f_{ij}^{(0)}(\rho) + g^2(\mu^2) \left[f_{ij}^{(1)}(\rho) + \bar{f}_{ij}^{(1)}(\rho) \log \left(\frac{\mu^2}{m^2} \right) \right] + \mathcal{O}(g^4). \quad (2.9)$$

Further details on the functions $f_{\gamma j}$ and f_{ij} can be found in [16] and [17]. The perturbative expansions shown in Equations 2.7 and 2.9 depend on the mass of the quark, m. This demonstrates that the larger the quark mass, the more reliable the perturbative expansion thus emphasizing the statement that beauty production should be accurately calculable in perturbative QCD. The above equations refer to the single particle inclusive production cross section but have been extended [18] to give exclusive cross section predictions which allow better comparisons to data.

2.3 NLO QCD photoproduction calculations

Two main schemes exist for the calculation of heavy quark cross sections in photoproduction. These are known as the "massive" and "massless" schemes. In massive calculations [19], only the gluons and three quark flavours, u, d and s, are active partons in the proton and photon PDFs. Heavy quarks are produced in the hard subprocess. Using this method, there are two resolved processes at LO:

$$gg \rightarrow Q\bar{Q},\ q\bar{q} \rightarrow Q\bar{Q}. \tag{2.10}$$

In the perturbative expansion of Sec. 2.2, it can be seen that at large p_T terms of the form $\log\left(\frac{p_T^2}{m^2}\right)$ become large and the series diverges. This method may therefore be unreliable for $p_T \gg m_Q$. In the massless scheme [20], the heavy quarks are considered to be active flavours in the proton and photon above a certain threshold. This method is valid for $p_T \gg m_Q$ where the heavy quark mass bears less relevance. At NLO, real and virtual partons can be radiated in the hard interaction which cause soft and collinear singularities. In the massless scheme, soft singularities in real and virtual corrections cancel while collinear singularities can be absorbed into the non-perturbative PDFs or perturbative fragmentation functions.

The mass of the b quark is sufficiently large that it provides an energy scale such that perturbative calculations can be made using the massive method. However if other scales such as the transverse momentum of the quark, p_T^b, or Q^2 become large enough, then a massless calculation may improve reliability. For the analysis in this thesis calculations based on the massive scheme developed by Frixione et al. [19] (FMNR) were used.

2.4 Monte Carlo simulations

So-called LO+PS Monte Carlo (MC) generators use LO matrix elements and simulate higher order effects in the leading logarithm approximation with the initial- and final-state radiation obeying the DGLAP evolution equations, which describe the way in which the quark and gluon momentum distributions in a hadron evolve with the scale of the interaction, as described in Sec. 1.4.

Monte Carlo simulations are an important tool in many particle physics analyses and essential to the analysis described in this thesis. Since a particle traversing a detector cannot ever be perfectly reconstructed some correction must be made for inefficiencies and acceptances of the measurements made. We rely on MC simulations of both physics processes and detector responses to make these

corrections. Moreover, as with the analysis described in this thesis, the separation of signal and background can be performed using MC simulations. Finally MC simulations can be used to test the predictions of the theoretical models contained within them by comparison with data.

The simulation of physics events at HERA begins with an event generator which simulates the final state of an *ep* interaction. Data produced by the event generator are then passed to a detector and trigger simulation package called MOZART which uses GEANT 3.21. At this stage, the responses of the ZEUS detector to the final state particles are simulated.

2.4.1 Event generators

In this thesis, the MC programme used is a general purpose event generator called PYTHIA which can be used to simulate the final states of a wide range of interactions. The general structure of the generation of an *ep* event is shown in Fig. 2.2 and the main stages are as follows:

- Incoming particles are described using PDFs.
- Parton showers are used to approximate initial-state radiation.
- The 2-body hard scattering process is calculated using LO matrix elements.
- The outgoing partons emit final state radiation which is described using parton showers.
- The hadronisation process is non-perturbative and so phenomenological models are used to describe it. Hadronisation is divided into the parton showering and fragmentation stages which are described in Section 2.4.2.

2.4.2 Hadronisation in PYTHIA

PYTHIA uses the Lund string model to simulate hadronisation. In the model, a colour flux tube or string joins each $q\bar{q}$ pair leaving the parton shower. The tubes have transverse dimensions of ~ 1 fm which is approximately the typical meson size. They have no p_T and are uniform along their length. As each $q\bar{q}$ pair moves apart, the colour flux tube between them is stretched until its energy density reaches that of a typical meson (~ 1 GeV/fm^3) and it is fragmented, forming a new $q\bar{q}$ pair at the break as shown in Fig. 2.3. Quantum tunnelling is responsible for the production of the new pair and so heavy flavours are suppressed. This process continues until all of the tubes are too light to undergo further fragmentation.

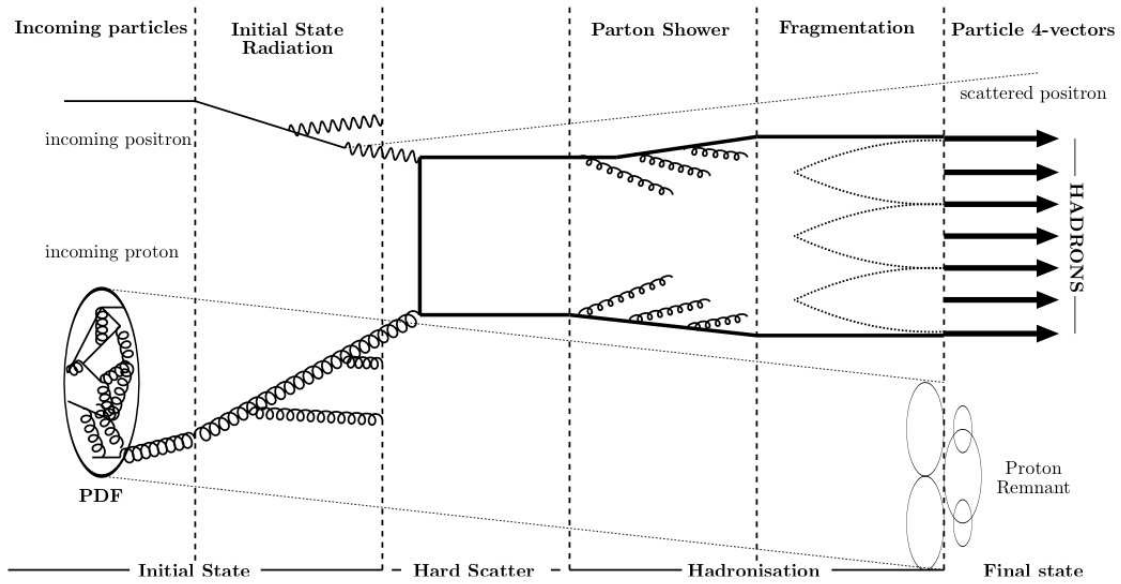

Figure 2.2: General structure of the generation of a Monte Carlo event involving a positron-proton collision.

2.5 An overview of previous measurements

In this section, an overview of previous measurements relevant to the analysis described in this thesis will be given. The most recent measurements of beauty production in collider experiments are presented, starting with some measurements of beauty in photoproduction made at HERA. Then a selection of measurements made at hadron colliders, $Sp\bar{p}S$ and the Tevatron, and in $\gamma\gamma$ collisions at LEP are summarised. Finally two ZEUS measurements, in which the correlations between jets have been studied, are presented.

2.5.1 Beauty production at HERA

Measurement of beauty photoproduction using semileptonic decays into muons

The previous ZEUS measurement [21] of beauty in photoproduction using a muon tag was carried out using data taken between 1996 and 2000. In a data sample of 110 pb^{-1}, events were selected with $Q^2 < 1$ GeV^2 and $0.2 < y < 0.8$ which contained two jets with $p_T^{j1,j2} > 7,6$ GeV and $|\eta^{j1,j2}| < 2.5$ and at least one muon with $p_T^{\mu} > 2.5$ GeV and $-1.6 < \eta^{\mu} < 2.3$. The fraction of beauty events in this sample was extracted by fitting MC distributions to the data distribution of

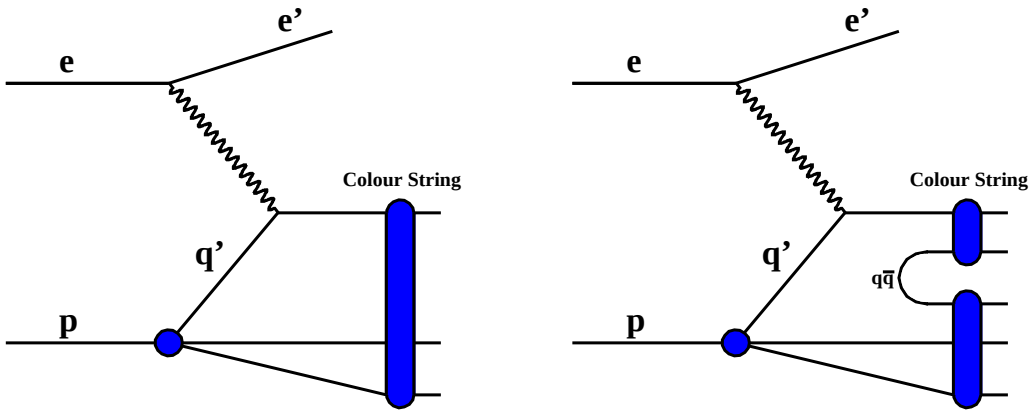

Figure 2.3: Illustration of the Lund string model in which $q\bar{q}$ pair is joined together by a colour flux tube which splits at some energy density to form a new $q\bar{q}$ pair.

the transverse momentum of the muon with respect to the jet, $p_T^{\rm rel}$. Figure 2.4 shows the differential cross sections as a function of p_T^μ and η^μ measured in the analysis. The data are compared to NLO QCD predictions from the FMNR program [19] and to PYTHIA and CASCADE MC models. The data are well described by the NLO QCD calculation and by the MC.

The H1 collaboration have also made a measurement [22] of beauty in dijet events with a muon tag. The analysis used 50 pb^{-1} of data collected in 1999 and 2000 and was made in the following kinematic region: $Q^2 < 1$ GeV^2, $0.2 < y < 0.8$, $p_T^{j1,j2} > 7,6$ GeV, $|\eta^{j1,j2}| < 2.5$, $p_T^\mu > 2.5$ GeV and $-1.6 < \eta^\mu < 2.3$. The method employed to identify beauty events was the same as for the ZEUS measurement with the addition of lifetime information in the form of the signed impact parameter variable, δ. This corresponds to the distance of the muon track from the primary vertex using precise spatial information from the H1 Silicon track detector. The long lifetime of B hadrons leads to a larger displacement than for lighter quark events. The differential cross sections as a function of η^μ and p_T^μ are shown in Fig. 2.5 compared again to NLO QCD predictions and to PYTHIA and CASCADE MC models. The shape of the η^μ distribution is well described by the QCD calculation but the p_T^μ distribution is somewhat harder in the data and the data is found to lie above the NLO QCD prediction by a factor of ~ 2.5 in the first bin.

In the above analyses, both collaborations have also measured the differential cross section as a function of x_γ^{jets}, the massive-jet analogue of x_γ^{obs} which is described in Sec. 1.6. The variable x_γ^{jets}

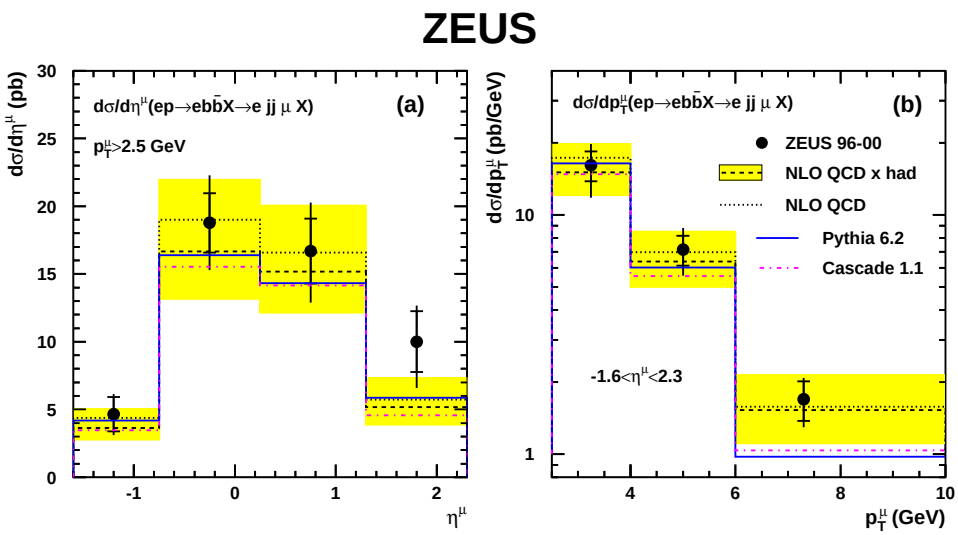

Figure 2.4: Differential cross sections as a function of pseudorapidity, η^{μ}, (left) and transverse momentum, p_T^{μ}, (right) of the muon for beauty photoproduction in dijet events, measured by the ZEUS collaboration. The data are compared to predictions from PYTHIA and CASCADE MC as well as to NLO QCD calculations with and without factors applied to correct for hadronisation effects (see Sec. 7.3).

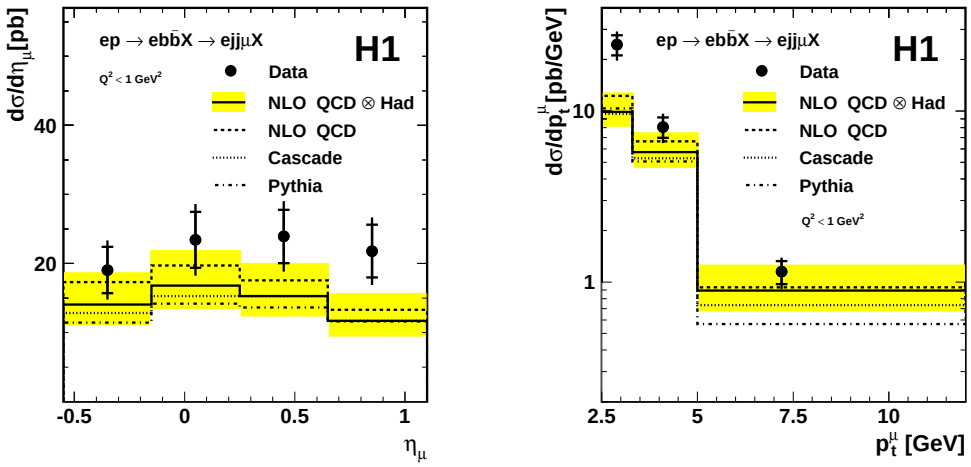

Figure 2.5: Differential cross sections as a function of pseudorapidity, η^{μ}, (left) and transverse momentum, p_T^{μ}, (right) of the muon for beauty photoproduction in dijet events, measured by the H1 collaboration. The measurements are compared to predictions from PYTHIA and CASCADE MC as well as to NLO QCD calculations with and without factors applied to correct for hadronisation effects (see Sec. 7.3).

is given by,

$$x_\gamma^{jets} = \frac{\sum_{j=1,2}(E^j - p_Z^j)}{(E - p_Z)}, \tag{2.11}$$

where E and p_Z are the total energy of the event and the momentum along the z-axis of the event respectively. Subtracting p_Z means that the contribution to the total energy of particles escaping detection along the forward beam-pipe is negligible. At LO, x_γ^{jets} estimates the fraction of the photon momentum taking part in the hard scatter and as such is a measure of the relative importance of direct ($x_\gamma^{jets} \sim 1$) and resolved ($x_\gamma^{jets} < 1$) photon processes. Figure 2.6 shows the results of these two measurements compared to NLO QCD predictions, obtained using FMNR, and PYTHIA and CASCADE MC predictions, which all describe the data reasonably well.

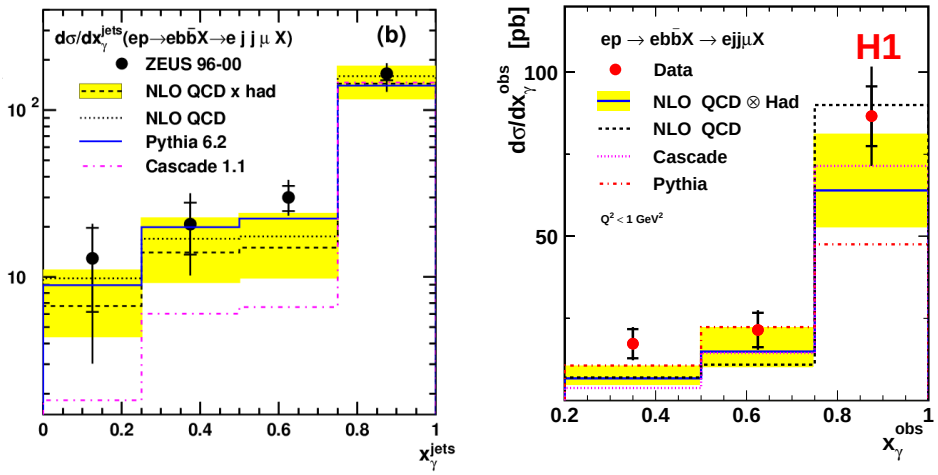

Figure 2.6: Differential cross sections as a function of x_γ^{jets} in dijet events with a muon measured by the ZEUS collaboration (left) and the H1 collaboration (right). The data are compared to predictions from PYTHIA and CASCADE MC as well as to NLO QCD calculations.

Measurement of beauty photoproduction using semileptonic decays into electrons

Beauty photoproduction has been also measured using semileptonic decays to electrons or positrons [23, 24]. Tagging electrons has the advantage that lower values of the lepton transverse momentum can be probed. In this analysis [23], based on $\mathcal{L} = 120$ pb^{-1} of HERA I data collected with the ZEUS detector from 1996 to 2000, events were selected in the photoproduction regime,

$Q^2 < 1$ GeV^2, having $0.2 < y < 0.8$, and with at least two jets with $E_T^{j1,j2} > 7,6$ GeV, $|\eta^{j1,j2}| < 2.5$ and an electron coming from the semileptonic b decay with $p_T^e > 0.9$ GeV and $|\eta^e| < 1.5$. For the identification of the electrons and the extraction of the b fraction a likelihood ratio method was used combining five discriminating variables. Three of them were used mainly for the lepton identification, and are based on the ionisation energy loss of the particle in the ZEUS central drift chamber, and on other calorimeter and tracking information. Also included were $p_T^{\rm rel}$ and the azimuthal angle between the electron and the missing transverse momentum vector, which corresponds to the neutrino from the semileptonic b decay. Figure 2.7 shows the distributions of the differential cross sections as a function of the electron transverse momentum, $d\sigma/dp_T^e$, and pseudorapidity, $d\sigma/d\eta^e$. The data are compared with the predictions of the PYTHIA MC program and with NLO QCD predictions from FMNR. The shape of the data is well described by both the MC and the NLO calculations. The NLO predictions describe the normalisation of the data within the large uncertainties.

Measurement of beauty dijet cross sections in photoproduction using inclusive lifetime tag

An inclusive measurement of beauty in dijet events in the photoproduction regime [25] has been carried out by the H1 collaboration. The analysis is based on a sample of data collected in 1999 and 2000 and corresponds to an integrated luminosity of 56.8 pb^{-1}. Photoproduction ($Q^2 < 1$ GeV^2) events with $0.15 < y < 0.8$ and two jets with $p_T^{j1,j2} > 11,8$ GeV and $-0.9 < \eta^{j1,j2} < 1.3$ were selected.

Events containing beauty quarks were distinguished from those containing only light quarks by reconstructing the impact parameter, δ, of the charged tracks. The quantities S_1 and S_2 are defined as the significance, $\delta/\sigma(\delta)$, of the track with the highest and second highest absolute significance, respectively, where $\sigma(\delta)$ is the error on δ. In order to reject most of the light quark background and to reduce the uncertainty due to the impact parameter resolution, the negative bins in the significance distributions were subtracted from the positive bins. The resulting distributions are dominated by c quark events, with a b fraction increasing towards larger significances. The light quarks contribute a small fraction for all values of significance. To extract the beauty fraction, a simultaneous χ^2-fit to the subtracted S_1 and S_2 distributions was performed. The differential cross sections as a function of the transverse momentum of the highest-p_T jet, $p_T^{jet_1}$ and the mean pseudorapidity of the two jets, $\bar{\eta}$, shown in Fig. 2.8, are extracted using the scale factors obtained from the fit. The results are compared to different MC predictions and to NLO QCD calculations. The beauty cross sections are reasonably well described in shape but the NLO QCD prediction tends to lie below the data.

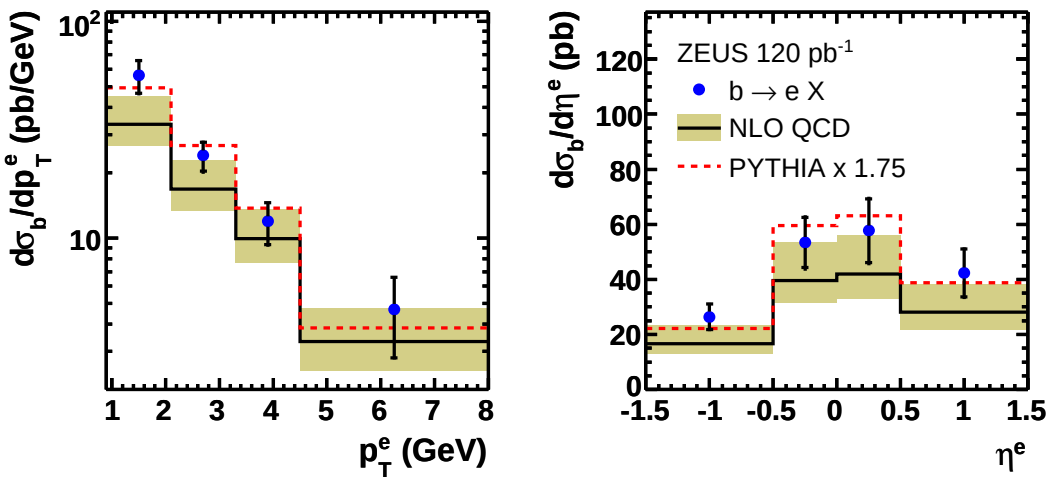

Figure 2.7: Differential cross sections as a function of the transverse momentum, p_T^e, (left) and pseudorapidity, η^e, (right) of the electron for beauty photoproduction in dijet events. The measurements are compared to the predictions from PYTHIA as well as to NLO QCD calculations corrected for hadronisation effects.

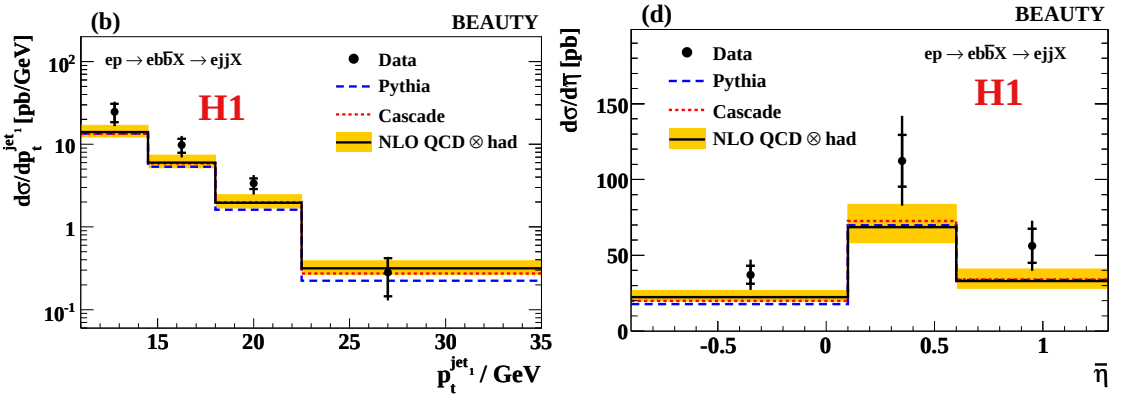

Figure 2.8: Differential beauty dijet photoproduction cross sections as a function of the transverse momentum of the leading jet, $d\sigma/dp_T^{jet_1}$, (left) and as a function of the mean pseudorapidity of the two jets, $d\sigma/d\bar{\eta}$, (right). The measurements are compared to the absolute predictions of PYTHIA and CASCADE as well as to NLO QCD calculations corrected for hadronisation effects.

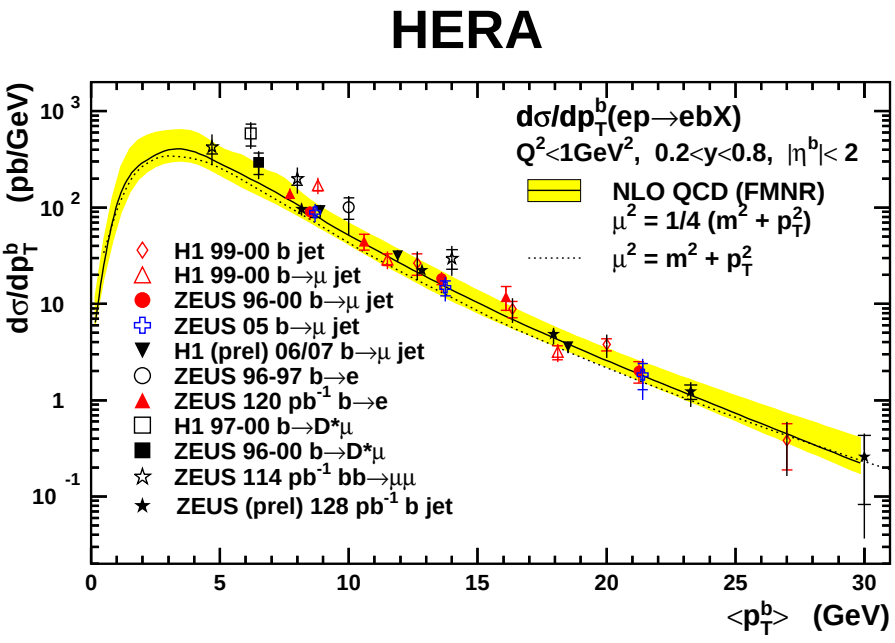

Figure 2.9: Summary of beauty photoproduction measurements at HERA. Measurements described in this section are shown in red and the analysis which forms the subject of this thesis is shown by the blue markers. The data are compared to NLO QCD predictions from the FMNR program with two different choices of scale: $\mu^2 = 1/4(m^2 + p_T^2)$ (solid line) and $\mu^2 = m^2 + p_T^2$ (dotted line).

Summary of HERA beauty production measurements

The HERA measurements of beauty photoproduction, some of which have been presented in this section, are shown together in Fig. 2.9. The measurements are compared to NLO QCD predictions, obtained using the FMNR program, with two different choices of scale: $\mu^2 = 1/4(m^2 + p_T^2)$ and $\mu^2 = m^2 + p_T^2$. The data are generally well described by the QCD prediction and although there is a tendency for some of the measurements to lie above the theory, the most recent and the most precise measurements are nearly all well described.

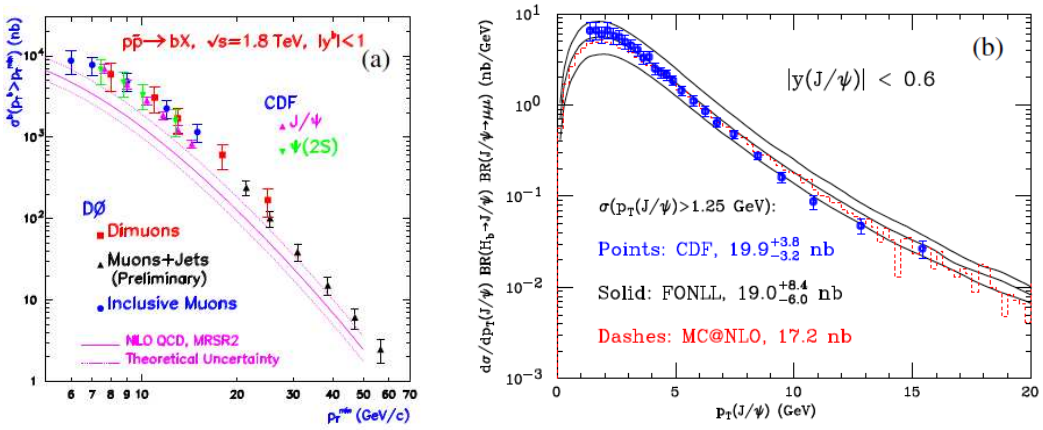

Figure 2.10: Beauty production cross section measurements made at the Tevatron: (a) as a function of p_T^b, made by the CDF and D0 collaborations using RUN I data, and (b) as a function of p_T of J/Ψ from B decays using RUN II data by the the CDF collaboration.

2.5.2 Beauty production at hadron colliders

Beauty production has also been studied in $p\bar{p}$ collisions in the $Sp\bar{p}S$ collider and at the Tevatron. The first of such measurements were carried out by the UA1 experiment at a centre-of-mass energy, $\sqrt{s} = 630$ GeV, using single muon and dimuon final state events [26]. The experiment measured the beauty production cross section as a function of p_T by integrating over the rapidity range $|y| < 1.5$ above a given p_T^{min} which was then compared to an NLO QCD calculation [27]. The data were found to be well described by the theoretical prediction.

Early measurements of the process $p\bar{p} \rightarrow b + X$ for the same cross section as the UA1 measurement but in the range $|y| < 1.5$ were made by the CDF [28] and D0 [29] collaborations at a centre-of-mass energy, $\sqrt{s} = 1.8$ GeV. The data were consistently found to be in excess of the NLO QCD predictions. Some of these measurements are shown in Fig. 2.10(a).

Since then improvements on both the experimental and theoretical fronts have led to reduction in the discrepancy [30]. The most recent CDF measurements [31] of beauty photoproduction using "RUN II" data, in collisions at $\sqrt{s} = 1.96$ GeV, are in agreement with NLO QCD calculations and any residual discrepancy is within the theoretical uncertainties. Figure 2.10(b) shows the p_T spectrum of J/Ψ from B decays analysed in RUN II data by CDF. The data are compared to a Fixed-Order with Next to Leading Logarithm (FONLL) summation [32] and an MC@NLO calculation [33] which combines NLO QCD calculations with parton showering and hadronisation performed by HERWIG Monte Carlo.

2.5.3 Beauty production in $\gamma\gamma$ interactions

The beauty cross section was measured by the L3 collaboration at the LEP collider in e^+e^- collisions at centre-of-mass energies ranging between $\sqrt{s} = 189$ GeV and $\sqrt{s} = 209$ GeV [34]. A heavy quark pair can be produced through the interaction of two almost real photons, one emitted by the incoming electron and one by the positron. The beauty quarks were identified through their semi-leptonic decay into muons or electrons by a fit to the transverse momentum of the lepton with respect to the jet. Figure 2.11 shows the results of this measurement compared to an NLO QCD calculation [35]. The data were found to be a factor of three, and three standard deviations, above the prediction.

More recently, the ALEPH collaboration also measured the beauty production cross section in $\gamma\gamma$ interactions at LEP [36]. The measurement was made at centre-of-mass energies ranging between $\sqrt{s} = 130$ GeV and $\sqrt{s} = 209$ GeV and was the first in $\gamma\gamma$ interactions to identify heavy quarks using a method based on the lifetime of the quark. The cross section was measured to be

$$\sigma(e^+e^- \to e^+e^- b\bar{b}X) = (5.4 \pm 0.8_{\text{stat}} \pm 0.8_{\text{syst}}) \text{ pb}, \tag{2.12}$$

which is consistent with the NLO QCD prediction [35] of between 2.1 and 4.5 pb and hence does not confirm the excess observed by the L3 collaboration.

2.5.4 Dijet correlation measurements at ZEUS

Dijet correlations are particularly sensitive to higher-order effects and so their measurement provides a good test of fixed order QCD calculations. This thesis represents the first of such measurements to be performed in beauty at HERA. However dijet correlations have previously been measured at ZEUS in charm and inclusive-jet production at high transverse energies. Those results are summarised in this section.

Dijet correlations in charm

Charm events were identified [37] by tagging a D^* meson in the decay channel $D^{*+} \to D^0\pi_s^+ \to K^-\pi^+\pi_s^+$ (or the corresponding anti-particle decay), where the small difference in the masses of the D mesons, $\Delta M = m(D^*) - m(D^0)$, yields the low-momentum or "slow" pion, π_s^+, which accompanies the D^0. Events were analysed which contained a tagged D^* meson and at least one reconstructed jet. The measurement was performed on 78.6 pb^{-1} of data collected by the ZEUS detector in the following kinematic region: $Q^2 < 1$ GeV^2, $130 < W_{\gamma p} < 280$ GeV (where

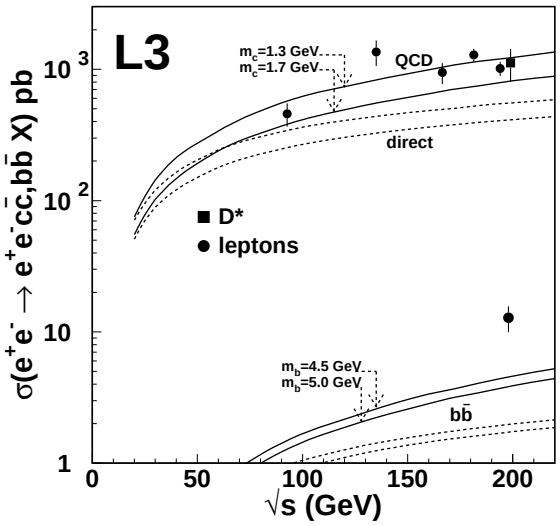

Figure 2.11: Charm (upper) and beauty (lower) production cross sections measured by the L3 collaboration in $\gamma\gamma$ interactions at LEP. The solid line represents the NLO QCD prediction for the sum of the direct and single-resolved processes while the dashed line represents the direct-process contribution.

$W_{\gamma p}$ is the photon-proton centre-of-mass energy), $p_T^{D^*} > 3$ GeV, $|\eta^{D^*}| < 1.5$, $E_T^{jet} > 6$ GeV and $-1.5 < \eta^{jet} < 2.4$.

Several dijet correlation variable cross sections were measured in this analysis, including the difference in azimuthal angle between the two highest-E_T jets, $\Delta\phi^{jj}$. At LO, two jets are produced back-to-back in azimuthal angle and so $\Delta\phi^{jj} = \pi$. Deviations from this value are indications of higher-order QCD effects. The cross section as a function of $\Delta\phi^{jj}$ was also measured separately for values of $x_\gamma^{obs} > 0.75$ and $x_\gamma^{obs} \leq 0.75$, the latter being particularly sensitive to higher order QCD effects. Figure 2.12 shows the $\Delta\phi^{jj}$ cross sections for $x_\gamma^{obs} > 0.75$ and $x_\gamma^{obs} \leq 0.75$ compared to massive NLO QCD predictions ((a) and (b)) and compared to predictions from PYTHIA and HERWIG MC models ((c) and (d)). Although the cross section for $x_\gamma^{obs} > 0.75$ is reasonably well described by the NLO QCD prediction, the data still exhibit a slightly harder distribution. This discrepancy is more apparent in the $x_\gamma^{obs} \leq 0.75$ cross section, where the data have a significantly harder distribution than the NLO QCD prediction to which it is compared. This is indicative of higher order QCD effects.

The PYTHIA MC prediction describes neither the shape nor the normalisation of either cross section, whereas HERWIG MC gives a good description of the shape of all distributions. The fact that

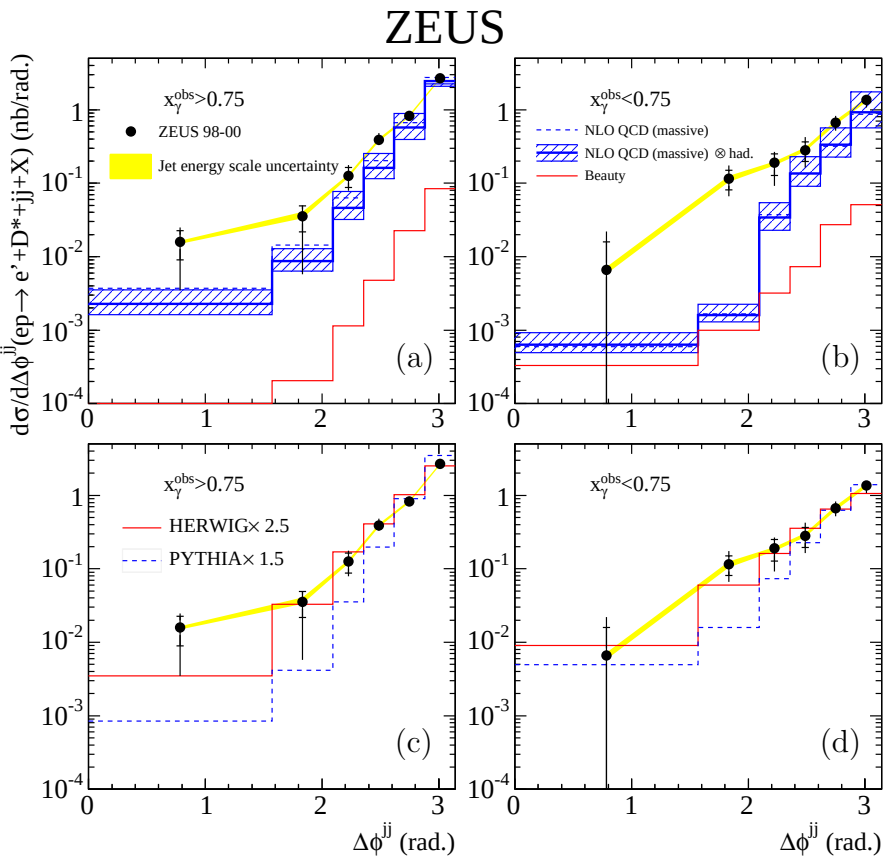

Figure 2.12: Cross section of $d\sigma/d\Delta\phi^{jj}$ separated into ((a) and (c)) direct enriched ($x_\gamma^{obs} > 0.75$) and ((b) and (d)) resolved enriched ($x_\gamma^{obs} < 0.75$) samples. In (a) and (b) the data are compared to NLO QCD predictions (blue band). The beauty component is also shown in red. In (c) and (d) the data are compared to HERWIG (red line) and PYTHIA (dashed blue line) MC models.

a MC prediction which includes parton showers can describe the shape of the data in these kinds of distributions, whereas an NLO QCD prediction cannot indicates that higher orders than NLO are required in the calculation.

Dijet correlations in inclusive jet production

The cross section as a function of $\Delta\phi^{jj}$ was also measured in inclusive dijet production [38]. This measurement was carried out using 81.8 pb^{-1} of data, selecting events with $Q^2 < 1$ GeV^2 and $142 < W_{\gamma p} < 193$ GeV and containing two high-E_T jets, $j1$ and $j2$, where $E_T^{j1} > 20$ GeV, $E_T^{j2} > 15$ GeV and $-1 < \eta^{j1,2} < 3$, with at least one of the jets satisfying $-1 < \eta^{\text{jet}} < 2.5$. Figure 2.13 shows the $d\sigma/d\Delta\phi^{jj}$ cross sections for (a) direct enriched ($x_\gamma^{obs} > 0.75$) and (b) resolved

enriched ($x_\gamma^{obs} < 0.75$) samples compared to an NLO QCD calculation and predictions from PYTHIA and HERWIG MC models.

The conclusions drawn from this measurement confirm the findings of the charm analysis. For high x_γ^{obs}, the data is described by the NLO QCD calculation only at high values of $\Delta\phi^{jj}$, but the prediction falls off more steeply than the data distribution. For $x_\gamma^{obs} < 0.75$, the NLO QCD prediction is much too steep and is significantly lower than the data in all but the highest $\Delta\phi^{jj}$ bin. The PYTHIA MC prediction gives a similarly poor description of the data, wheres HERWIG describes the data well in both cases. This is once again indicative of the need for higher orders to be included in the QCD calculation.

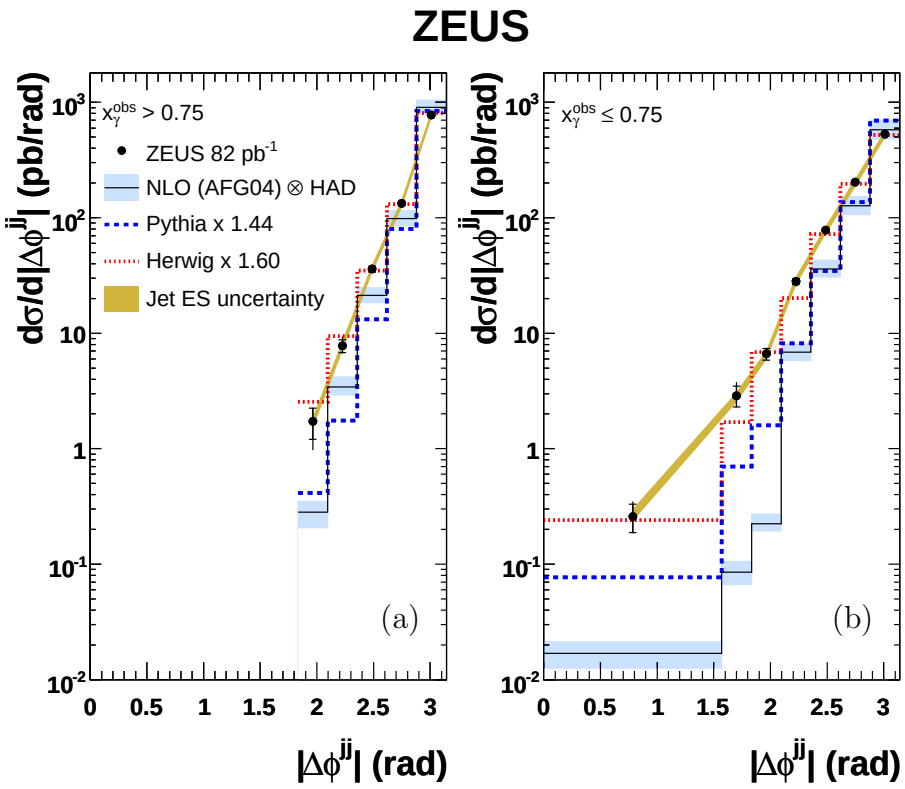

Figure 2.13: Cross section of $d\sigma/d\Delta\phi^{jj}$ separated into (a) direct enriched ($x_\gamma^{obs} > 0.75$) and (b) resolved enriched ($x_\gamma^{obs} < 0.75$) samples. The data are compared to NLO QCD predictions calculated using the AFG04 photon PDF. The data are compared to HERWIG (dashed red line) and PYTHIA (dashed blue line) MC models normalised by the factors given.

Chapter 3

HERA and the ZEUS detector

3.1 HERA

Figure 3.1: Aerial photograph of the Volkspark in Hamburg, Germany showing the locations of the HERA accelerator and the pre-accelerator, PETRA.

The Hadron-Elektron Ring Anlage (HERA), was a particle accelerator which collided electrons or positrons and protons. It was located 10-20 m underground beneath the Deutsches Elektronen-Synchrotron (DESY) site and the Hamburg Volkspark (see Fig. 3.1). During its history, HERA operated at four different proton beam energies. After an initial electron beam energy of 26.7 GeV,

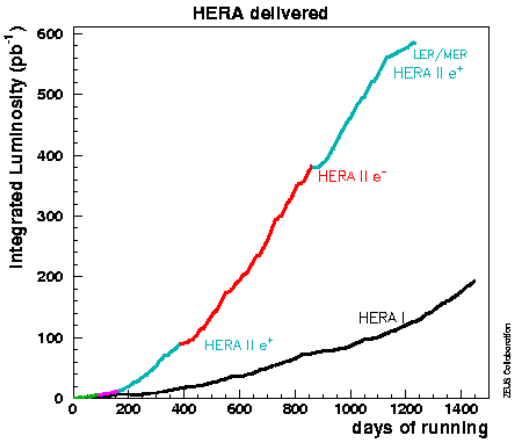

Figure 3.2: Luminosity delivered by HERA during the different running periods.

HERA ran at 27.5 GeV from 1995 until the end of running. Until the end of 1997, it collided the electron beam with a 820 GeV proton beam, yielding a centre-of-mass energy $\sqrt{s} = 300$ GeV. In 1997, the proton beam energy was increased to 920 GeV increasing the centre-of-mass energy to $\sqrt{s} = 318$ GeV. The final two running periods took place in 2007 are known as low-energy and high-energy running (LER and MER) when the proton beam energy was decreased to 460 GeV and 575 GeV respectively. The final collision in HERA took place on 30th June 2007. The integrated luminosity delivered by HERA during these four running periods is summarised in Fig. 3.2.

The HERA tunnel was 6.3 km long and contained separate storage rings for the electrons and protons which were not circular but had four straight sections, each 360 m in length. The beams were brought to zero crossing-angle collisions in two of these straight sections. These interaction points (IPs) were in the north and south halls where the two multi-purpose detectors, H1 and ZEUS, were located. The other two experiments used fixed target collisions. HERMES, in the east hall, studied collisions of the electron beam with polarised gas to measure nucleon spin. HERA-B, in the west hall, was designed to study the interaction of the proton beam with fixed wire targets in order to investigate $\mathcal{CP}$ violation.

3.1.1 The HERA upgrade

In 2000-2001, HERA was shut down in order to upgrade the machine with the aim of reaching a target integrated luminosity of 1 fb^{-1} by 2005. The hope was that with a higher luminosity being delivered to the experiments, new interesting measurements would be possible [39] such as an investigation into high-x, high-Q^2 events which had been observed by ZEUS and H1 during the HERA I running period. The increase in luminosity was achieved by installing superconducting

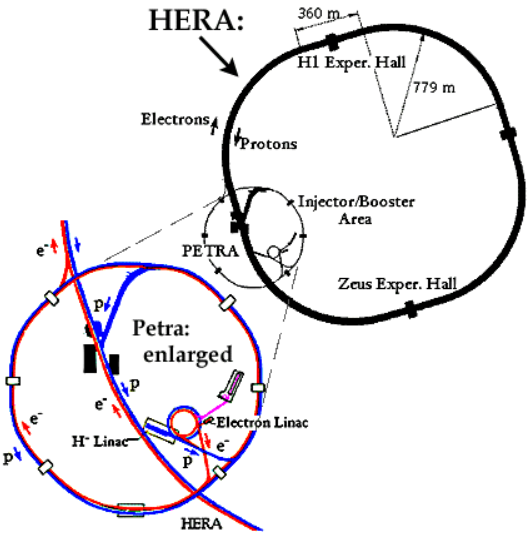

Figure 3.3: Diagram of the HERA ring with an enlargement of the pre-accelarator, PETRA, and the injection system.

magnets close to the interaction points in order to make the beam cross section smaller. The upgraded machine was known as HERA II. The data analysed in this thesis were collected in the HERA II high-energy running period. During this shutdown period a silicon Micro-Vertex Detector was installed in the ZEUS detector in the region closest to the beam pipe. The introduction of this detector component allowed precision heavy flavour measurements, such as the one described in this thesis, to be carried out.

3.1.2 The HERA injection system

A diagram of the HERA injection system is shown in Fig. 3.3. In the proton injection system, negative Hydrogen ions (H^-) were first accelerated to 50 MeV in the proton LINear ACcelerator (LINAC) before being stripped of electrons in the DESY III storage ring where the remaining protons were accelerated to 7.5 GeV in 11 bunches with a temporal spacing of 96 ns. These bunches were transferred into PETRA where they were accelerated up to 40 GeV. Finally they were injected into the main HERA proton storage ring, the process being repeated until there were 210 bunches in the machine, and then accelerated up to 920 GeV using radio frequency cavities. Superconducting dipole and quadrupole magnets guided the protons around the ring.

Acceleration of the electrons began in LINAC II where they reached energies of 450 MeV. Once transferred to the DESY-II storage ring, they were accelerated to 7.5 GeV before being injected in PETRA where they reached an energy of 14 GeV in bunches which were 96 ns apart. On injection

into the HERA electron storage ring, they underwent a final acceleration to 27.5 GeV. As with the proton beam, bunches were injected until there were 210 bunches in the machine.

3.2 The ZEUS detector

ZEUS was a multi-purpose detector which was designed to study the lepton-proton collisions produced by HERA. Due to the asymmetry of the beam energies, many of the processes observed at HERA produced events in which most of the final state particles were boosted in the direction of the proton beam. Thus the ZEUS detector contained more apparatus in this direction. It covered almost all of the 4π solid angle, breaking hermeticity only in a small region near the beam pipes. Figures 3.4 and 3.5 show cross sections through the ZEUS detector. In this section, an overview of the main components of the ZEUS detector will be given, starting from the interaction point (IP) and moving radially outwards. More detailed descriptions of the most relevant components will be given in the following sections, but for a more complete description of the ZEUS detector see [40].

From 2001 onwards, the component closest to the beam-pipe was the Micro-Vertex Detector (MVD). It was a silicon strip detector and is central to this analysis; it will be described in more detail in Section 3.2.2. Surrounding the MVD was the Central Tracking Detector (CTD) with the Forward Tracking Detector (FTD) and Rear Tracking Detector (RTD) at its ends. Outside these inner tracking components lay the calorimeters: the Uranium CALorimeter (UCAL) and the BAcking Calorimeter (BAC). Just inside and outside the iron yoke, which contained the BAC, were the MUON chambers: FMUI, BMUI and RMUI inside and FMUON, BMUON and RMUON (in the Forward, Barrel and Rear) outside the yoke.

The VETO wall is an iron wall with scintillators on both sides, it is designed to protect the central detector from beam halo particles. The luminosity measurement was carried out using two systems not shown in Fig. 3.4.

3.2.1 The ZEUS coordinate system

The ZEUS coordinate system is a right-handed cartesian coordinate system with the origin defined as the nominal IP which is at the geometrical centre of the ZEUS detector. The positive z-axis points in the direction of the proton beam or the forward direction and the x-axis points towards the centre of the HERA ring. The y-axis is at right-angles to the other two and points approximately vertically upwards. In polar coordinates, r is the radial distance from the IP, θ is the polar angle measured with respect to the z-axis and ϕ is the azimuthal angle measured with respect to the

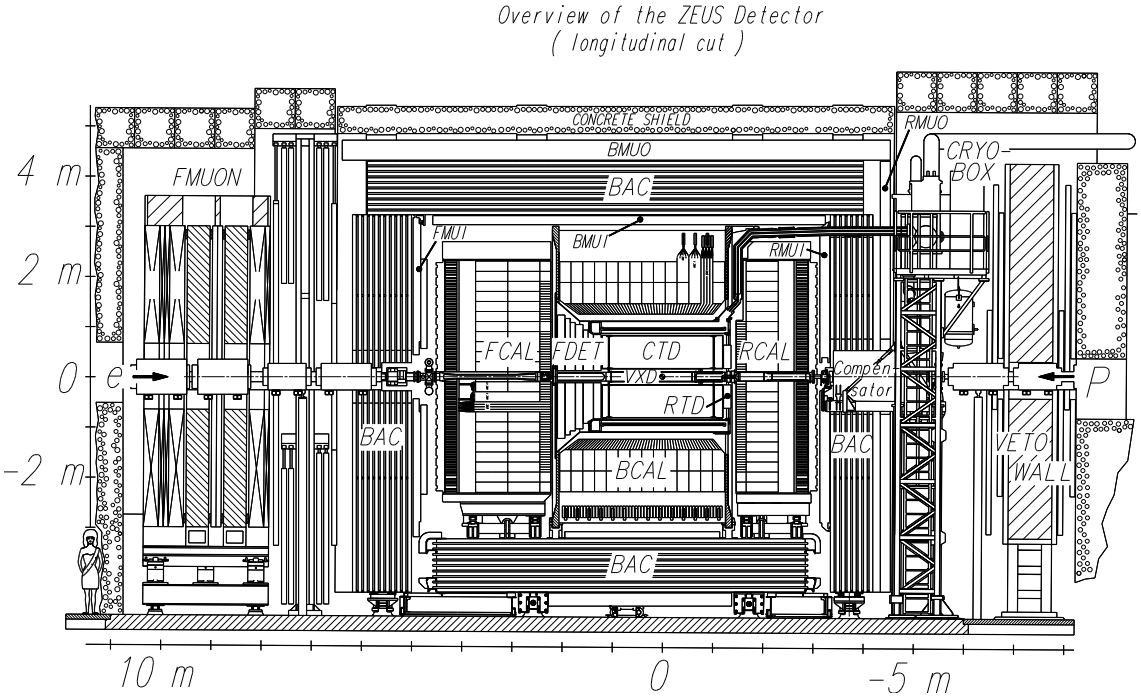

Figure 3.4: Cross section of the ZEUS detector along the beam direction.

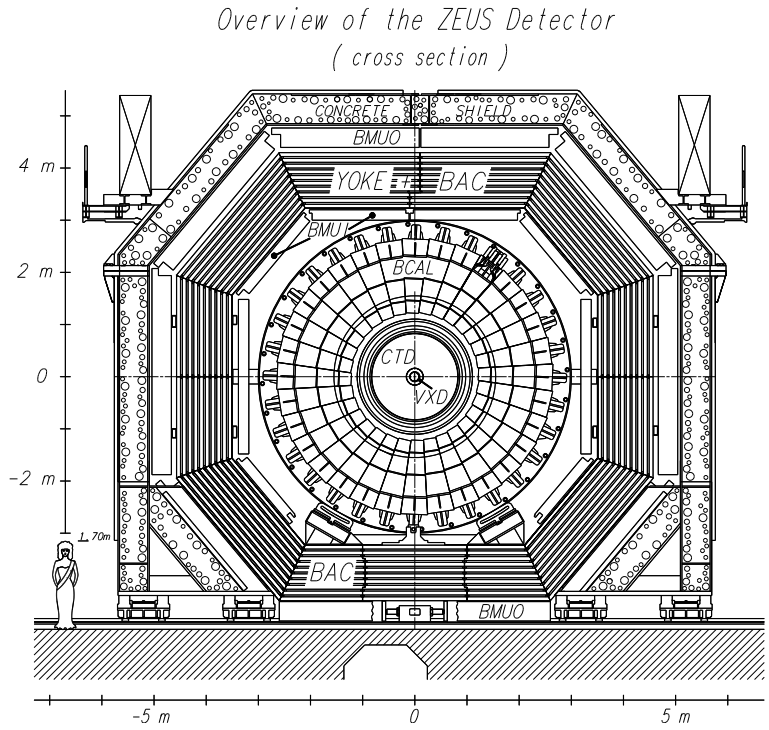

Figure 3.5: Cross section of the ZEUS detector perpendicular to the beam direction.

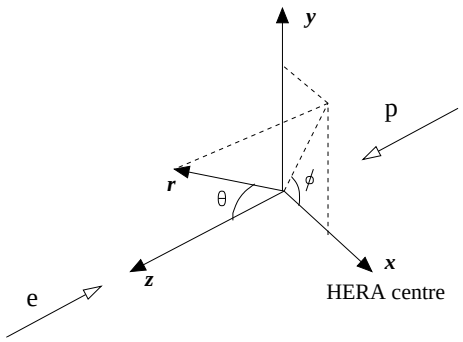

Figure 3.6: ZEUS coordinate system.

x-axis, as shown in Fig. 3.6. A quantity more commonly used than θ is pseudorapidity, η, defined as $\eta = -\ln(\tan\frac{\theta}{2})$.

3.2.2 The micro-vertex detector

The Micro-Vertex Detector (MVD) [41] was inserted into the ZEUS detector, inside the CTD, during the 2001 HERA upgrade. Its purpose was to enable heavy quark tagging by identifying displaced secondary vertices and to improve the tracking system as a whole. Together with the CTD it measured the trajectories of charged particles, detecting them by means of 712 single-sided silicon strip detectors. The MVD comprised a barrel (BMVD) and a forward (FMVD) section, giving the whole sub-detector a coverage in polar angle of $7° < \theta < 130°$.

Figure 3.7 shows the arrangement of silicon sensors in the BMVD. They were arranged in concentric layers around the z-axis, with 75% of the azimuthal angle covered by 3 layers and the remaining 25% covered by 2 layers due to restrictions in space around the beam pipe. The square detectors were arranged in pairs, as shown in Fig. 3.8, with one sensor providing r-ϕ information and the other providing z-ϕ information. This is known as a half-module. Two half-modules were coupled together to provide complementary r-ϕ and z-ϕ information in each layer. A ladder, which lay parallel to the beam, comprised 5 such modules. The 63 cm long BMVD was centred at the interaction point. The FMVD sensors differed only in geometry, having a wedge shape instead of being square. These sensors were arranged in 4 vertical planes, known as wheels.

Test-beam measurements found the spatial resolution of barrel half-modules to be about 13 μm at normal incidence. The impact parameter of tracks crossing 3 layers of the BMVD has been measured with a resolution of 100 μm.

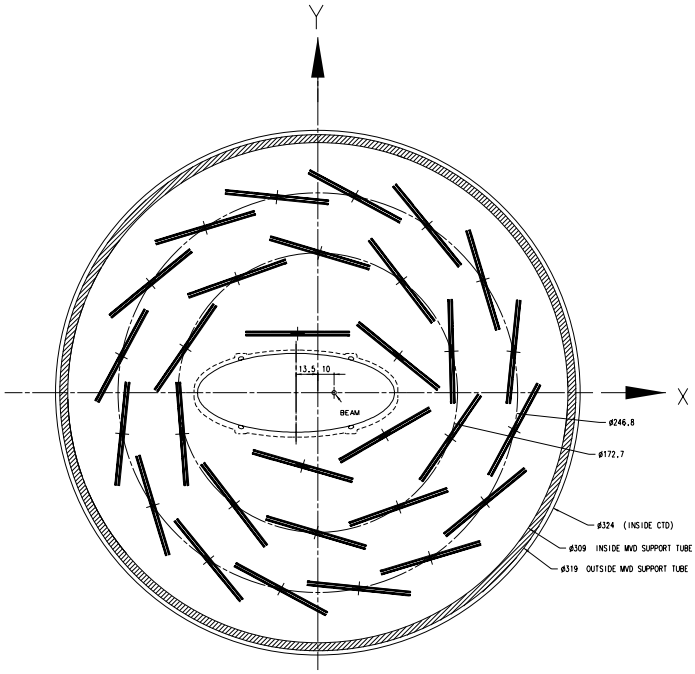

Figure 3.7: x-y cross section of the barrel MVD.

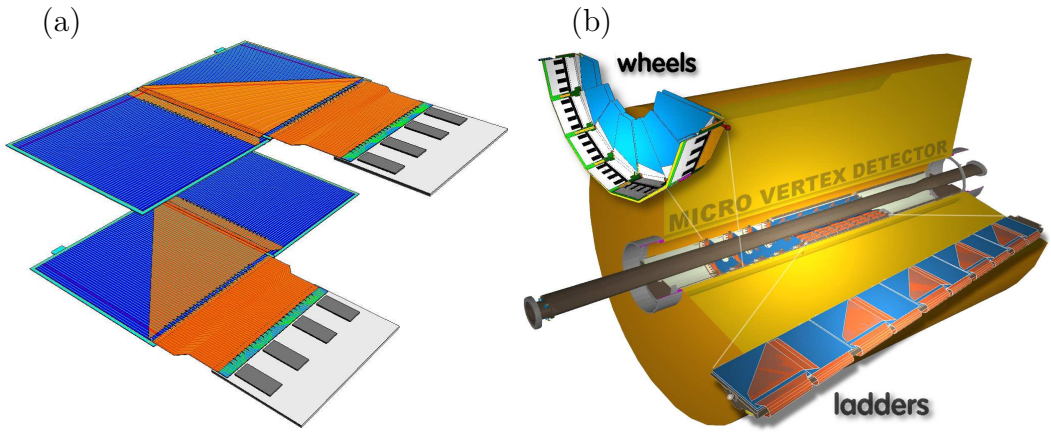

Figure 3.8: (a) Two half-modules of the MVD and (b) cut-away showing the whole MVD situated inside the CTD and the positions of the barrel ladders and forward wheels.

3.2.3 The central tracking detector

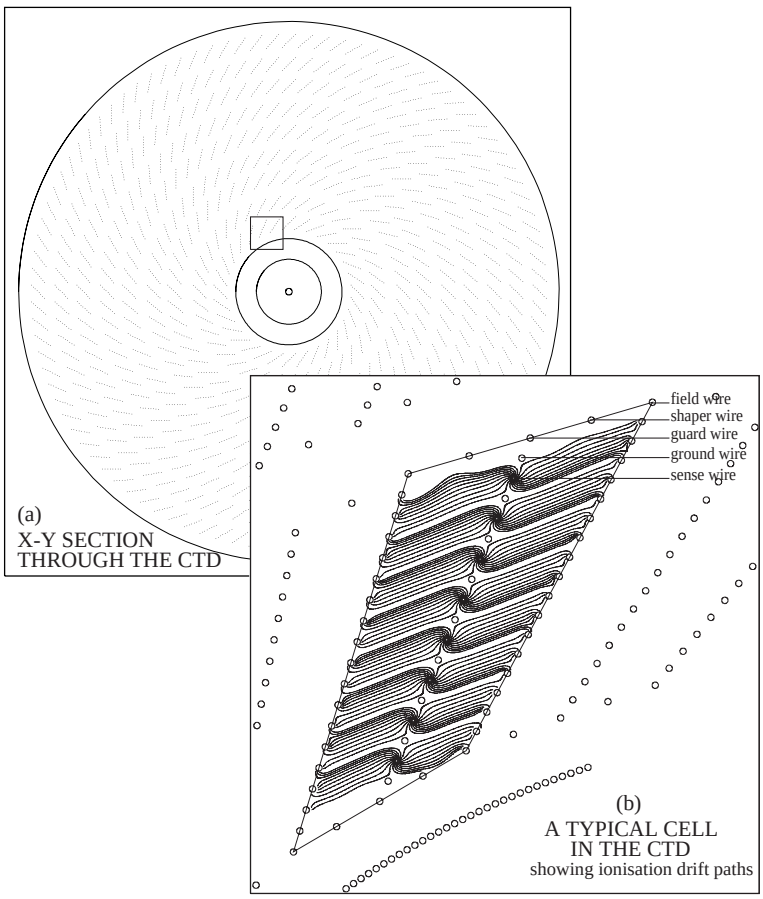

Figure 3.9: (a) r-ϕ cross-section through the CTD, showing 9 superlayers, and (b) the layout of a typical cell showing ionisation drift paths.

The CTD [42] was a cylindrical multi-wire drift chamber used to measure the direction and momentum of charged particles and to provide information about their identity by estimating the energy loss dE/dx. It operated in a magnetic field of 1.43 T, generated by a thin superconducting coil and contained a total of 4608 sense wires and 19584 field wires. The magnetic field bent the trajectories of charged particles so that their momentum could be measured. The chambers were filled with a gas mixture of argon, carbon dioxide and ethane bubbled through ethanol. A charged particle traversing the chamber would produce ionisation of the gas along its path. The resulting electrons drifted towards the positive sense wires while the positive ions drifted towards the field wires. An avalanche effect occurred so that a measurable pulse was induced on the sense wires. Figure 3.9 shows the layout of a typical CTD cell, which consisted of 8 radial sense wires and its associated field wires.

The CTD covered a polar angle region of $15° < \theta < 164°$ and was 2.05 m long, with an inner and outer radius of 18.2 cm and 79.4 cm, respectively. It consisted of 72 cylindrical drift chamber layers organised into 9 superlayers as shown in Fig. 3.9. The odd-numbered (axial) superlayers contained drift wires which ran parallel to the z-axis, while wires in the even-numbered (stereo) superlayers subtended an angle of $\pm 5°$ to the z-axis, allowing accurate measurements to be made of the particle's coordinates in both z and $r - \phi$. The position resolution of the CTD for tracks traversing all nine superlayers was ~ 180 μm in $r - \phi$ and ~ 2 mm in z. The first three axial layers were also used for trigger purposes using a system known as z-by-timing. This provides crude, ~ 4 cm resolution, but quick z-position information by comparing pulse arrival times between the two ends of the chamber.

3.2.4 The Uranium calorimeter

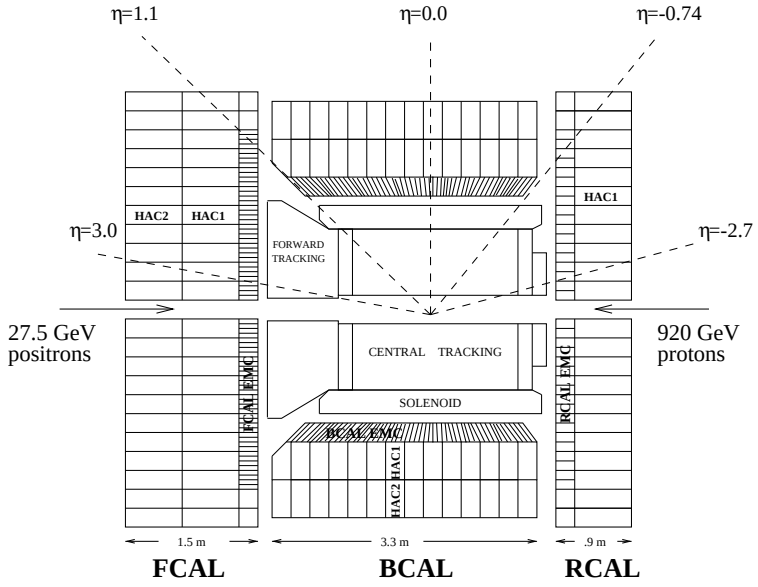

Figure 3.10: Schematic of the ZEUS Uranium calorimeter in the $x - z$ plane.

The UCAL was a high resolution compensating calorimeter covering 99.7% of the solid angle. It comprised three sub-detectors: the Forward (FCAL) [43], Barrel (BCAL) [44, 45] and Rear (RCAL) [43] calorimeters as shown in Fig. 3.10. Each section was divided into towers, consisting of both electromagnetic (EMC) and hadronic (HAC) cells. The towers in the FCAL and RCAL laid parallel to the beam direction whereas the BCAL towers were perpendicular to it. The length of the towers was designed to ensure that at least 95% of a jet's energy is deposited in the calorimeter in 90% of events. Figure 3.11 shows the arrangement of EMC and HAC blocks of cells in towers in each of the three sub-detectors of the ZEUS calorimeter. A BCAL tower consisted of four EMC

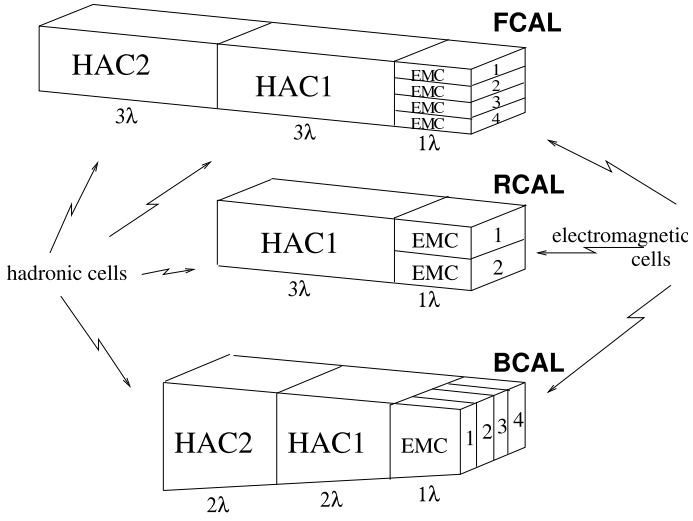

Figure 3.11: The different configurations of the towers found in the FCAL, BCAL and RCAL.

cells, each measuring 5 cm by 20 cm, and two HAC cells, which measured 20 cm by 20 cm. The EMC blocks were 1 interaction length (λ) deep and the HAC sections were 6λ, 4λ and 3λ deep in the FCAL, BCAL and RCAL respectively. The HAC sections in the FCAL were longer than in the BCAL and RCAL due to the increased hadronic activity present in this region.

EMC and HAC cells both had alternating layers of depleted Uranium (3.3 mm of absorber) and plastic scintillator (2.6 mm of active material). Photons emitted by the active material were directed via light guides and wavelength shifters on the sides of the cell to photo-multiplier tubes (PMTs) at the rear of the tower. The Uranium acts as a compensator, absorbing neutrons in a hadronic shower and emitting the energy as photons, such that the same number of photons are present in a hadronic and an electromagnetic shower. Thus the ZEUS calorimeter had the same response for hadronic or electromagnetic showering. The energy resolution for electrons and hadrons was $\frac{\sigma(E)}{E} = \frac{18\%}{\sqrt{E}}$ and $\frac{\sigma(E)}{E} = \frac{35\%}{\sqrt{E}}$ respectively.

3.2.5 Muon chambers

The muon chambers were designed to detect particles originating from the interaction region which could traverse the calorimeter and yoke without being absorbed. Such particles were likely to be muons which are heavy compared to electrons and not strongly interacting. The muon detection system was divided into the barrel and rear detectors (BMUON and RMUON) [46] and the forward muon detector (FMUON) which had to be capable of detecting the typically higher momentum muons which were produced in this direction.

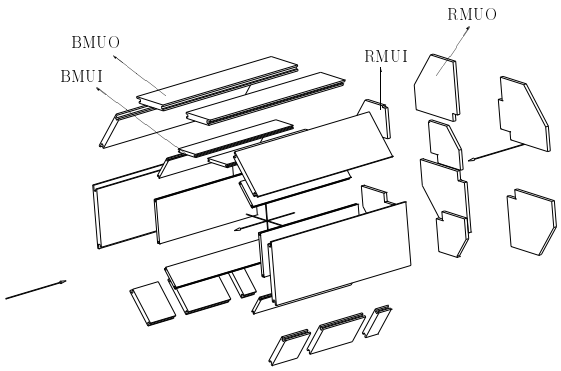

Figure 3.12: An exploded view of the barrel and rear muon chambers.

The muon momentum was determined by comparing the direction of the particle before and after it traversed the iron yoke. As such, the muon detector was divided into the inner barrel (rear) detector, located between the CAL and the iron yoke, known as the BMUI (RMUI) and the outer detector, located outside the yoke, known as the BMUO (RMUO). A diagram of the BMUON and RMUON can be seen in Fig. 3.12. The momentum measurement was compared with that made in the CTD to reduce background from non-prompt muons.

The chosen method of particle detection in the muon chambers was by means of Limited Streamer Tubes (LSTs). An LST consisted of 8 cells filled with a gas mixture of carbon dioxide, argon and isobutane, each containing 1 sense wire. The sense wires were separated by 1 cm. The sense wires were brought to 4500 V during data taking so that they acted as anodes, while the graphite lined cell walls acted as cathodes. Each BMUO or BMUI (and RMUO or RMUI) chamber consisted of 2 planes of LST displaced from one another by half a cell in order to gain acceptance for particles detected at a cell boundary in one of the planes. Each plane in the barrel (rear) chambers contained two layers of LST separated by a 40 cm (20 cm) thick aluminium structure which was a lightweight and rigid support for the LSTs. On one of the outer walls of the LSTs, analogue readout strips were attached orthogonal to the wires. These strips allowed a determination of the coordinate within the LST to be made. With the strip readout, the spatial resolution in the coordinate orthogonal to the wires was 200 μm and 400 μm parallel to the wires.

3.2.6 Luminosity measurement

It is very important in any cross section measurement that the luminosity is accurately determined. At ZEUS, the luminosity was measured using the bremsstrahlung process, $ep \to e\gamma p$. This process

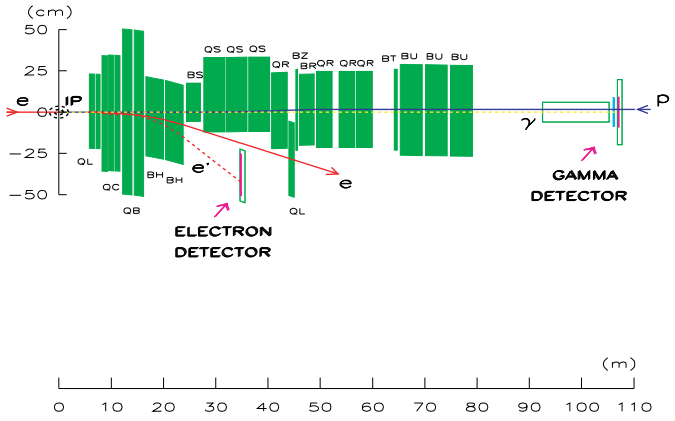

Figure 3.13: Schematic of the photon calorimeter luminosity monitor.

has a large cross section ($\sim$ 15 mb) and could be measured almost instantaneously to a high precision. It is calculated to leading-order (LO) using the Bethe-Heitler formula [47] and the higher-order corrections to the calculation are known to within 0.5%.

There were two systems in the ZEUS detector which were used in the luminosity measurement. The first was the photon calorimeter, a lead scintillator located at $z = -104$ m, which detected small-angle Bethe-Heitler photons. The luminosity calorimeter apparatus is shown in Fig. 3.13. A lepton calorimeter was located at $z = -34$ m but this could not be used in the luminosity measurement due to poor understanding of the acceptance. As a result, the measurement was extremely sensitive to background from synchrotron radiation. In HERA II running, active filters were installed to suppress the increased synchrotron radiation of the upgraded collider [48]. The second system was not sensitive to synchrotron radiation. In the exit window of the luminosity monitor, a small fraction of Bethe-Heitler photons converted to e^-e^+ pairs. The paths of the e^- and e^+ were bent vertically by a dipole magnet and then they were detected by tungsten-scintillator calorimeters which can be seen in Fig. 3.14. The uncertainty on the final luminosity measurement was 2.6%.

3.2.7 Trigger system

The bunch crossing frequency at the nominal interaction point at ZEUS was $\sim$ 10 MHz. However, in the majority of bunch crossings, no *ep* collision occurred and so there was no event observed in the ZEUS detector. The dominant contribution to events seen in the ZEUS detector was background from collisions between beam particles and gas in the beam pipe. These are known as beam-gas events and occurred at a rate of $10 - 100$ kHz. This rate had to be decreased to a level compatible

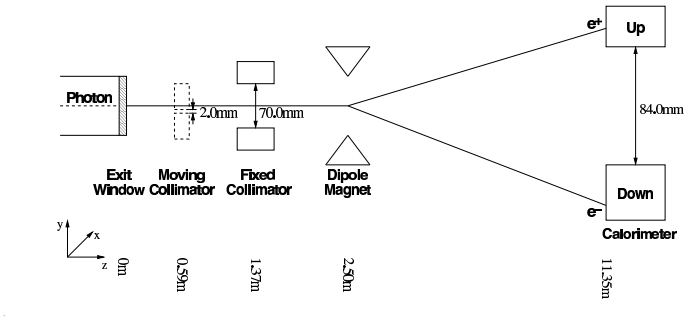

Figure 3.14: Schematic of the luminosity spectrometer.

with data storage capacities without reducing the rate of ep interactions (< 10 Hz). To achieve this and to select interesting ep events for analysis, ZEUS adopted a three-level trigger system [49].

The First Level Trigger (FLT) was a hardware-based trigger which reduced the rate to ~ 1 kHz by eliminating most of the beam gas events. Individual detector components had their own FLTs which could accept or reject events and which then passed the decision onto the Global First Level Trigger (GFLT) where the final decision was made before passing this back to the component readouts. The whole process took > 96 ns and so the data were buffered in a 4.4 μs pipeline. This means that the GFLT decision was issued 46 crossings after the event which produced it. There was an additional trigger component known as the Fast Clear which aborted events after the FLT level based on information from the calorimeter trigger data.

The events accepted by the FLT and Fast Clear were then passed to the Second Level Trigger (SLT) which was a software trigger based on a network of transputers. Just as in the FLT, individual detector components passed a decision to the Global Second Level Trigger (GSLT) where a final decision was made which was passed back to the components. The SLT reduced the rate to a maximum of ~ 100 Hz. At this stage, the data were passed to an event builder which took information from each component and formed the data structure of an event which could transferred to the Third Level Trigger (TLT).

The TLT ran a reduced version of the full offline reconstruction software decreasing the rate to a few Hz. The TLT had different triggers which looked for event topologies of particular interest to the various physics groups based on combined component data, jet and tracking information and other kinematic quantities. Finally the accepted events were written to mass storage tape for full event reconstruction. The total time between the bunch crossing and a final TLT decision was ~ 0.3 s

Chapter 4

Event Reconstruction

In this chapter the reconstruction of physics events in the ZEUS detector is presented. In particular the method of reconstruction of muons and jets is described.

4.1 Track and vertex reconstruction

Offline track reconstruction takes place in two stages. The first stage uses the pattern recognition package VCTRACK [50] which uses CTD and MVD hits to maximise track finding efficiency. The trajectory of a particle in the magnetic field of the detector describes, to first approximation, a cylindrical helix. In this first stage, a multi-pass algorithm combines hits, starting with the outer CTD detector layers and moving inwards, to produce the initial helix trajectories. These trajectories can then be used to include additional hits. This method finds tracks with both good CTD and good MVD constraints.

In the second phase, the track information is passed to a fitting package called KFFIT [51] which is based on a Kalman Filter technique. This accurately determines the track parameters and their covariances. Close to the interaction point, the magnetic field is essentially parallel to the CTD axis, and the helix can be described by 5 parameters which are shown in Fig. 4.1:

- ϕ_H, the azimuthal angle of the helix tangent at the distance of closest approach to the z-axis,
- Q/R, where Q is the "charge" of the track given by the direction of curvature and R is the local radius of curvature of the helix,
- QD_H, where D_H is the distance of closest approach to the z-axis,

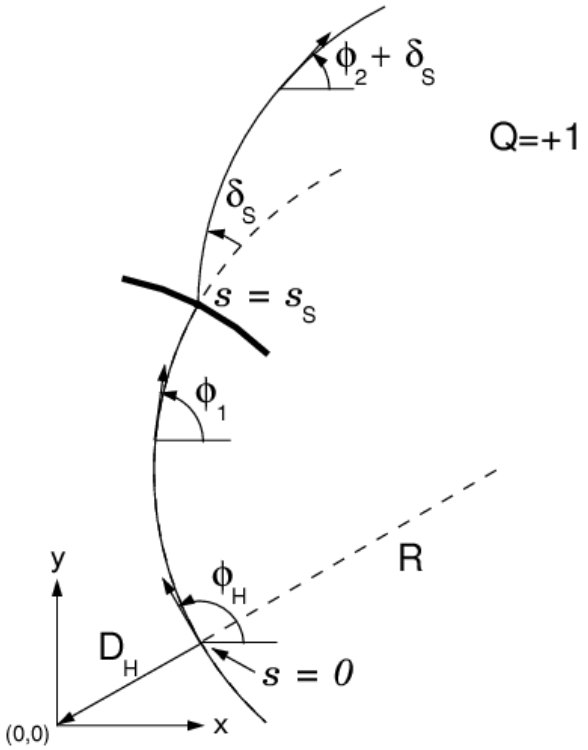

Figure 4.1: Illustration of the parameters used in the VCTRACK track fit.

- Z_H, the z-coordinate at this point,
- $\cot\theta_H$, where θ_H is the polar angle of the helix.

The coordinates of a point on the helix can then be parameterised as:

$$X = X_H + QR(-\sin\phi + \sin\phi_H), \tag{4.1}$$

$$Y = Y_H + QR(+\cos\phi - \cos\phi_H), \tag{4.2}$$

$$Z = Z_H + s(\phi)\cot\phi, \tag{4.3}$$

where $s(\phi)$ is the path length in the $x-y$ plane given by $-QR(\phi - \phi_H)$.

In a similar way, VCTRACK was used to reconstruct the primary vertex at ZEUS. Firstly a beam constraint is applied: it is assumed that the vertex lies along the axis of the proton direction. Then pairs of tracks with a common vertex are combined with other track pairs and a vertex is chosen based on the χ^2 of the best combination. The outlying tracks are removed before a final primary vertex is determined [52].

4.2 Beam spot

The ZEUS beam spot position was found by obtaining a distribution of reconstructed primary vertices for a number of physics events and then fitting it with a Gaussian curve. This number of events was optimised in order to find a compromise between precision and granularity and was found to be 2000 events [53]. A precise determination of the beam spot can provide a better estimate of the event primary vertex than an explicit reconstruction of the vertex itself. For that reason the beam spot is used in the analysis described in this thesis as a reference for the muon impact parameter. The ZEUS beam spot was found [54] to be an ellipse with the following dimensions:

$$\sigma_{x,bsp} = (83.1 \pm 1.2(\text{stat.}) \pm 8(\text{syst.}))\mu\text{m}, \tag{4.4}$$

$$\sigma_{y,bsp} = (19.7 \pm 5.9(\text{stat.}) \pm 20(\text{syst.}))\mu\text{m}. \tag{4.5}$$

4.3 Muon finding

Muons are found by matching reconstructed segments in the barrel and rear muon detectors to reconstructed tracks in the inner tracking detectors. This is carried out using a package called BREMAT [55] (Barrel and Rear Extrapolation MATching). Tracks reconstructed in the tracking detectors undergo the following preselection:

- track momentum, $p > 1$ GeV;
- polar angle of the track, $\theta > 20^\circ$ (to ensure good CTD acceptance);
- the track must pass through the first CTD superlayer and also through at least the third superlayer;
- track impact parameter $|D_H| < 10$ cm;
- the z coordinate of the distance of closest approach to the nominal IP $|z_H| < 75$ cm;
- $\chi^2_{track}/n.d.f < 5$;
- distance, Δ, from a central point in the BMUON segment to the straight line obtained when the CTD track is extrapolated to the edge of the calorimeter, $\Delta \leq 150$ cm.

The tracks passing the preselection are then extrapolated, from the inner tracking detectors outwards, to the inner muon chambers using GEANE [56] which takes into account the full error matrix of the matching χ^2 to evaluate a true matching probability. The matching is then carried out in position and angle in two projections, yielding 4 degrees of freedom. A detailed description of the BREMAT procedure can be found in [55].

4.4 Hadronic system reconstruction

The hadronic final state can be reconstructed from energy flow objects (EFOs) which combine information from calorimetry and tracking. The EFOs are constructed in the following three stages.

1. Clustering begins with the combination of adjacent cells in each calorimeter layer separately. Cells are iteratively combined with the neighbouring cell with the highest energy to form *cell islands*, as shown in Fig. 4.2.

2. Charged tracks which have been fitted to the primary vertex and which pass certain requirements are extrapolated to the surface of the CAL. The track requirements are as follows:

   - $0.1 < p_T < 20$ GeV for tracks with at least 4 CTD superlayer hits,
   - $0.1 < p_T < 25$ GeV for tracks with at least 7 CTD superlayer hits.

   If a track passing this preselection passes within 20 cm of a cell island then it is matched to that cell island.

3. The associated track and CAL islands are called EFOs and the combination of the information from each is carried out in the following way:

   - when comparing the CTD momentum resolution of a track and the energy resolution of the CAL deposit, if the CTD resolution is the better of the two then the tracking information is used to describe the EFO,
   - good tracks not associated with an energy deposit in the CAL are assumed to be low energy pions and information is taken from tracking,
   - unmatched energy deposits in the CAL are assumed to be neutral particles and CAL information alone is used,
   - CAL information alone is also used for energy deposits which are associated to more than three tracks.

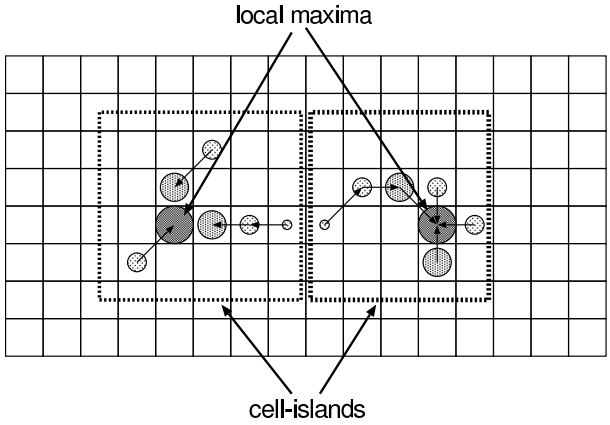

Figure 4.2: Schematic diagram of the formation of cell islands in the calorimeter.

Due to some discrepancies found when comparing the EFOs reconstructed in data and those reconstructed in MC [57, 58], some corrections have been made to the EFOs. Energy losses due to dead material, such as such as the beam pipe and solenoid, are difficult to include fully in the MC detector simulation. Therefore a correction has been made offline to the EFOs as a function of their energy and polar angle. In addition to this, a correction was made to compensate for the presence of a muon in the event. Muons do not release all their energy in the CAL and therefore if an energy deposit measured in the CAL is used to reconstruct a muon contained in a jet, then the jet energy will be systematically lower than it should be. It is expected that an EFO corresponding to a particle such as a muon would be described using tracking information alone but nevertheless a correction was applied to account for those EFOs reconstructed with CAL information.

4.5 Jet finding

In order to describe the dynamics of an interaction, final state particles are grouped into jets of collimated particles using a jet algorithm. Although the dynamics of the jets in an event are closely related to the dynamics of the partons produced in the hard subprocess, the definition of a jet relies on the algorithm used for reconstruction. An important feature of a jet algorithm is infrared safety; the output of the algorithm should be independent of soft or collinear emissions which cause infrared divergences in the theoretical calculations. Cone based jet algorithms are widely used at hadron-hadron colliders and are standardised according to criteria set at the Snowmass meeting of 1990 [59]. Jets reconstructed using such algorithms consist of calorimeter cells (or partons, in a theoretical description), i, with a distance, R_i from the jet centre defined by:

$$R_i = \sqrt{(\eta_i - \eta_{jet})^2 + (\phi_i - \phi_{jet})^2} < R, \tag{4.6}$$

where R is the jet cone radius. However this method can be ambiguous in its treatment of overlapping jets. The ambiguity can be avoided by using, instead, the k_T clustering algorithm [60] as implemented in the KTCLUS [61] library which has been used in this analysis. This has the advantage of being infrared safe to all orders [62].

In a cluster algorithm, a distance measure is defined which determines which particles should be merged. This quantity is defined between two objects, i and j, to be:

$$d_{ij} = \frac{\min(E_{T,i}^2, E_{T,j}^2)\left[(\eta_i - \eta_j)^2 + (\phi_i - \phi_j)^2\right]}{R^2}, \tag{4.7}$$

where R is a parameter analogous to the cone radius, and in the limiting case of the distance between object i and the proton remnant travelling in the z-direction, we define:

$$d_i = E_{T,i}^2. \tag{4.8}$$

If $d_{min} \equiv \min[d_i, d_{ij}] = d_{ij}$ then objects i and j are merged into a single object, k, according to the specific recombination scheme used. For example, in the E-recombination scheme (which was used in this analysis), the four-momentum of the composite object is the sum of the four-momenta of the objects from which it is formed, ie.

$$P_k = P_i + P_j. \tag{4.9}$$

The object k is then used in further iterations of the algorithm. However, if $d_{min} = d_i$ then the object is a final state jet and is removed from further clustering. The process is repeated until all objects have been removed in this way.

In this analysis, the k_T clustering algorithm in the longitudinally invariant mode [63] has been used on EFOs in the experimental data to produce jets in the final state. The E-recombination scheme was used, producing massive jets whose four-momenta were, therefore, the sum of the four-momenta of the clustered EFOs.

Chapter 5

Event Selection

For the measurement in this thesis a sample of dijet photoproduction events containing a muon were selected. This chapter focusses on each step in this selection process, describing the trigger chains used and the methods employed to select photoproduction events and reject beam gas events. The kinematic cuts presented and the MC samples which will be used to extract the beauty fraction in the data are described. Finally control plots of data distributions compared to the MC are presented.

5.1 Trigger selection

The events used in this analysis were first selected from the data sample by requiring that certain triggers fired at the first, second and third levels of the ZEUS trigger system. At the third level, an event selected for analysis must have fired at least one of the following trigger slots, all of which imply that the first and second level triggers fired:

HFL5: Inclusive dijet trigger slot

- 2 jets with $E_T > 4.5$ GeV and $|\eta| < 2.5$;
- $p_z/E < 0.95$ (measured in the CAL);
- $E - p_z < 100$ GeV (measured in the CAL).

HFL13: Inclusive semi-leptonic muon slot

- at least one muon found at second level trigger;
- muon reconstructed in barrel/rear muon chambers with a matching CTD track (matched with GLOMU [64]);
- total $E_T > 9$ GeV (measured in the CAL).

HFL25: Muon plus dijet trigger slot

- at least one muon found at second level trigger;
- muon reconstructed in barrel/rear muon chambers with a matching CTD track (matched with GLOMU [64]);
- 2 jets with $E_T > 3.5$ GeV and $|\eta| < 2.5$;
- $p_z/E < 1.0$ (measured in the CAL);
- $E - p_z < 100$ GeV (measured in the CAL).

5.1.1 Trigger efficiency

The percentage of the total number of events accepted by the triggers which fired HFL25 only was $\sim 1.5\%$ and therefore only the efficiencies of HFL5 and HFL13 were considered. These trigger slots are independent (apart from common vetoes and minimal track requirements) and so can be used as reference trigger slots to one another. Therefore the efficiencies can be evaluated as:

$$\epsilon_{\mathrm{HFL5}} = \frac{N_{\mathrm{HFL5} \bigcap \mathrm{HFL13}}}{N_{\mathrm{HFL13}}}, \tag{5.1}$$

$$\epsilon_{\mathrm{HFL13}} = \frac{N_{\mathrm{HFL5} \bigcap \mathrm{HFL13}}}{N_{\mathrm{HFL5}}}, \tag{5.2}$$

where N_{HFL5} and N_{HFL13} are the numbers of events which fired HFL5 and HFL13 respectively. The number of events firing both HFL5 and HFL13 is given by $N_{\mathrm{HFL5} \bigcap \mathrm{HFL13}}$. The percentage of the total number of events accepted by the triggers which fired both HFL5 and HFL13 was $\sim 51\%$ and the percentages of the total number of triggered events which fired HFL5 or HFL13 alone were $\sim 35\%$ and $\sim 13\%$ respectively.

Efficiency of trigger slot HFL5

Figures 5.1(a) and (b) show the trigger efficiency of HFL5 for data and MC as a function of p_T and η of the second jet in the event respectively. Figures 5.1(c) and (d) show the ratios of the data and MC efficiencies, again as functions of p_T and η of the second jet. The efficiency is higher in the MC than in the data. This difference is constant as a function of η as shown in Fig. 5.1(d), but is only present for values of $p_T^{j2} < 11.5$ GeV and decreases with increasing p_T^{j2}. A straight line fit in this region yields a functional form for the correction to be applied and is shown in Fig. 5.1(c). As a result of the discrepancy a weight, w_{HFL5}, is applied to MC events firing trigger slot HFL5 only and lying in the range $6 < p_T^{j2} < 11.5$ GeV which is of the form: $w_{HFL5} = 0.031 p_T^{j2} + 0.638$.

Efficiency of trigger slot HFL13

The same distributions were plotted for the efficiency of trigger slot HFL13 but as a function of the p_T and η of the muon and are shown in Fig. 5.2. In this case, the data and MC efficiencies are consistent with an efficiency of $\sim 60\%$ except for a small difference in the rear-η^μ region. This was corrected for by applying a weight, $w_{HFL13} = 0.82$, to MC events firing trigger slot HFL13 only with a muon lying in the range $-1.6 < \eta^\mu < -0.75$. Events firing both trigger slots HFL5 and HFL13 were weighted by the following combination, w, of the HFL5 and HFL13 trigger efficiency correction factors:

$$w = w_{HFL5} + w_{HFL13} - w_{HFL5}.w_{HFL13} \tag{5.3}$$

5.2 Selection of photoproduction events

Photoproduction events are those with photon virtuality $Q^2 \sim 0$ GeV^2, as described in Section 1.1. In this analysis the first step in offline event selection is the rejection of DIS background.

5.2.1 Rejection of reconstructed electron

Deep inelastic scattering events are characterised by a lepton which is scattered through a sizeable angle. This is in contrast to photoproduction events in which the lepton escapes undetected in the beampipe. Therefore, events in which a scattered electron is reconstructed are rejected using an "electron finder" called SINISTRA [65]. This is a package which analyses energy deposits in the calorimeter and, using a neural network, calculates the probability that a cluster is an

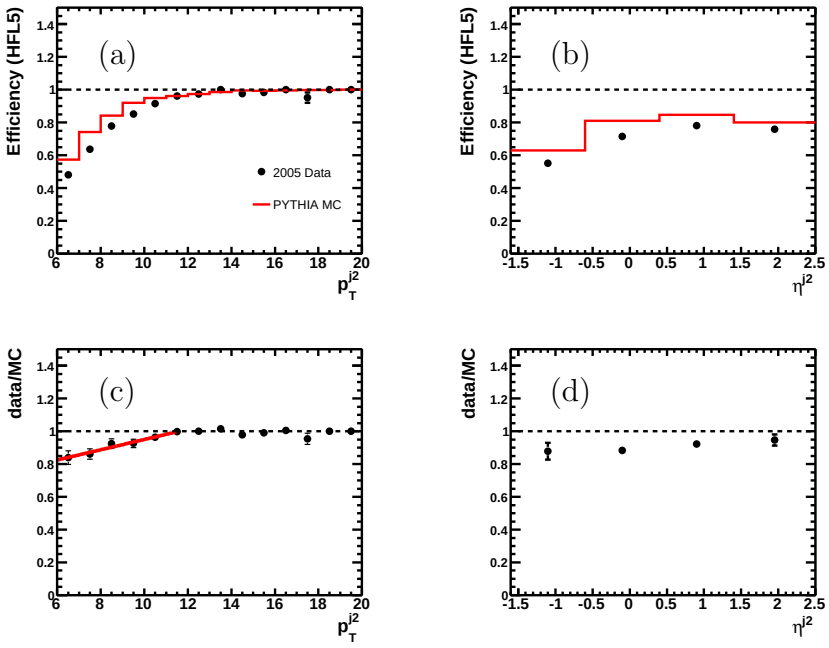

Figure 5.1: Efficiency of trigger slot HFL5 for data (points) and MC (solid line) as a function of (a) p_T and (b) η of the second jet and the ratio of data and MC efficiencies also as a function of (c) p_T and (d) η of the second jet.

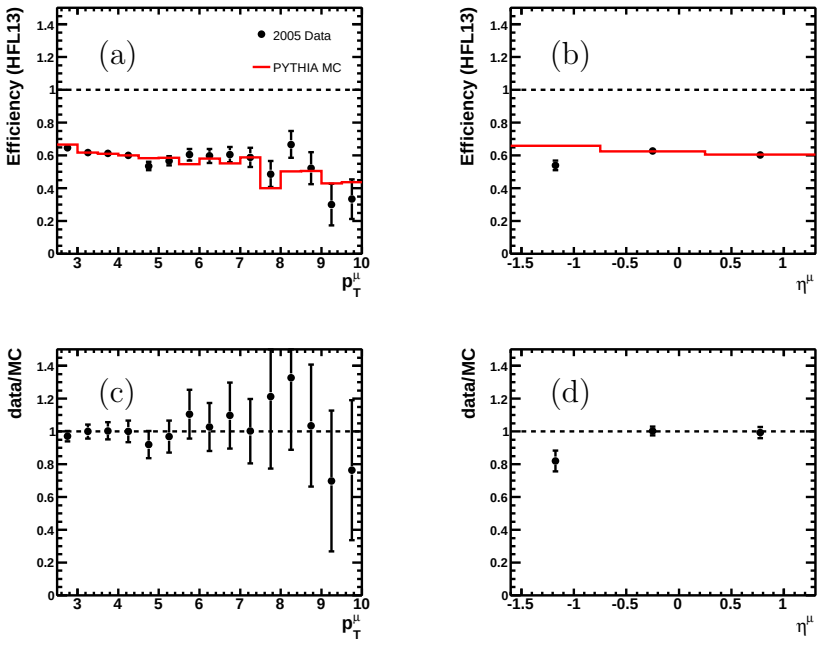

Figure 5.2: Efficiency of trigger slot HFL13 for data (points) and MC (solid line) as a function of (a) p_T and (b) η of the muon and the ratio of data and MC efficiencies as a function of (c) p_T and (d) η of the muon.

electromagnetic or a hadronic cluster. In this analysis, SINISTRA analysed calorimeter deposits only and did not use CTD information. This is because in the majority of DIS events, the lepton is scattered through a small angle, outside the acceptance of the CTD. SINISTRA then selects a lepton from the list of candidates in an event provided the probability that the candidate is an electron, $\mathrm{Prob_{el}} > 0.9$. Events with a reconstructed SINISTRA electron are rejected if they satisfy the following criteria:

$$E_{\mathrm{el}} > 5 \text{ GeV and } \mathrm{y_{el}} < 0.9, \tag{5.4}$$

where E_{el} and y_{el} are the energy and inelasticity of the electron candidate respectively. Final state pions, electrons or photons can be misidentified as scattered electrons and by making the requirements of Equation 5.4 reduces the risk of rejecting photoproduction events wrongly identified as DIS.

5.3 Reconstruction of y

The inelasticity, y, of a DIS event can be found using a number of different methods. Since events in which there is a scattered lepton reconstructed in the detector have been rejected, y cannot be calculated using the electron variables. In fact it is calculated using the hadronic final state, using the Jacquet-Blondel method [66]. This method uses the sum over all the final state particles except the scattered lepton:

$$y_{\mathrm{JB}} = \sum_i \frac{(E_i - p_{z,i})}{2E_e}, \tag{5.5}$$

where E_i and $p_{z,i}$ are the energy and z-component of momentum of the EFO, i, since experimentally the information about the hadrons themselves is not known, and E_e is the energy of the incoming electron. In some DIS events where the lepton is not reconstructed, the lepton energy contributes to the sum, yielding an artificially high $y_{JB} \sim 1$. Such events are identified in this analysis as DIS contamination and removed by the requirement $y_{JB} < 0.8$.

5.4 Rejection of beam gas events

Beam gas events are characterised by energy deposits around the beam pipe and also by unbalanced p_T. To remove these events the following requirements were applied to the EFOs:

- $E_{T,\text{rings}} \geq 10$ GeV, where $E_{T,\text{rings}}$ is the total E_T measured in all CAL cells except those in the 2 inner rings of the FCAL;
- $\frac{p_T}{E_T} < 0.5$;
- $p_T \leq 10$ GeV.

Beam gas events also have a large number of tracks which do not point back to the vertex and so the following cuts were applied:

- the number of vertex fitted tracks > 2;
- $\frac{\text{total number of tracks}}{\text{number of vertex fitted tracks}} \leq 10$.

A cut was also made on y_{JB} to remove misidentified beam gas events which have energy in the forward region only resulting in a low y_{JB}:

- $y_{\text{JB}} > 0.2$

5.5 Event selection

Events with one muon and two jets were selected by requiring:

- ≥ 1 muon with pseudorapidity $-1.6 < \eta^{\mu} < 1.3$, and transverse momentum $p_T^{\mu} > 2.5$ GeV (this cut was lowered to $p_T^{\mu} > 1.5$ GeV for the measurement of the differential cross section with respect to p_T^{μ}); the muon track was required to have at least 4 MVD hits;
- ≥ 2 jets with pseudorapidity $|\eta^j| < 2.5$, and transverse momentum $p_T^j > 7$ GeV for the highest-p_T^j jet and $p_T^j > 6$ GeV for the second-highest-p_T^j jet;
- that muons were associated with jets using the k_T algorithm; if the EFO corresponding to a reconstructed muon was included in a jet then the muon was considered to be associated with the jet, which will from now on be referred to as the muon-jet;
- that the muon was associated with a jet with $p_T^j > 6$ GeV which is not necessarily one of the two highest-p_T jets. To ensure a reliable p_T^{rel} measurement (see Section 6.1), the residual jet transverse momentum, calculated excluding the associated muon, was required to be greater than 2 GeV;

- that the vertex position in Z, $|Z_{vertex}| < 40$ cm.

After all the selection cuts, a sample of 7351 events remained for $p_T^\mu > 2.5$ GeV and 14172 events remained for $p_T^\mu > 1.5$ GeV.

5.6 Monte Carlo samples

In this analysis, MC samples were used to separate signal from background and so events were generated simulating both signal and background processes. Monte Carlo samples of beauty, charm and light-flavour events were generated corresponding respectively to 9, 4.5 and 1 times the luminosity of the data. All samples were produced using PYTHIA 6.2.

5.6.1 Beauty event simulation

At LO beauty quarks are produced predominantly though boson-gluon fusion but other processes also form contributions to the cross section. Resolved photoproduction, as described in Section 1.6, and processes in which a b quark is extracted from the photon or proton parton density, give smaller but still significant contributions. Four different beauty MC samples were generated corresponding to these different production processes:

- b in direct photoproduction:

$$\gamma g \rightarrow b\bar{b};$$

- b in resolved photoproduction:

$$q\bar{q} \rightarrow b\bar{b};$$
$$gg \rightarrow b\bar{b};$$

- b in γ:

$$bq \rightarrow bq;$$
$$bg \rightarrow bg;$$

- b in p:

$$b\gamma \rightarrow b\gamma;$$
$$bg \rightarrow bg;$$
$$bq \rightarrow bq;$$
$$b\bar{b} \rightarrow b\bar{b};$$

These samples were combined according to the cross sections given by PYTHIA and shown in Table 5.1. The contributions of processes where a b quark is extracted from the proton or photon to the total $b\bar{b}$ cross section is about 27%. The parton density CTEQ5L [67] was used for the proton and GRVG-LO [68] for the photon; the b-quark mass was set to 4.75 GeV and the b-quark string fragmentation was performed according to the Peterson function with $\epsilon = 0.0041$ [69]. The beauty quarks were not forced to decay into muons and so the fraction of b decays into muons was given by the branching fraction implemented in the generation according to the value given by the Particle Data Group [70].

5.6.2 Charm event simulation

The production processes of charm are the same as for beauty and so equivalent samples were generated. Again, the samples were combined according to the cross sections given by PYTHIA and shown in Table 5.1. The c quark mass was set to 1.35 GeV and the events were required to contain 2 jets each with:

- $E_T^j \geq 4$ GeV
- $|\eta^j| < 3$

5.6.3 Light flavour event simulation

Due to the low mass of the quarks, production of light flavour (LF) events is dominated by resolved photoproduction. In this sample, direct and resolved photoproduction processes were generated. As with the charm sample, the events contained 2 jets with the same E_T^j and $|\eta^j|$ requirements and the generation cross sections are shown in Table 5.1. Events containing b and c quarks were removed from the sample.

process	σ (pb)	luminosity (pb^{-1})
b in direct PHP	4103	1293
b in resolved PHP	706	1248
b excitation in γ	1343	1268
b excitation in p	410	1280
c in direct PHP	148959	614
c in resolved PHP	11774	665
c excitation in γ	263984	634
c excitation in p	55967	595
LF in direct PHP	664627	133
LF in resolved PHP	7539270	135

Table 5.1: Cross sections and luminosities of the MC samples used in this thesis.

5.7 Muon efficiency corrections

Since this analysis relies on the correct MC simulation of the detector response, a correction has been applied to the MC samples to account for a difference in the efficiency between the data and MC reconstruction. This correction is applied offline on an event by event basis and is calculated using a well understood sample, namely $J/\psi \to \mu^+\mu^-$ events. This process was chosen because of its clean event topology of 2 muons in the final state, where one muon is triggered and the efficiency of the other can be measured. More details of the selection and study of these events can be found in [58, 71]. If both muons fired the trigger, then both are included in the correction since each one is included because of the other and so is unbiased by the trigger. The efficiency of the BREMAT muon finder (see Section 4.3) in the data and the MC is then determined by the fraction of muons reconstructed by BREMAT and by another muon finder, MV [1]:

$$\epsilon = \frac{N_{MV \bigcap BREMAT}}{N_{MV}}, \tag{5.6}$$

and the correction, c, applied to MC events is calculated as the ratio of the efficiencies in data and MC:

$$c = \frac{\epsilon^{data}}{\epsilon^{MC}}. \tag{5.7}$$

[1] MV is a reconstruction algorithm suitable for the identification of isolated muons. It matches CAL cell patterns to CTD tracks.

These corrections were calculated in bins of p_T^μ and η^μ by the ZEUS collaboration muon group and were provided as factors which were then applied in this analysis, also in bins of p_T^μ and η^μ. The dependence of the correction factors on these variables is largely due to geometrical effects of the detector.

5.8 Control distributions

Figure 5.3 shows the distributions of the kinematic variables p_T^μ and η^μ as well as those for the jet associated with the muon $p_T^{\mu\text{-}j}$ and $\eta^{\mu\text{-}j}$. Also shown is the distribution of x_γ^{jj}. The data are compared in shape to the MC simulations in which the relative contributions of beauty, charm and LF were mixed according to the fractions measured in this analysis as described in Chapter 6. The comparison shows that the data are generally well described by the MC. In the η^μ distribution, and correspondingly in the $\eta^{\mu\text{-}j}$ distribution, an apparent shift of the data to larger η with respect to the MC can be seen.

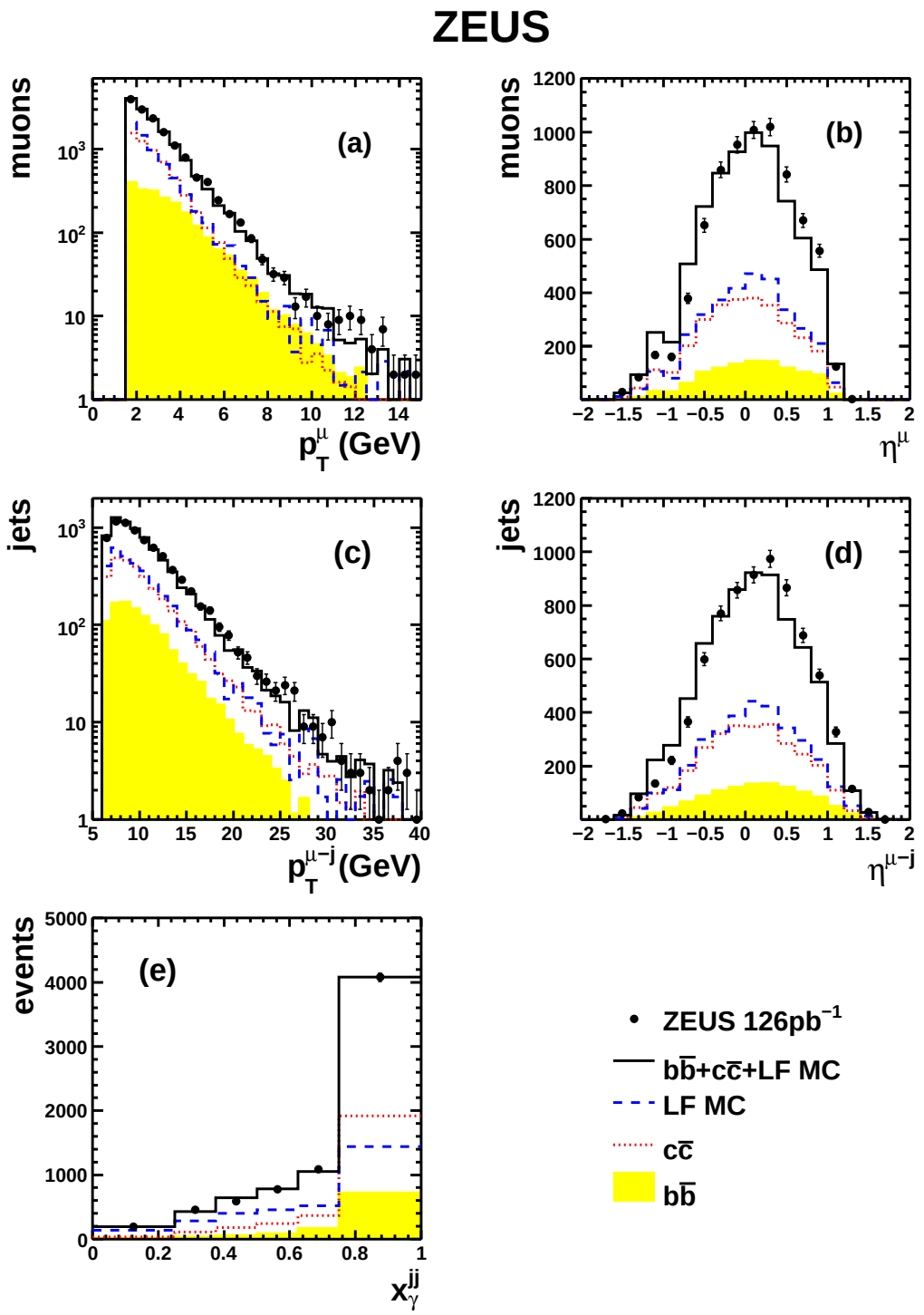

Figure 5.3: Distributions of (a) p_T^μ, (b) η^μ, (c) $p_T^{\mu-j}$, (d) $\eta^{\mu-j}$ and (e) x_γ^{jj}. The data are compared to a mixture of beauty (shaded histogram), charm (dotted line) and light flavour (dashed line) PYTHIA MC predictions, combined according to the fractions given by the two-dimensional p_T^{rel}-δ fit. The total MC distribution is shown as the solid line. The kinematic region is restricted to $p_T^\mu > 1.5$ GeV ($p_T^\mu > 2.5$ GeV) for (a)((b)-(e)).

Chapter 6

Beauty quark identification

In the analysis presented here, events with at least two jets were selected and b quarks were identified through their semi-leptonic decay into muons. The branching ratio for this decay channel is acceptably large ($\sim 10\%$) and the muon provided a clean signature since it is minimally ionising and could traverse the inner detector components to reach the muon chambers, whereas other particles were stopped before the muon detection system. Thus, in this analysis, beauty in photoproduction has been studied in the following decay chain:

$$ep \rightarrow eb\bar{b}X \rightarrow ejj\mu X \tag{6.1}$$

The major backgrounds to this process were $c\bar{c}$ production and processes in which final state hadrons were wrongly identified as muons. The mechanism for $c\bar{c}$ production in ep collisions is essentially the same as for $b\bar{b}$ production and the semi-leptonic decay of charm to muons also has a branching ratio of $\sim 10\%$. Since the $c\bar{c}$ production cross section was much higher at HERA than that of $b\bar{b}$ production and the final state topologies of the two were very similar, this process represented an important background in this analysis. Another possible background was due to the misidentification of hadrons, such as pions or kaons, as muons in the muon chambers. Although these particles had a low probability of reaching the muon chambers, they were produced copiously at HERA and so formed another large background component.

In this analysis the fraction of beauty quarks in the sample is extracted using a statistical method, exploiting both the large mass of the b quark and the long lifetime of the B hadron to separate signal and background.

6.1 The $p_T^{\rm rel}$ method

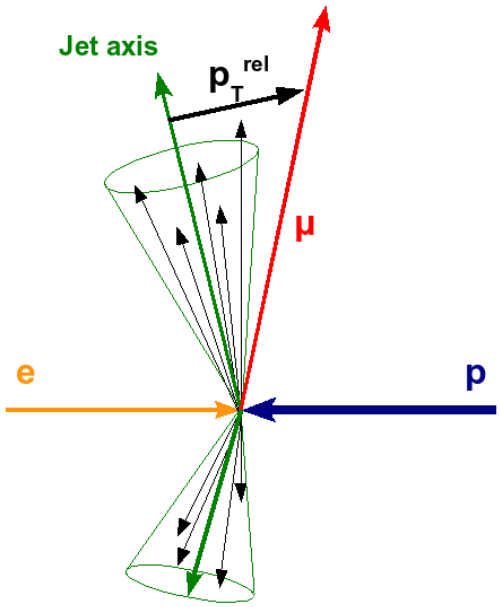

Figure 6.1: Illustration of the $p_T^{\rm rel}$ variable.

The mass of the b quark is approximately 3 times the mass of the c quark. As a result, it is to be expected that the decay products of the B hadron will have a harder transverse momentum spectrum compared with the products of charm decay. In particular, muons from semi-leptonic beauty decays tend to be produced with high transverse momentum with respect to the direction of the mother B hadron,

$$p_{T,\rm true}^{\rm rel} = |\vec{p}_{T,\rm true}^{\rm rel}| = |\vec{p}^{\,\mu} \times \hat{p}^{\,\rm had}| = \frac{|\vec{p}^{\,\mu} \times \vec{p}^{\,\rm had}|}{|\vec{p}^{\,\rm had}|}, \tag{6.2}$$

where $\vec{p}^{\,\mu}$ is the muon momentum vector, $\hat{p}^{\,\rm had}$ is the unit vector along the B-hadron direction and $\vec{p}^{\,\rm had}$ is the B hadron momentum vector. Since B hadrons rapidly decay, their direction is approximated by that of the jet associated with the muon, as shown in Fig. 6.1. The transverse momentum of the muon relative to this associated jet (which includes the muon) is given by

$$p_T^{\rm rel,incl.} = \frac{|\vec{p}^{\,\mu} \times \vec{p}^{\,j}|}{|\vec{p}^{\,j}|}, \tag{6.3}$$

where $\vec{p}^{\,j}$ is the momentum vector of the jet associated with the muon. An alternative definition for $p_T^{\rm rel}$ uses a slightly modified jet axis as a reference by subtracting the muon momentum from the

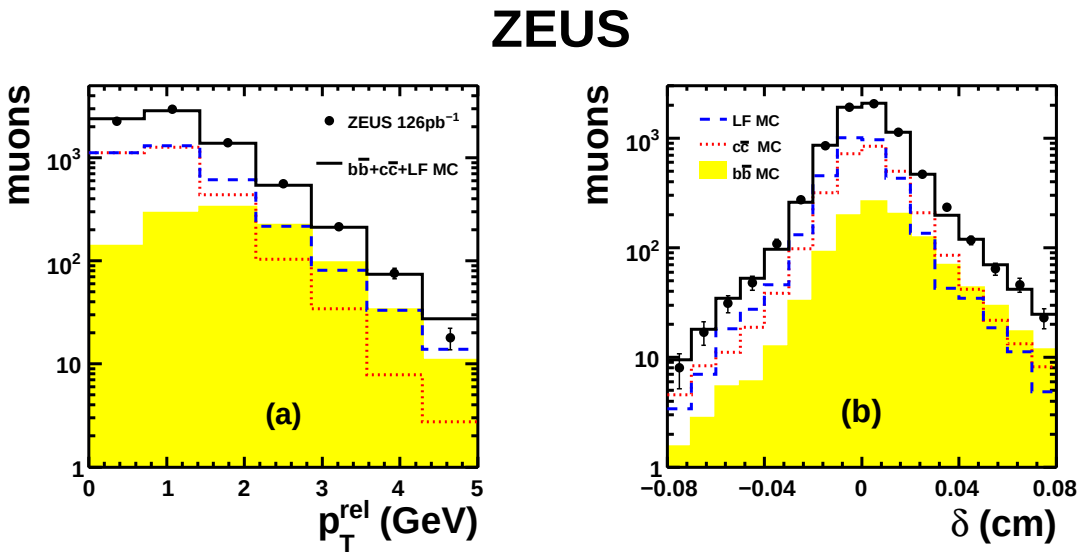

Figure 6.2: Distributions of (a) p_T^{rel} and (b) the muon impact parameter, δ. The data are compared to a mixture of beauty (shaded histogram), charm (dotted line) and light flavour(dashed line) PYTHIA MC samples. The total MC distribution is shown as the solid line. The relative contributions of beauty, charm and light flavour were mixed according to the fractions measured in this analysis as described in Sec.6.4.

jet momentum, thus shifting the p_T^{rel} spectrum to larger values. Subtracting the muon momentum enhances the discriminating power of the p_T^{rel} variable, since a jet axis defined including the muon would be correlated to the muon track's momentum, and hence would diminish its discriminating power. This is especially important in the case of low track multiplicity jets, in which the muon has the possibility to strongly influence the definition of the jet axis. This definition is used in this analysis and is given by

$$p_T^{rel} = \frac{|\vec{p}^{\,\mu} \times (\vec{p}^{\,j} - \vec{p}^{\,\mu})|}{|\vec{p}^{\,j} - \vec{p}^{\,\mu}|}. \tag{6.4}$$

Figure 6.2(b) shows the distribution of p_T^{rel} for the data and the signal ($b\bar{b}$) and background ($c\bar{c}$, LF) MC samples. The p_T^{rel} spectrum for beauty events is harder than for charm or light flavour events and it is this difference which enables a separation of signal and background.

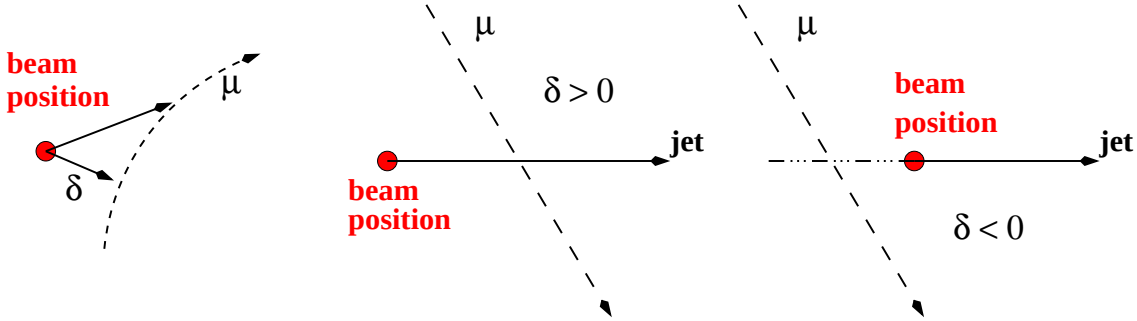

Figure 6.3: Illustration of the signed impact parameter.

6.2 The impact parameter method

The long lifetime of beauty and char m hadrons means that the products of beauty and charm decays are produced at a secondary vertex some distance, L, from the production of the hadron. With very precise position measurements of the decay products, their tracks can be unambiguously associated to the secondary vertex. However, requiring this level of precision leads to a significant loss of signal candidate events. A statistical extraction of the heavy flavour content of a larger sample can be achieved using a variable related to L. The impact parameter, δ, of a particle coming from a hadron decay is defined as the closest distance, in the r-ϕ plane, between the path of the particle's trajectory and the production vertex of the hadron and is given by

$$\delta_{\text{true}} = L_T \sin\alpha, \tag{6.5}$$

where $L_T = L\sin\theta$, θ being the polar angle of the decaying hadron, and α is the angle in the r-ϕ plane between the hadron direction and the direction of the decay product. Experimentally, in semi-leptonic decays producing muons, the impact parameter is the distance of closest approach of the reconstructed muon track to the event primary vertex, given by the beam spot. The direction of the hadron trajectory is approximated by the direction of the axis of the jet associated with the muon.

In semi-leptonic charm and beauty decays, the impact parameter is expected to be a positive non-zero quantity. Therefore this variable can be used to discriminate between heavy flavour events and events involving lighter quarks, for which we would expect an impact parameter of zero.

Introducing a sign to the impact parameter allows a statistical separation of detector resolution effects from the effects of the lifetime of a heavy hadron. The sign of δ is positive if the muon intercepts the axis of the associated jet within the jet hemisphere, otherwise δ is negative, as

shown in Fig. 6.3. A negative δ is an unphysical scenario due to the resolution of the detector. As such, muon tracks originating at the event primary vertex, as in light flavour events, will have a δ spectrum symmetric about zero the width of which reflects the finite track and vertex reconstruction resolution. Decays of beauty and charm hadrons are characterised by the excess seen in the positive δ spectrum. The difference in lifetime between beauty and charm hadrons leads to a significant difference in the δ spectra of the muons in charm and beauty events with beauty events having a harder δ distribution. Figure 6.2(b) shows the muon impact parameter distributions of the data, $b\bar{b}$, $c\bar{c}$ and LF MC samples. The characteristic asymmetric δ distributions of the beauty MC and to a lesser extent, of the charm MC can be clearly seen.

6.3 Comparison between data and MC

Since the beauty content of the data sample is extracted statistically in this method using distributions predicted by the Monte Carlo, it is essential that the discriminating variables, p_T^{rel} and δ are well reproduced by the Monte Carlo description. In this section, the corrections made to these variables are described.

6.3.1 p_T^{rel} correction

In-flight decays of pions and kaons form the largest source of muon candidates in the light flavour background. The p_T^{rel} distribution of the muon background $f_\mu^{\mathrm{bkg}}(p_T^{\mathrm{rel}})$ can be expressed as:

$$f_\mu^{\mathrm{bkg}}(p_T^{\mathrm{rel}}) = f_x^{\mathrm{bkg}}(p_T^{\mathrm{rel}}) P_{x\to\mu}(p_T^{\mathrm{rel}}), \tag{6.6}$$

where $f_x^{\mathrm{bkg}}(p_T^{\mathrm{rel}})$ is the p_T^{rel} distribution of unidentified particle x and $P_{x\to\mu}(p_T^{\mathrm{rel}})$ is the probability that an unidentified particle is identified as a muon. This probability can be determined from Monte Carlo as

$$P_{x\to\mu}(p_T^{\mathrm{rel}}) = \frac{f_\mu^{\mathrm{MC,bkg}}(p_T^{\mathrm{rel}})}{f_x^{\mathrm{MC,bkg}}(p_T^{\mathrm{rel}})}, \tag{6.7}$$

where $f_\mu^{\mathrm{MC,bkg}}(p_T^{\mathrm{rel}})$ and $f_x^{\mathrm{MC,bkg}}(p_T^{\mathrm{rel}})$ are the Monte Carlo muon and unidentified track p_T^{rel} distributions. Therefore, the p_T^{rel} distribution of the muon background can be expressed as a correction to the muon distribution obtained from Monte Carlo:

$$f_{\mu}^{\mathrm{bkg}}(p_T^{\mathrm{rel}}) = f_{\mu}^{\mathrm{MC,bkg}}(p_T^{\mathrm{rel}}) \frac{f_x^{\mathrm{bkg}}(p_T^{\mathrm{rel}})}{f_x^{\mathrm{MC,bkg}}(p_T^{\mathrm{rel}})}. \tag{6.8}$$

This is known as the p_T^{rel} correction. The distribution $f_x^{\mathrm{bkg}}(p_T^{\mathrm{rel}})$ can be obtained from a data sample of dijet events without the requirement of a muon since the beauty contribution in such a sample is very small (2%), i.e.

$$f_x^{\mathrm{bkg}}(p_T^{\mathrm{rel}}) \simeq f_x(p_T^{\mathrm{rel}}). \tag{6.9}$$

This inclusive dijet sample was selected using the same cuts as in the analysis, see Section 5.5, but without the requirement of a muon in the event. Instead, the correction was calculated using all tracks in the event which pass the following quality cuts:

- $p_T > 2.5$ GeV ($p_T > 1.5$ GeV for the p_T^{rel} correction applied to the p_T^{μ} cross section);
- $-1.6 < \eta < 2.3$;
- The track is associated with a jet by the requirement that $\Delta R(\mathrm{track} - \mathrm{jet}) < 1.0$ where $\Delta R(\mathrm{track} - \mathrm{jet}) = \sqrt{(\eta_{\mathrm{track}} - \eta_{\mathrm{jet}})^2 + (\phi_{\mathrm{track}} - \phi_{\mathrm{jet}})^2}$;

The p_T^{rel} value was then calculated for each track. Figure 6.4(a) shows the p_T^{rel} spectrum for the data and MC, normalised to the data. The MC has a more rapid fall off to higher value of p_T^{rel} than the data. The correction factor $\frac{f_x(p_T^{\mathrm{rel}})}{f_x^{\mathrm{MC}}(p_T^{\mathrm{rel}})}$ is shown in Fig 6.4(b) given by the ratio of the data and MC distributions in Fig. 6.4(a). These p_T^{rel} correction factors are calculated for each bin of each cross section measured in this analysis and applied as such to the light flavour MC sample.

Since the charm background is composed not only of a fake muon contribution but also includes muon final states from charm decays, it would not be appropriate to apply the same correction to the charm sample as for the light flavour sample. On the other hand, since it is not possible to extract the p_T^{rel} distribution of charm from the data, such correction factors cannot be calculated directly for charm background. Therefore, as an estimation, 50% of the correction factor applied to the light flavour MC sample was applied to the charm MC sample.

6.3.2 Impact parameter smearing

Using the same inclusive dijet sample as in Section 6.3.1 and plotting the impact parameter distribution for tracks, as in Fig. 6.5, a discrepancy between MC and data is observed. The width of

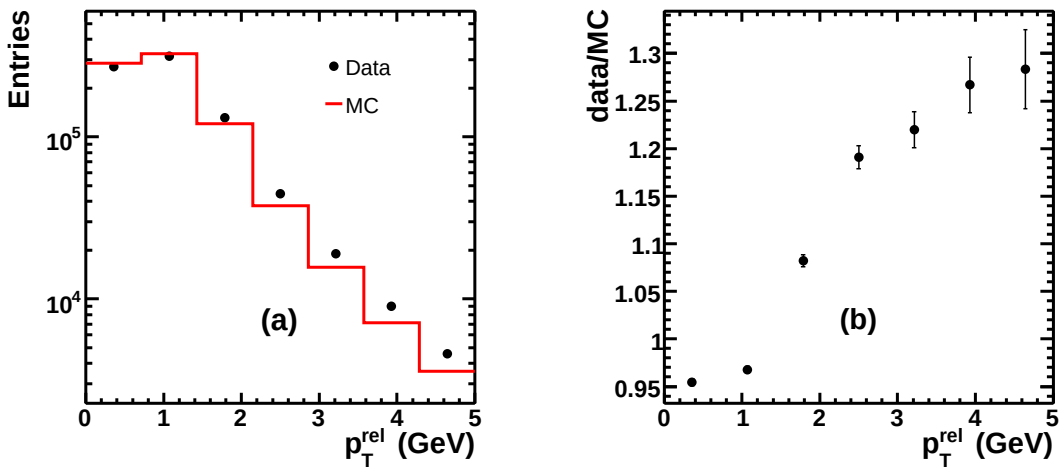

Figure 6.4: (a) p_T^{rel} distribution for inclusive dijet samples of data and PYTHIA MC events (normalised to the data). (b) The ratio of data to MC events as a function of p_T^{rel}.

the δ distribution in the MC is smaller than that of the data. The reasons for this disagreement are related to the following:

- insuffcient accuracy of the dead material simulation;
- intrinsic hit and track resolution overestimating the real tracking detector resolution;
- incomplete version of the alignment of the MVD implemented for this analysis.

A correction can be calculated on the same inclusive data sample so as to reduce the dependence of the correction on Monte Carlo. A full description of the method employed to calculate this correction can be found in [2]. The correction, which was calculated by fitting the data with a double convolution of a Gaussian and a Breit-Wigner distribution, takes the form:

$$\Delta\delta = N_{\mathrm{BW}}(e^{(a-b\cdot p_T^{\mu})} + c)\cdot d + N_{\mathrm{Gauss}}(f + g\cdot p_T^{\mu}), \tag{6.10}$$

where N_{BW} and N_{Gauss} are random numbers which are distributed according to a Breit-Wigner and Gaussian function respectively, both with unit width, and a, b, c, d, f, and g are constants. The correction, which depends on p_T^{μ}, is applied to each MC event in the beauty, charm and light flavour samples in the analysis. Figure 6.6 shows the δ distributions of the inclusive data and MC samples after the application of the correction. The MC description of the data is much improved.

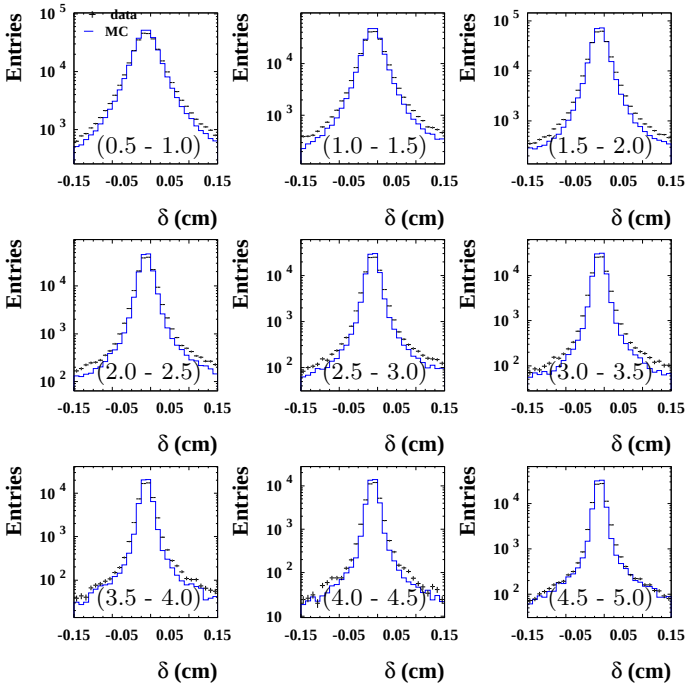

Figure 6.5: MC impact parameter distributions (blue histograms) compared to the data (black points) in bins of p_T (the bin range range for each plot in GeV is given in the brackets). [2, 3] .

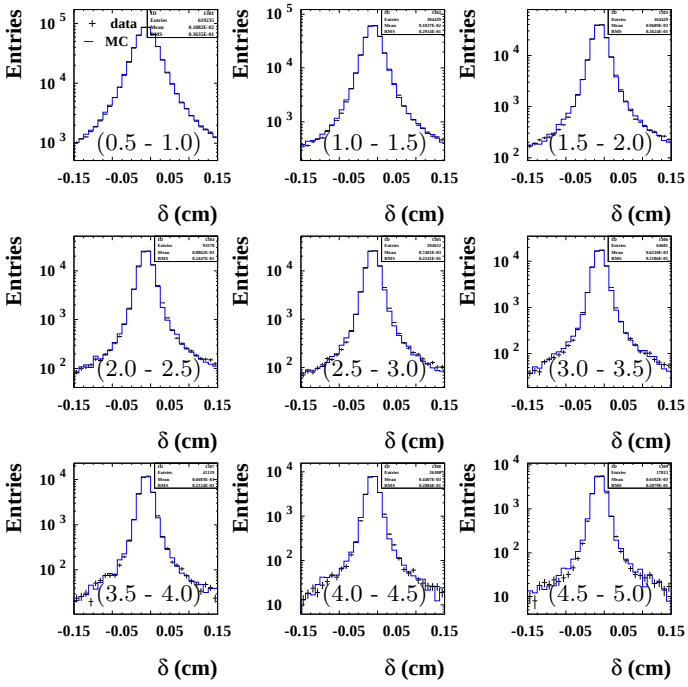

Figure 6.6: MC impact parameter distributions (blue histograms), after the application of smearing correction, compared to the data (black points) in bins of p_T (the bin range range for each plot in GeV is given in the brackets). [2, 3].

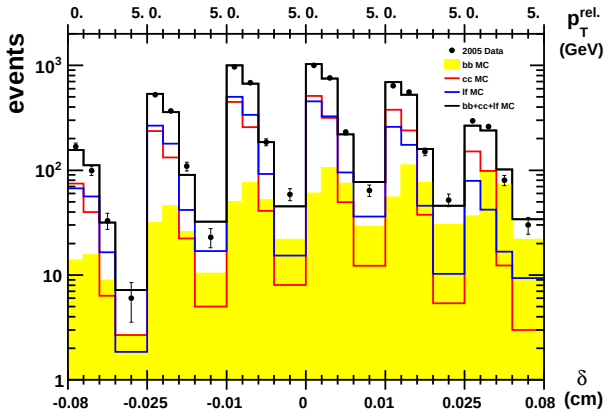

Figure 6.7: Fit of MC distributions to a data distribution of p_T^{rel} in bins of δ.

6.4 Extraction of the beauty fraction

The beauty component of the data sample was determined using the differences in the shapes of distributions of p_T^{rel} and δ for signal and background processes. These distributions were provided by MC simulation and by performing a fit to the data distribution, the fraction of beauty events in the sample was extracted. In order to combine the discriminating properties of the two variables, the fit was made to a two-dimensional distribution of p_T^{rel} in bins of δ, as shown in Fig. 6.7. The fit f was a three component fit:

$$f = a_{b\bar{b}} f^{b\bar{b}} + a_{c\bar{c}} f^{c\bar{c}} + (1 - a_{b\bar{b}} - a_{c\bar{c}}) f^{LF}, \tag{6.11}$$

using the MC predicted shapes for beauty ($f^{b\bar{b}}$), charm ($f^{c\bar{c}}$) and light flavour (f^{LF}) events. Thus the fractions of beauty ($a_{b\bar{b}}$) and charm ($a_{c\bar{c}}$) events were extracted. The fit to the data distribution, f_{data}, used the mimimum-χ^2 method, in which the χ^2 value:

$$\chi^2 = \sum_i^{nbins} \frac{(f_i^{data} - f_i)^2}{\sigma_{i,data}^2 + (a_{b\bar{b}}\sigma_{i,b\bar{b}})^2 + (a_{c\bar{c}}\sigma_{i,c\bar{c}})^2 + ((1 - a_{b\bar{b}} - a_{c\bar{c}})\sigma_{i,LF})^2} \tag{6.12}$$

is calculated iteratively for different values of $a_{b\bar{b}}$ and $a_{c\bar{c}}$ until the minimum is found. The denominator takes into account the statistical uncertainties of the beauty ($\sigma_{b\bar{b}}$), charm ($\sigma_{c\bar{c}}$) and light flavour (σ_{LF}) samples. The fit was repeated in each bin of every cross section. The results of the global fit to complete data sample ($p_T^{\mu} > 2.5$ GeV) are given below.

- $a_{b\bar{b}} = 0.150 \pm^{0.014}_{0.013}$

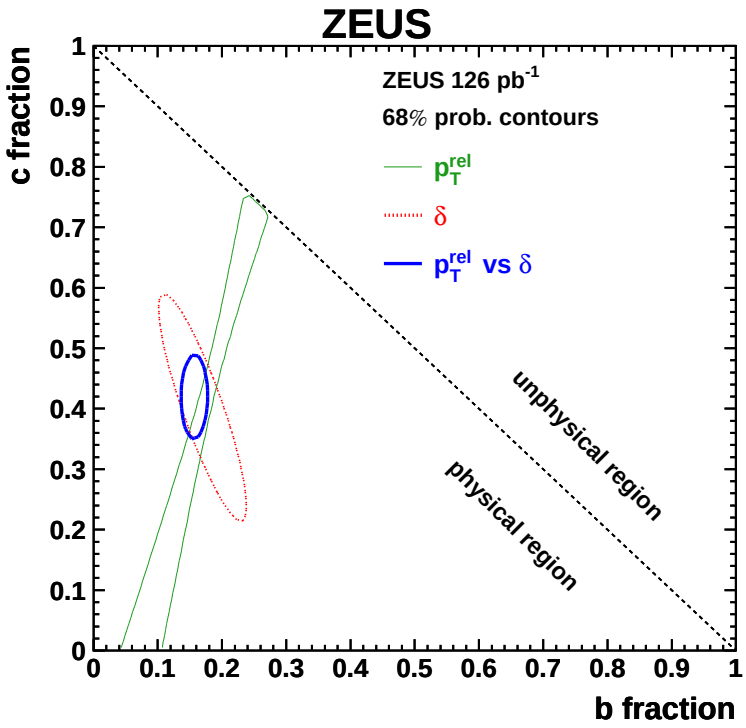

Figure 6.8: Contours of 68% probability in the plane defined by the beauty and charm fractions. The results of the χ^2 fit to the two-dimensional $p_T^{\rm rel}$-δ distribution and to the $p_T^{\rm rel}$ and δ-only distributions are shown. The diagonal line shows the boundary of the physical region in which the fractions of b, c and LF are positive.

- $a_{c\bar{c}} = 0.398 \pm^{0.050}_{0.050}$
- $a_{LF} = 1 - a_{b\bar{b}} - a_{c\bar{c}} = 0.452 \pm^{0.049}_{0.052}$

Figure 6.8 shows the 68% probability contours from the fit described above and also from the the fits carried out using $p_T^{\rm rel}$ or δ alone. It shows that the two variables give complementary information. The $p_T^{\rm rel}$ fit alone is able to distinguish between beauty and the background of charm and LF. It is not able to separate these two backgrounds. On the other hand, the δ fit gives a good determination of the heavy quark content. Using the combination of the two gives a vastly improved result.

Chapter 7

Cross-section measurement

A study of beauty photoproduction in dijet events has been carried out with 126 pb^{-1} of data collected using the ZEUS detector in 2005 [1]. Due to their large mass, the production of b quarks in ep collisions should be accurately calculable in perturbative QCD. Therefore it is interesting to compare such predictions to experimental results. In this chapter, measurements of the total cross section $\sigma(ep \to eb\bar{b}X \to ejj\mu X')$ and differential cross sections as a function of muon and jet variables are presented for beauty production. They are compared to NLO QCD predictions and and Monte Carlo models.

The dijet sample of beauty photoproduction events was also used to study higher-order QCD topologies. At LO, the two jets in the event are produced back-to-back in azimuthal angle, such that $\Delta\phi^{jj} = \phi^{j1} - \phi^{j2} = \pi$. Additional soft radiation causes small azimuthal decorrelations, whilst $\Delta\phi^{jj}$ significantly lower than π is evidence of additional hard radiation. In this chapter, the differential cross section with respect to $\Delta\phi^{jj}$ is also presented for beauty photoproduction and again compared to NLO QCD predictions and Monte Carlo models.

The total and differential visible cross sections were measured for final states with at least one muon and two jets in the following kinematic region:

- $Q^2 < 1\,\text{GeV}^2$ and $0.2 < y < 0.8$;
- $p_T^{j1,j2} > 7,6\,\text{GeV}$ and $|\eta^{j1,j2}| < 2.5$;
- $p_T^{\mu} > 2.5\,\text{GeV}$ ($p_T^{\mu} > 1.5\,\text{GeV}$ for $d\sigma/dp_T^{\mu}$) and $-1.6 < \eta^{\mu} < 1.3$;
- at least one muon is associated with a jet with $p_T^{j} > 6\,\text{GeV}$.

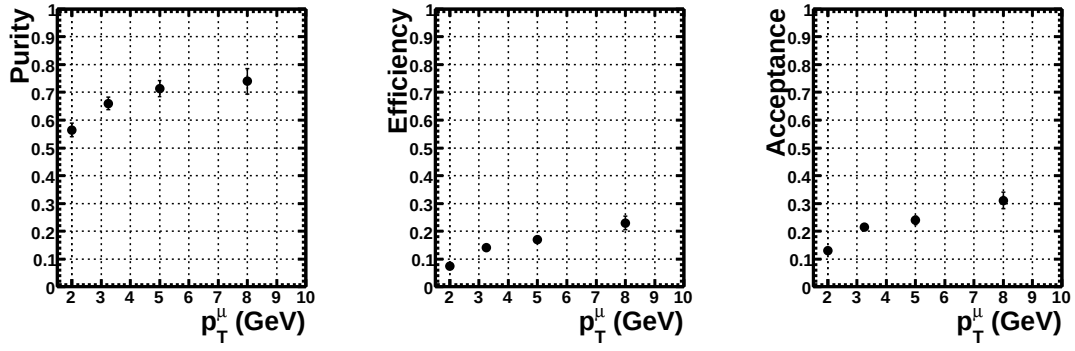

Figure 7.1: Purity, p, efficiency, ϵ and acceptance correction factor, A, for the differential cross section as a function of p_T^μ.

The visible cross section was determined using:

$$\sigma(ep \to eb\bar{b}X \to ejj\mu X') = \frac{a_{b\bar{b}} N_\mu}{A \cdot \mathcal{L}}, \tag{7.1}$$

where $a_{b\bar{b}}$ is the fraction of beauty events in the sample, extracted statistically as described in Section 6.4, N_μ is the number of muon candidates selected from a data set with integrated luminosity $\mathcal{L}$. The acceptance correction, A, which takes into account migration of events from bin to bin and the reconstruction inefficiency is described in Section 7.1.

A visible differential cross section with respect to a variable Y is given by a corresponding formula,

$$\frac{d\sigma}{dY} = \frac{a_{b\bar{b}}(i) N_\mu(i)}{A(i) \cdot \mathcal{L} \cdot \Delta Y_i}, \tag{7.2}$$

where $a_{b\bar{b}}(i)$, $N_\mu(i)$ and $A(i)$ are the beauty fraction, number of muon candidates and acceptance correction respectively in a given bin, i, of width ΔY_i.

7.1 Purities, efficiencies and acceptance corrections

In order to obtain a cross section from detector level quantities, the purity, efficiency and acceptance correction were calculated in each bin using PYTHIA MC. The purity, $p(i)$, and efficiency, $\epsilon(i)$, are given by,

$$p(i) = \frac{N_{rec \cap gen}(i)}{N_{rec}(i)}, \tag{7.3}$$

$$\epsilon(i) = \frac{N_{rec \cap gen}(i)}{N_{gen}(i)}, \tag{7.4}$$

where $N_{rec}(i)$ is the number of reconstructed events and $N_{gen}(i)$ is the number of events generated in bin i which pass the kinematic cuts. $N_{rec \cap gen}(i)$ is the number of events which are generated and reconstructed in the same bin, i. The purity can therefore be interpreted as the fraction of reconstructed events in a certain bin which were originally generated in that bin. Similarly, the efficiency can be interpreted as the fraction of generated events which were then reconstructed in the same bin. The acceptance correction, $A(i)$, can be calculated from the purity and efficiency as,

$$A(i) = \frac{\epsilon(i)}{p(i)}. \tag{7.5}$$

The purity, efficiency and acceptance correction as functions of p_T^μ are shown in Fig. 7.1. For all other variables, these figures are included in Appendix A. The efficiency includes the muon efficiency corrections and so low values can be attributed in part to the inefficiency in muon reconstruction.

7.2 Determination of the systematic uncertainties

The following sources of systematic uncertainty were considered. The resulting uncertainty on the total cross section is given in parentheses and the uncertainties on the differential cross sections are given in Appendix B. The total systematic uncertainty is determined by summing these contributions in quadrature.

Muon acceptance

The uncertainty on the muon acceptance, including the efficiency of the muon chambers, of the reconstruction and of the B/RMUON matching to central tracks has been determined in a study based on a dimuon sample, as described in Section 5.7. The efficiency of the muon trigger in the MC was corrected so that it reproduced the efficiency as measured in the data, as described in Section 5.1.1. The size of the correction was varied within its uncertainties. These variations were carried out simultaneously ($\pm 7\%$).

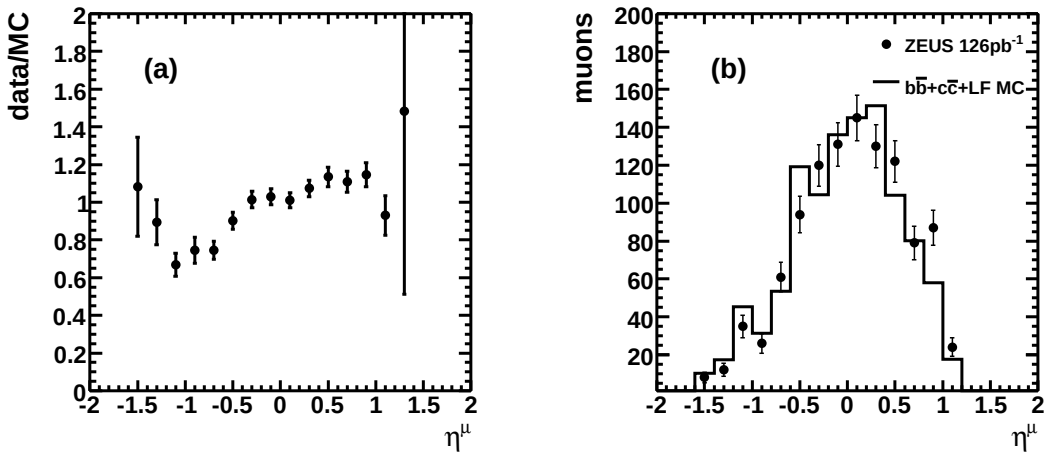

Figure 7.2: (a) The factors used to reweight the MC taken from the ratio of the numbers of data and MC events in bins of η_μ. (b) Comparison of η_μ control distribution for data and MC for beauty-enriched samples obtained by the requirement of $p_T^{\mathrm{rel}} > 2\,\mathrm{GeV}$

Energy scale

The absolute energy scale of the calorimeter is known to be reproduced by the MC to within ±3%. Therefore the error due to the uncertainty of the energy scale was evaluated by varying the energy of the jets and the inelasticity y_{JB} in the MC by ±3% (±4%).

MVD efficiency

The efficiency of finding a track with 4 MVD hits in an inclusive sample of CTD tracks ($p_T >$ 2.5 GeV, $0.55 < \theta < 2.75$) was measured in the data and in the MC. The ratio of the measured efficiencies was found to be 0.94 and was applied as a correction to the acceptance. The uncertainty on this ratio was included as a systematic uncertainty (±3%).

Dijet trigger efficiency

The efficiency of the dijet trigger in the MC was corrected so that it reproduced the efficiency as measured in the data, as described in Section 5.1.1. The systematic uncertainty on the size of this correction was negligible.

η_μ MC description

The data η_μ distribution was not well described by the MC simulation. As shown in Fig. 5.3(b), the MC distribution is shifted to lower values of η_μ with respect to the data. As a systematic

check, MC events were weighted, in order to account for these differences, by factors taken from the ratio of the data and MC in each bin of the η_μ distribution. Each MC event was given the weight corresponding to the bin containing the highest-p_T muon in the event. The factors are shown in Fig. 7.2(a). The discrepancy in η_μ control distribution was also present in a signal enhanced sample (using the requirement $p_T^{\mathrm{rel}} > 2\,\mathrm{GeV}$), as shown in Fig. 7.2(b), and therefore the reweighting was applied to both signal and background MC samples. The resulting variation in the cross section was found to be largest in $\frac{d\sigma}{d\eta^\mu}$ and $\frac{d\sigma}{d\eta^{\mu-j}}$, however the effect on the total cross section was negligible ($< 1\%$).

Impact parameter correction

The uncertainty on the size of the correction to the shape of the impact parameter distribution for the MC samples, as described in Section 6.3.2, was evaluated by varying the widths of the Gaussian and Breit-Wigner distributions used in the correction function by $+20\%$ and -10% of their nominal values. These variations are such that the global MC distribution still provides a good description of the data ($^{+6\%}_{-10\%}$).

p_T^{rel} correction

The uncertainty on the p_T^{rel} shape of the LF and charm background was evaluated by:

- varying the correction applied to the LF background by $\pm 20\%$ of its nominal value ($\pm 2\%$).
- varying the p_T^{rel} shape of the charm component by removing or doubling the correction applied ($\pm 4\%$).

Physics process contributions in MC

The contributions of processes to the overall MC samples are combined according to the corresponding production cross sections taken from the Pythia MC prediction. The uncertainty on these MC model cross sections is estimated in the following way.

The contribution of processes in which a b quark comes from the proton or photon in Pythia was varied by $+100\%/-50\%$ and simultaneously the contribution of $gg \to b\bar{b}$, $q\bar{q} \to b\bar{b}$ events was varied by $-50\%/+100\%$. Figure 7.3(a) shows the change in shape of the MC distribution of $\frac{d\sigma}{dx_\gamma^{jj}}$ when these variations are made ($\pm 4\%$).

The contribution of $\gamma g \to b\bar{b}$ processes in Pythia was decreased by 20% and all other processes were increased by $+100\%$. The change in shape of the $\frac{d\sigma}{dx_\gamma^{jj}}$ MC distribution is shown in Fig. 7.3(b) ($\pm 2\%$).

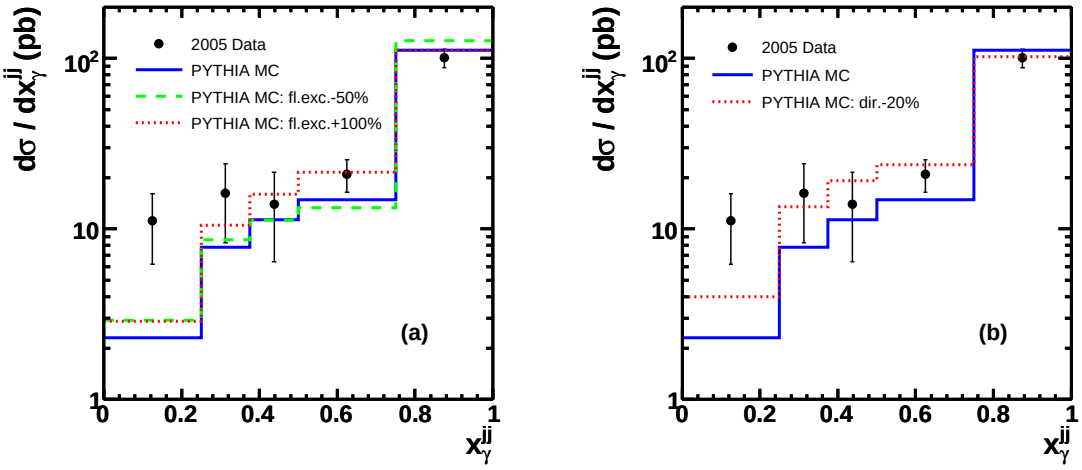

Figure 7.3: $\frac{d\sigma}{dx_\gamma^{jj}}$ for data and nominal PYTHIA MC samples. Also shown are $\frac{d\sigma}{dx_\gamma^{jj}}$ for PYTHIA MC samples in which (a) the contribution of flavour-excitation events was varied by $+100\%/-50\%$ and simultaneously the contribution of $gg \to b\bar{b}$, $q\bar{q} \to b\bar{b}$ events was varied by $-50\%/+100\%$ and (b) the contribution of $\gamma g \to b\bar{b}$ processes was decreased by 20% and all other processes were increased by +100%

The size of these variations were such that the comparison between MC and data for $\frac{d\sigma}{dx_{d\gamma}^{jj}}$ was still satisfactory (see Fig. 7.3).

7.3 Theoretical predictions

The measured cross sections are compared to NLO QCD predictions based on the FMNR [19] program. The parton distribution functions used for the nominal prediction were GRVG-HO [68] for the photon and CTEQ5M [67] for the proton. The b-quark mass was set to $m_b = 4.75$ GeV, and the renormalisation and factorisation scales to the transverse mass, $\mu_r = \mu_f = m_T = \sqrt{\frac{1}{2}\left((p_T^b)^2 + (p_T^{\bar{b}})^2\right) + m_b^2}$, where $p_T^{b(\bar{b})}$ is the transverse momentum of the b ($\bar{b}$) quark in the laboratory frame. Jets were reconstructed by running the k_T algorithm on the four-momenta of the b and $\bar{b}$ quarks and of the third light parton (if present) generated by the program. The fragmentation of the b quark into a B hadron was simulated by rescaling the quark three-momentum (in the frame in which $p_Z^b = -p_Z^{\bar{b}}$, obtained with a boost along Z) according to the Peterson [69] fragmentation function with $\epsilon = 0.0035$. The muon momentum was generated isotropically in the B hadron rest frame from the decay spectrum given by PYTHIA which is in good agreement with measurements made at B factories [72].

The NLO cross sections, calculated for jets made of partons, were corrected for jet hadronisation effects to allow a direct comparison with the measured hadron-level cross sections. The correction factors, $C_{\rm had}$, were derived from the MC simulation as the ratio of the hadron-level to the parton-level MC cross sections. The parton level is defined as being the result of the parton-showering stage of the simulation and the hadron level is defined as the point after hadronisation (see Fig. 2.2). Therefore the factors, $C_{\rm had}$, can be used to correct theoretical predictions, which have partons as the final state, to the hadron level so that they can be compared with the measured cross sections. The corrections were found to be typically small, with a maximum value of $\sim 20\%$, and did not change the shapes of the cross section distributions. Values of $C_{\rm had}$ for each bin of each cross section are given in Tables 7.1, 7.2, 7.3 and 7.4.

To evaluate the uncertainty on the NLO calculations, the b-quark mass and the renormalisation and factorisation scales were varied simultaneously to maximise the change, from $m_b = 4.5$ GeV and $\mu_r = \mu_f = m_T/2$ to $m_b = 5.0$ GeV and $\mu_r = \mu_f = 2m_T$, producing a variation in the cross section from $+34\%$ to -22%. The effect on the cross section of a variation of the Peterson parameter ϵ and of a change of the fragmentation function from the Peterson to the Kartvelishvili parameterisation was found in a previous publication [21] to be of the order of 3%. The effects of using different sets of parton densities and of a variation of the strong coupling constant were found to be within $\pm 4\%$. These effects are negligible with respect to that of a variation of the b-quark mass and the renormalisation and factorisation scales and are therefore not included. The uncertainty due to the hadronisation correction was also found to be negligible with respect to the dominant uncertainty.

7.4 Total cross section

The total visible cross section is

$$\sigma(ep \to eb\bar{b}X \to ejj\mu X') = 38.6 \pm 3.5(\text{stat.})^{+4.6}_{-4.9}(\text{syst.})\ \text{pb}. \tag{7.6}$$

This result is compared to the NLO QCD calculation described in Section 7.3. The prediction for the total visible cross section is

$$\sigma(ep \to eb\bar{b}X \to ejj\mu X') = 39.2^{+14.4}_{-6.9}\ \text{pb}, \tag{7.7}$$

in excellent agreement with the data.

7.5 Muon variable differential cross sections

Figure 7.4 and Tables 7.1 and 7.2 show the visible differential cross sections as a function of p_T^μ, η^μ, $p_T^{\mu-j}$ and $\eta^{\mu-j}$. The visible cross section as a function of p_T^μ is measured in the range $p_T^\mu > 1.5$ GeV, extending the kinematic region to lower p_T^μ than in the previous ZEUS and H1 measurements [21, 22], while the other cross sections are measured for $p_T^\mu > 2.5$ GeV. The NLO QCD predictions describe the data well and the PYTHIA MC also gives a good description of the shapes.

The visible differential cross section as a function of η^μ is also compared with the previous ZEUS measurement [21], which used the p_T^{rel} method to extract the beauty fraction. The two measurements agree well. The measurement presented by H1 [22] refers to a slightly different definition of the cross section and therefore cannot be compared to directly. However a qualitative comparison does not confirm their observation of an excess at low p_T^μ.

7.6 Dijet differential cross sections

Figure 7.5(a) and Table 7.3 show the visible dijet cross section as a function of x_γ^{jj} (Equation 2.11). The x_γ^{jj} variable corresponds at LO to the fraction of the exchanged-photon momentum entering the hard scattering process. In photoproduction, events can be classified into two types of process in LO QCD: direct and resolved processes, as described in Section 1.6. The x_γ^{jj} variable provides a tool to measure the relative importance of direct processes, which gives a peak at $x_\gamma^{jj} \sim 1$, and of resolved processes, which are distributed over the whole x_γ^{jj} range. The measurement presented here shows that the dominant contribution to the visible cross section comes from the high-x_γ^{jj} peak but a low-x_γ^{jj} component is also apparent. The NLO QCD prediction describes the measured visible cross section well. PYTHIA also gives a good description of the shape of the distribution.

Dijet angular correlations are particularly sensitive to higher-order effects and are therefore suitable to test the limitations of fixed-order perturbative QCD calculations. At LO, the differential cross section as a function of $\Delta\phi^{jj}$ is a delta function peaked at π. At NLO, exclusive three-jet production populates the region $\frac{2}{3}\pi < \Delta\phi^{jj} < \pi$, whilst smaller values of $\Delta\phi^{jj}$ require additional radiation such as a fourth jet in the event. However, it should be noted that an NLO QCD calculation can produce values of $\Delta\phi^{jj} < \frac{2}{3}\pi$ when the highest-p_T jet is not in the accepted kinematic region.

The visible differential cross section as a function of $\Delta\phi^{jj}$ is shown in Fig. 7.5(b) and Table 7.4. The NLO QCD predictions describe the data well. Visible cross sections as a function of $\Delta\phi^{jj}$ have

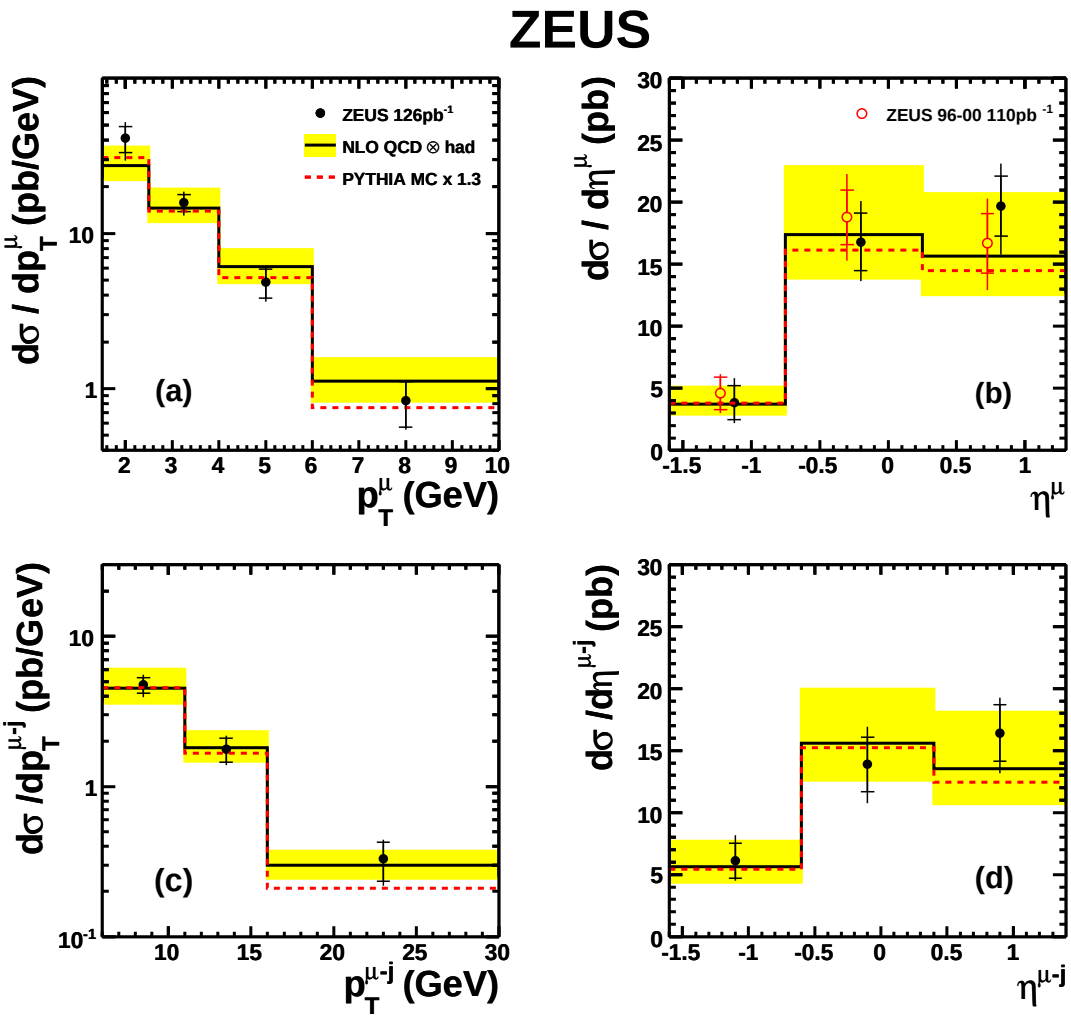

Figure 7.4: Differential cross section as a function (a) p_T^μ, (b) η^μ, (c) $p_T^{\mu-j}$ and (d) $\eta^{\mu-j}$ for $Q^2 < 1$ GeV^2, $0.2 < y < 0.8$, $p_T^{j_1,j_2} > 7,6$ GeV, $|\eta_{j_1,j_2}| < 2.5$, and $-1.6 < \eta^\mu < 1.3$. For the p_T^μ cross section, the kinematic region is defined as $p_T^\mu > 1.5$ GeV and as $p_T^\mu > 2.5$ GeV for all other cross sections. The filled circles show the results from this analysis and the open circles show the results from the previous ZEUS measurement. The inner error bars are statistical uncertainties while the external bars show the statistical and systematic uncertainties added in quadrature. The band represents the NLO QCD predictions with their uncertainties. The PYTHIA MC predictions are also shown (dashed line).

p_T^μ range (GeV)	$d\sigma/dp_T^\mu \pm$ stat. $\pm$ syst. (pb/GeV)	$C_{\rm had}$
1.5, 2.5	$41.05 \pm 7.74^{+8.26}_{-8.51}$	0.87
2.5, 4.0	$15.78 \pm 1.96^{+2.03}_{-1.98}$	0.93
4.0, 6.0	$4.87 \pm 1.03^{+0.69}_{-0.67}$	0.98
6.0, 10.0	$0.84 \pm 0.27^{+0.11}_{-0.11}$	1.01
η^μ range	$d\sigma/d\eta^\mu \pm$ stat. $\pm$ syst. (pb)	$C_{\rm had}$
-1.60,-0.75	$3.86 \pm 1.37^{+1.40}_{-0.92}$	0.83
-0.75, 0.25	$16.81 \pm 2.30^{+2.34}_{-2.15}$	0.89
0.25, 1.30	$19.70 \pm 2.43^{+2.43}_{-3.09}$	0.92

Table 7.1: Differential muon cross section as a function of p_T^μ and η^μ. For further details see text. The multiplicative hadronisation correction, $C_{\rm had}$, applied to the NLO prediction is shown in the last column.

$p_T^{\mu\text{-}j}$ range (GeV)	$d\sigma/dp_T^{\mu\text{-}j} \pm$ stat. $\pm$ syst. (pb/GeV)	$C_{\rm had}$
6, 11	$4.74 \pm 0.57^{+0.60}_{-0.59}$	0.89
11, 16	$1.78 \pm 0.32^{+0.24}_{-0.22}$	0.89
16, 30	$0.33 \pm 0.10^{+0.05}_{-0.05}$	0.92
$\eta^{\mu\text{-}j}$ range	$d\sigma/d\eta^{\mu\text{-}j} \pm$ stat. $\pm$ syst. (pb)	$C_{\rm had}$
-1.6,-0.6	$6.13 \pm 1.41^{+1.50}_{-0.82}$	0.77
-0.6, 0.4	$13.89 \pm 2.20^{+2.08}_{-2.21}$	0.84
0.4, 1.4	$16.42 \pm 2.29^{+1.70}_{-2.29}$	0.99

Table 7.2: Differential cross section for jets associated with a muon as a function of $p_T^{\mu\text{-}j}$ and $\eta^{\mu\text{-}j}$. For further details see text.

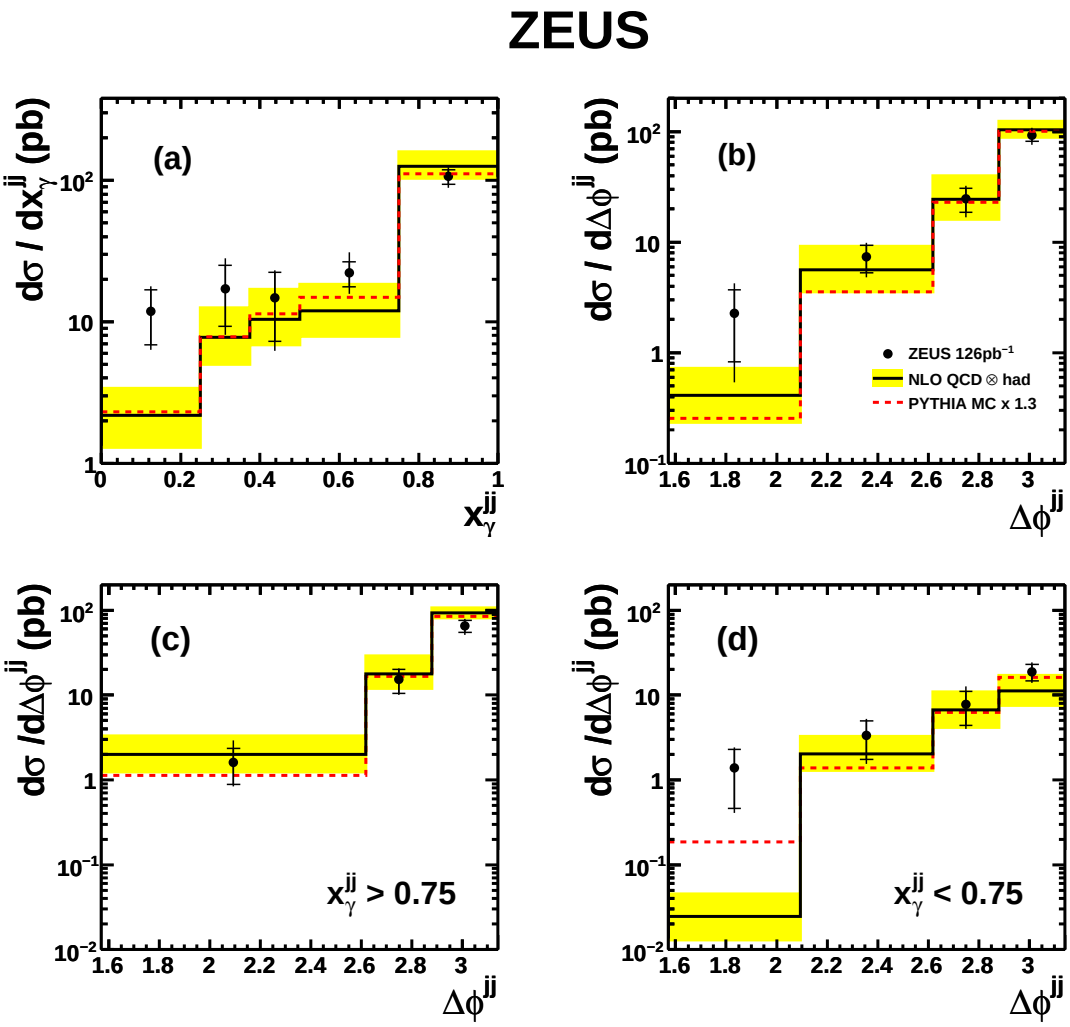

Figure 7.5: Differential cross sections as a function of (a) x_γ^{jj} and (b) $\Delta\phi^{jj}$ of the jet-jet system and $\Delta\phi^{jj}$ for (c) direct- and (d) resolved-enriched samples for $Q^2 < 1$ GeV^2, $0.2 < y < 0.8$, $p_T^{j_1,j_2} > 7,6$ GeV, $\eta_{j_1,j_2} < 2.5$, $p_T^\mu > 2.5$ GeV and $-1.6 < \eta^\mu < 1.3$. The inner error bars are statistical uncertainties while the external bars show the statistical and systematic uncertainties added in quadrature. The band represents the NLO QCD predictions with their uncertainties. The PYTHIA MC predictions are also shown (dashed line).

x_γ^{jj} range	$d\sigma/dx_\gamma^{jj} \pm$ stat. $\pm$ syst. (pb)	$C_{\rm had}$
0.000, 0.250	$11.85\pm\ 4.96\ ^{+3.32}_{-2.40}$	0.69
0.250, 0.375	$17.17\pm\ 7.89\ ^{+7.69}_{-4.47}$	0.78
0.375, 0.500	$14.81\pm\ 7.56\ ^{+3.30}_{-4.06}$	0.86
0.500, 0.750	$22.19\pm\ 4.48\ ^{+7.47}_{-4.51}$	0.86
0.750, 1.000	$106.63\pm12.63\ ^{+11.82}_{-12.74}$	0.92

Table 7.3: Differential cross section as a function of x_γ^{jj}. For further details see text.

$\Delta\phi^{jj}$ range	$d\sigma/d\Delta\phi^{jj} \pm$ stat. $\pm$ syst. (pb)	C_{had}
$\frac{6\pi}{12}$, $\frac{8\pi}{12}$	$2.26\pm\ 1.44\ ^{+1.34}_{-0.96}$	0.80
$\frac{8\pi}{12}$, $\frac{10\pi}{12}$	$7.35\pm\ 2.06\ ^{+1.47}_{-1.45}$	0.79
$\frac{10\pi}{12}$, $\frac{11\pi}{12}$	$24.70\pm\ 6.04\ ^{+4.66}_{-5.12}$	0.86
$\frac{11\pi}{12}$, $\frac{12\pi}{12}$	$92.91\pm11.10\ ^{+10.46}_{-12.82}$	0.92
$x_\gamma^{jj} > 0.75$		
$\Delta\phi^{jj}$ range	$d\sigma/d\Delta\phi^{jj} \pm$ stat. $\pm$ syst. (pb)	C_{had}
$\frac{6\pi}{12}$, $\frac{10\pi}{12}$	$1.62\pm\ 0.73\ ^{+1.08}_{-0.27}$	0.82
$\frac{10\pi}{12}$, $\frac{11\pi}{12}$	$15.27\pm\ 4.75\ ^{+2.50}_{-2.21}$	0.87
$\frac{11\pi}{12}$, $\frac{12\pi}{12}$	$65.69\pm10.66\ ^{+8.14}_{-9.18}$	0.93
$x_\gamma^{jj} < 0.75$		
$\Delta\phi^{jj}$ range	$d\sigma/d\Delta\phi^{jj} \pm$ stat. $\pm$ syst. (pb)	$C_{\rm had}$
$\frac{6\pi}{12}$, $\frac{8\pi}{12}$	$1.38\pm0.92\ ^{+0.46}_{-0.31}$	0.75
$\frac{8\pi}{12}$, $\frac{10\pi}{12}$	$3.36\pm1.60\ ^{+0.97}_{-0.87}$	0.76
$\frac{10\pi}{12}$, $\frac{11\pi}{12}$	$7.75\pm3.37\ ^{+3.67}_{-1.62}$	0.84
$\frac{11\pi}{12}$, $\frac{12\pi}{12}$	$18.84\pm4.17\ ^{+3.71}_{-2.59}$	0.84

Table 7.4: Differential muon cross section as a function of $\Delta\phi^{jj}$ for all x_γ^{jj} and for $x_\gamma^{jj} > (<)0.75$. For further details see text.

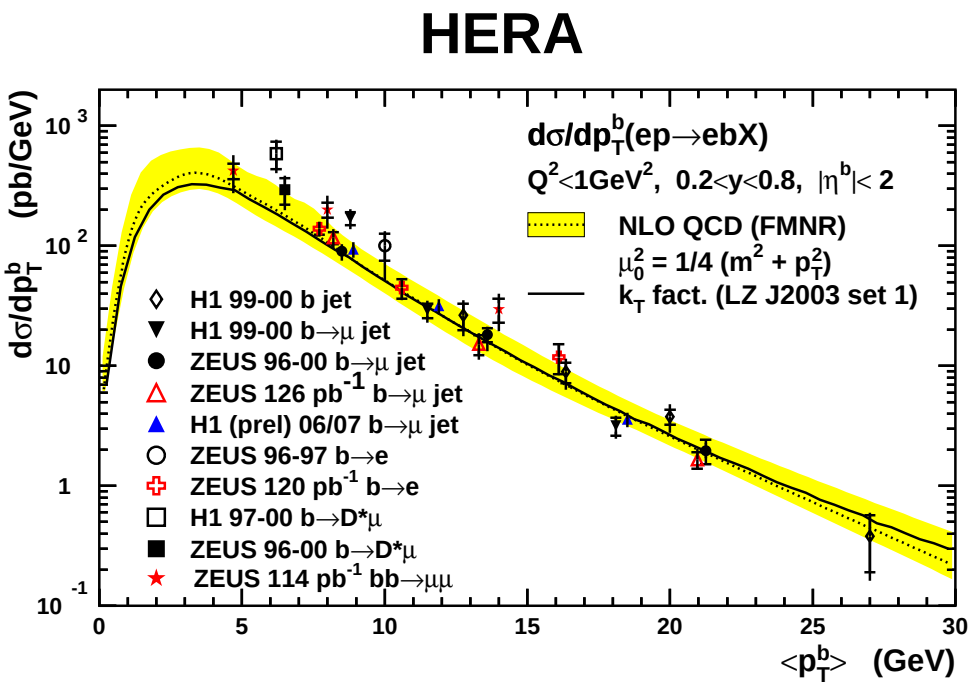

Figure 7.6: Compilation of HERA measurements of the differential cross section for b-quark production as a function of p_T^b. The measurement in this thesis is represented by the open red triangles.

also been measured separately for direct-enriched ($x_\gamma^{jj} > 0.75$) and resolved-enriched ($x_\gamma^{jj} < 0.75$) samples (Fig. 7.5(c) and (d) and Table 7.4) since the resolved-enriched sample should be more sensitive to higher-order topologies. The cross sections are well described by the NLO QCD prediction for $x_\gamma^{jj} > 0.75$ and for $x_\gamma^{jj} < 0.75$. The PYTHIA MC gives an equally good description of the shape of the distributions.

Figure 7.6 shows the comparison of several HERA measurements of beauty in photoproduction. The measurements are shown as differential cross sections as a function of p_T^b obtained by extrapolating from the cross section with respect to $p_T^{\mu-j}$ using the NLO QCD prediction (the values measured in this thesis are also given in Table 7.5). This was achieved by correcting to the b-quark level using

$$\frac{d\sigma(ep \to bX)}{dp_T^b} = \frac{1}{2}\frac{d\sigma^{NLO}(ep \to b(\bar{b})X)}{dp_T^{b(\bar{b})}}\frac{\sigma_{bin}(ep \to ejj\mu X)}{\sigma_{bin}^{NLO}(ep \to ejj\mu X)\cdot C_{had}}, \tag{7.8}$$

where $\sigma_{bin}(ep \to ejj\mu X)$ is the measured cross section as a function of $p_T^{\mu-j}$ in a given bin of $p_T^{\mu-j}$, $\sigma_{bin}^{NLO}(ep \to ejj\mu X)\cdot C_{had}$ is the NLO prediction in that bin multiplied by the hadronisation

p_T^b bin average (GeV)	$d\sigma/dp_T^b \pm$ stat. $\pm$ syst. (pb/GeV)
8.50	$106.04 \pm 12.49^{+18.71}_{-19.28}$
13.60	$13.73 \pm 2.56^{+3.26}_{-3.50}$
21.25	$1.50 \pm 0.23^{+0.35}_{-0.23}$

Table 7.5: Differential cross section for b-quark production as a function of p_T^b as measured in this analysis.

correction, $\frac{d\sigma^{NLO}(ep\to b(\bar{b})X)}{dp_T^{b(\bar{b})}}$ is the NLO prediction for b or $\bar{b}$ production with $|\eta^{b(\bar{b})}| < 2$ and the factor $1/2$ translates the cross section for b or $\bar{b}$ quark production to that for b quarks only.

The measurements are compared to an NLO QCD prediction and a prediction from LO k_T-factorisation approach [73]. The measurement in this thesis, given by the open triangles, is one of the most precise and is well described by both predictions.

Chapter 8

Conclusions

Beauty production identified through semi-leptonic decay into muons has been measured with the ZEUS detector in the kinematic range defined as: $Q^2 < 1\,\mathrm{GeV}^2$; $0.2 < y < 0.8$; $p_T^{j1,j2} > 7,6\,\mathrm{GeV}$; $|\eta^{j1,j2}| < 2.5$; $p_T^{\mu} > 2.5\,\mathrm{GeV}$; $-1.6 < \eta^{\mu} < 1.3$ with at least one muon being associated with a jet with $p_T^{j} > 6\,\mathrm{GeV}$. The muon impact parameter and muon p_T^{rel} methods were combined to extract the fraction of beauty events in the data sample. This thesis represents the first measurement of beauty production at ZEUS using lifetime information from the MVD.

The total visible cross section was measured as well as visible differential cross sections as a function of the transverse momenta and pseudorapidities of the muon and of the jet associated with the muon. The η^{μ} cross section was compared to the previous measurement [21]. This analysis confirms the previous result with similar statistical precision and different sources of systematic uncertainty. Also, it was possible to measure the cross section as a function of the muon transverse momentum to $p_T^{\mu} > 1.5\,\mathrm{GeV}$, a lower p_T^{μ} than in the previous muon-jet analysis [21]. The p_T^{μ} cross section agrees well with the NLO QCD prediction and does not confirm the excess observed by H1 [22] at low p_T^{μ}.

All results were compared to the Pythia MC model and to an NLO QCD prediction. The NLO QCD prediction describes the data well. The Pythia MC model also provides a good description of the shape of the distributions.

Beauty dijet angular-correlation cross sections were also measured. Separate measurements in direct-enriched and resolved-enriched regions were presented. Dijet correlations are particularly sensitve to higher order effects and so can be used to test the validity of fixed order calculations. The NLO QCD prediction describes the measured cross sections well.

Acknowledgements

There are a few people I would like to mention whose help and support throughout my studies were invaluable to me. Firstly, I would like to thank Matthew Wing for his guidance, I could not have hoped for a better supervisor. Mark Lancaster has always been a great mentor and friend. I value his opinion above all others; without him I would never have even started this. I would also like to thank John Loizides for his kindness and laughter. He taught me all the things I would have been afraid to ask anyone else. In doing this analysis, I worked closely with Silvia Miglioranzi and Monica Turcato; it was always a pleasure, I feel very lucky. I would also like to express my gratitute the following people for helpful chats, ideas and friendship: Tim Namsoo, James Ferrando, Dan Nicholass, Matthew Forrest and Homer Wolfe. I would especially like to thank Lily Asquith for being a wonderful friend who always knows what to do. Finally, I thank my family for all their encouragement and support in whatever I do.

Chapter 9

Appendix A: Purities, efficiencies and acceptance correction factors

This appendix contains plots of the purities, efficiencies and acceptance correction factors for all analysis bins as described in Section 7.1

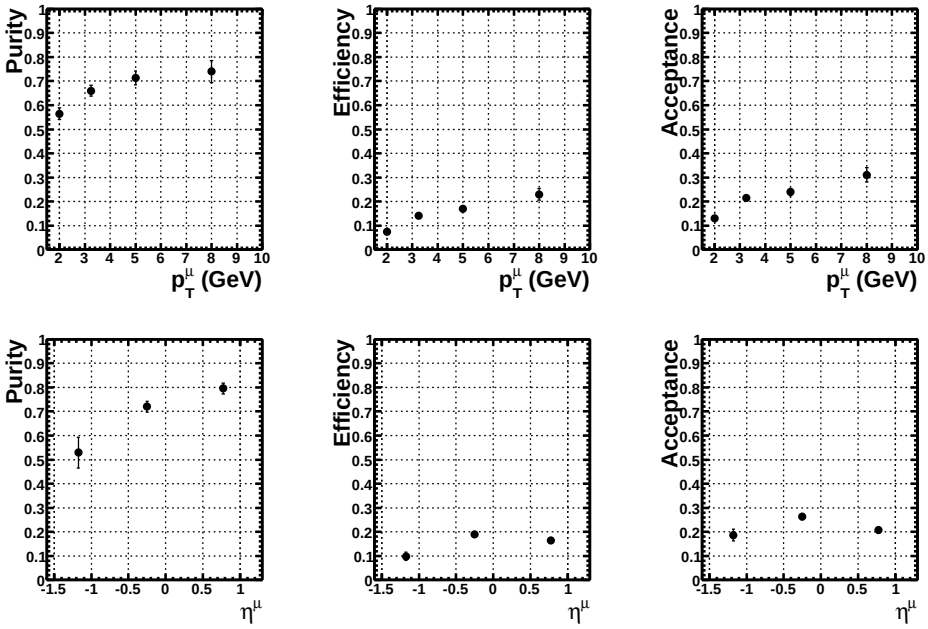

Figure 9.1: Purities, efficiencies and acceptance correction factors for the differential cross sections as functions of p_T^μ and η^μ.

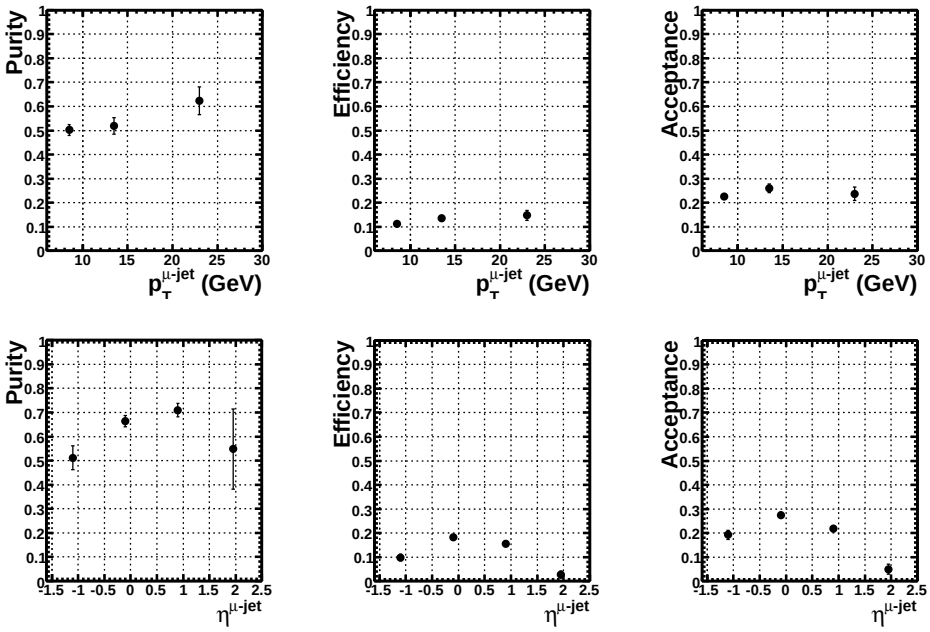

Figure 9.2: Purities, efficiencies and acceptance correction factors for the differential cross sections as functions of $p_T^{\mu-j}$ and $\eta^{\mu-j}$.

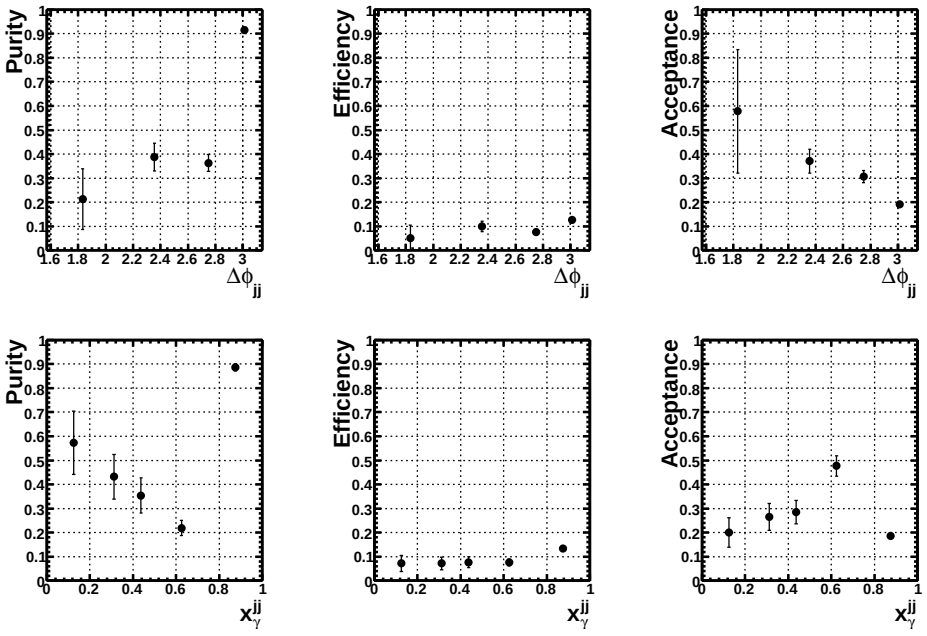

Figure 9.3: Purities, efficiencies and acceptance correction factors for the differential cross sections as functions of $\Delta\phi^{jj}$ and x_γ^{jj}.

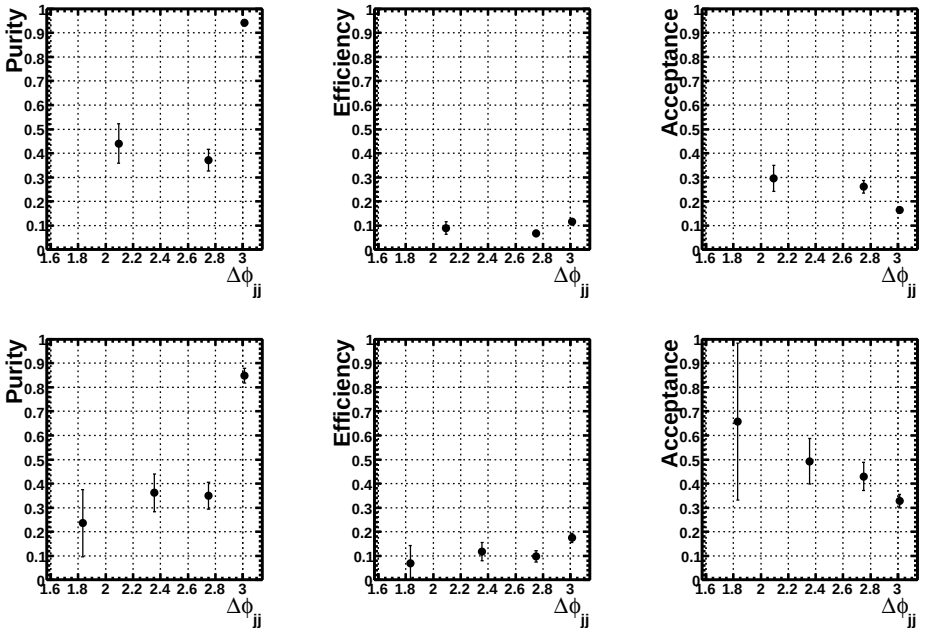

Figure 9.4: Purities, efficiencies and acceptance correction factors for the differential cross sections as functions of $\Delta\phi^{jj}$ for direct-enriched ($x_\gamma^{jj} > 0.75$) and resolved-enriched ($x_\gamma^{jj} < 0.75$) samples.

Chapter 10

Appendix B: Systematic uncertainites

This appendix contains plots of the fractional systematic uncertainties due to each variation described in Section 7.2. In all of the following plots, the solid line represents the size of the statistical uncertainty for each cross section.

Muon acceptance

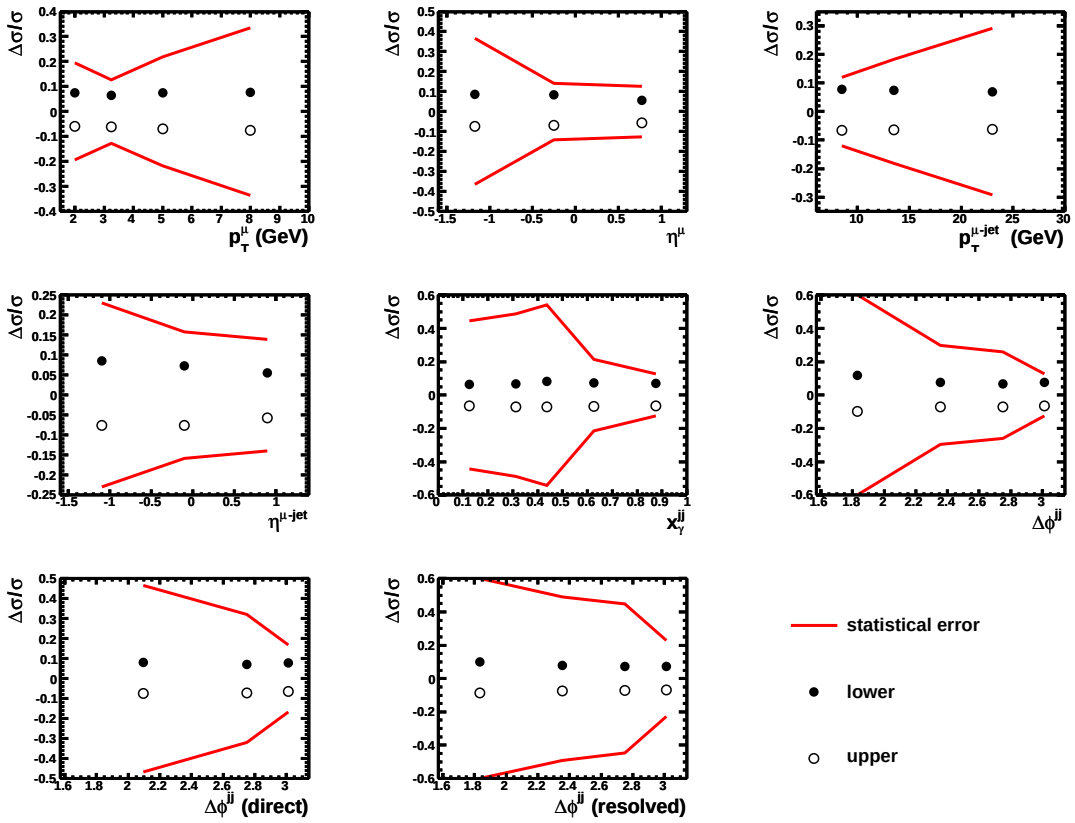

Figure 10.1: Fractional systematic uncertainty due to the muon acceptance.

Energy Scale

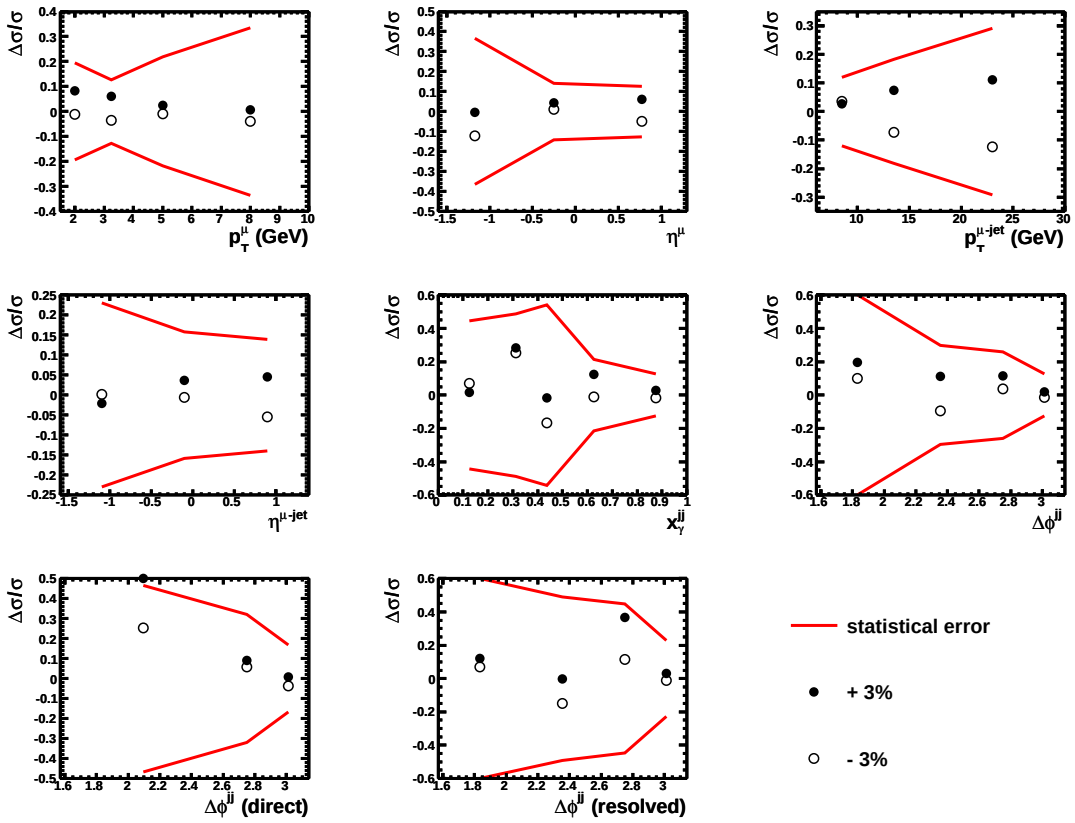

Figure 10.2: Fractional systematic uncertainty due to the energy scale.

MVD efficiency

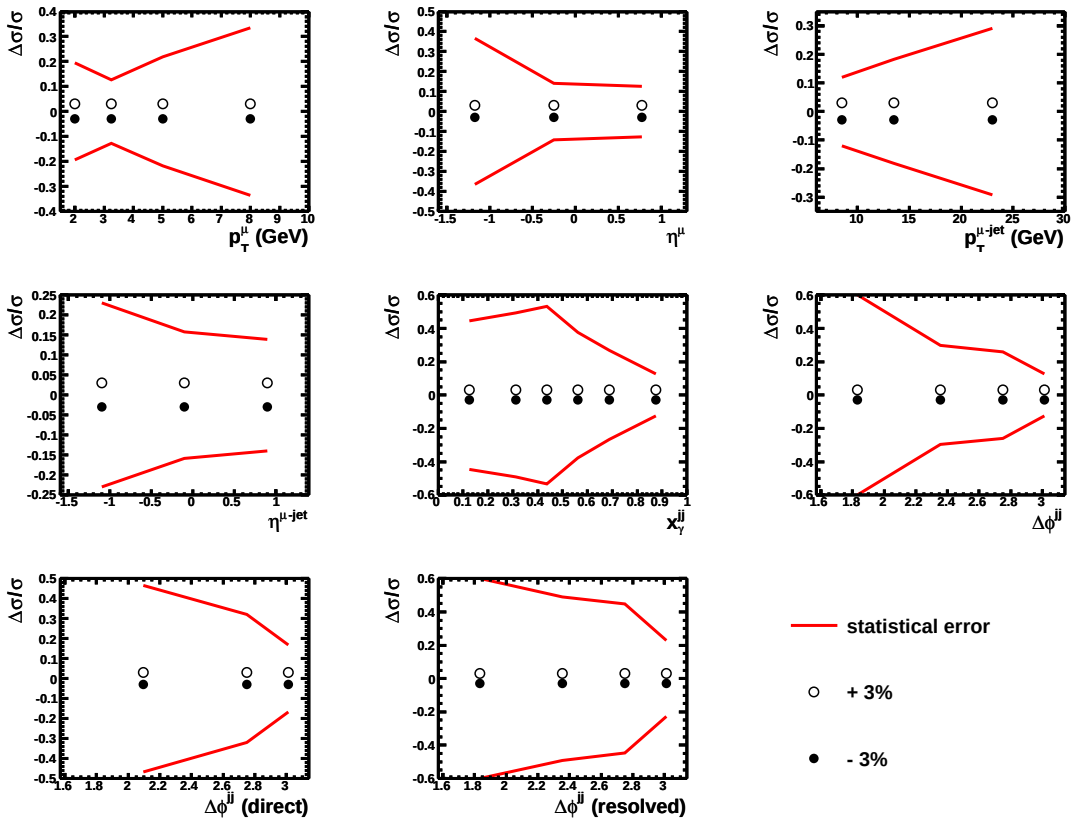

Figure 10.3: Fractional systematic uncertainty due to the MVD efficiency.

Dijet trigger efficiency

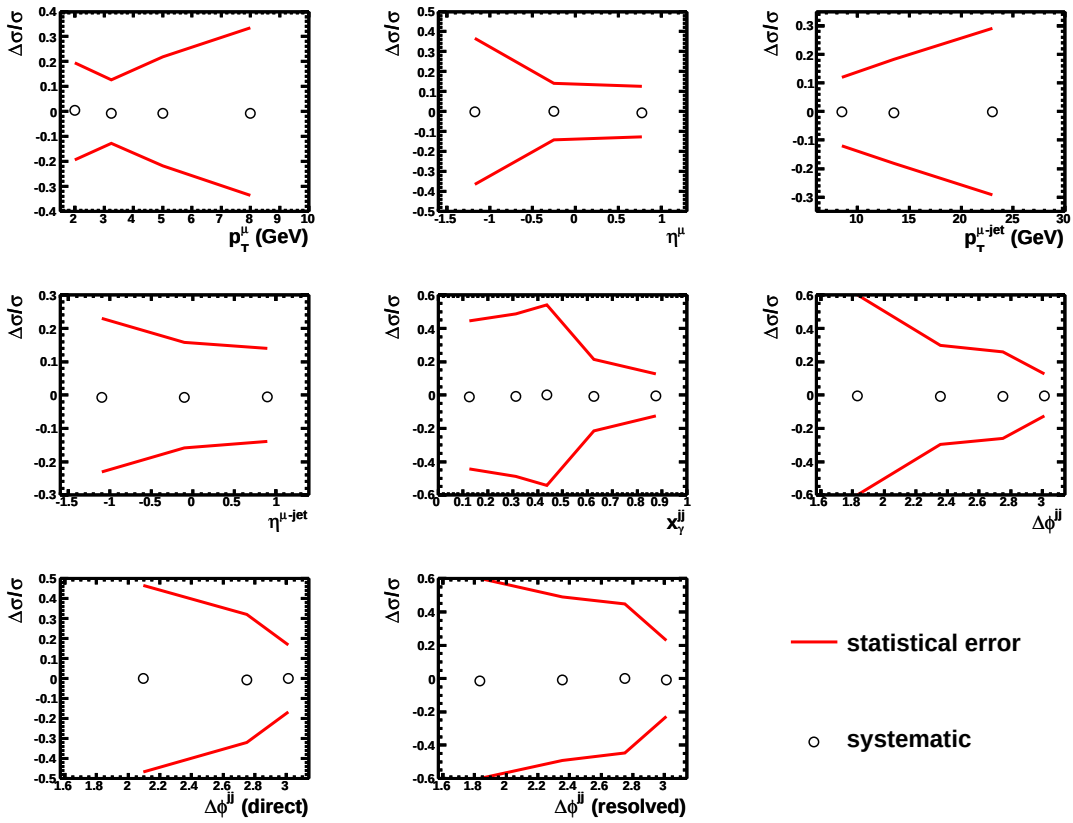

Figure 10.4: Fractional systematic uncertainty due to the dijet trigger efficiency.

η_μ MC description

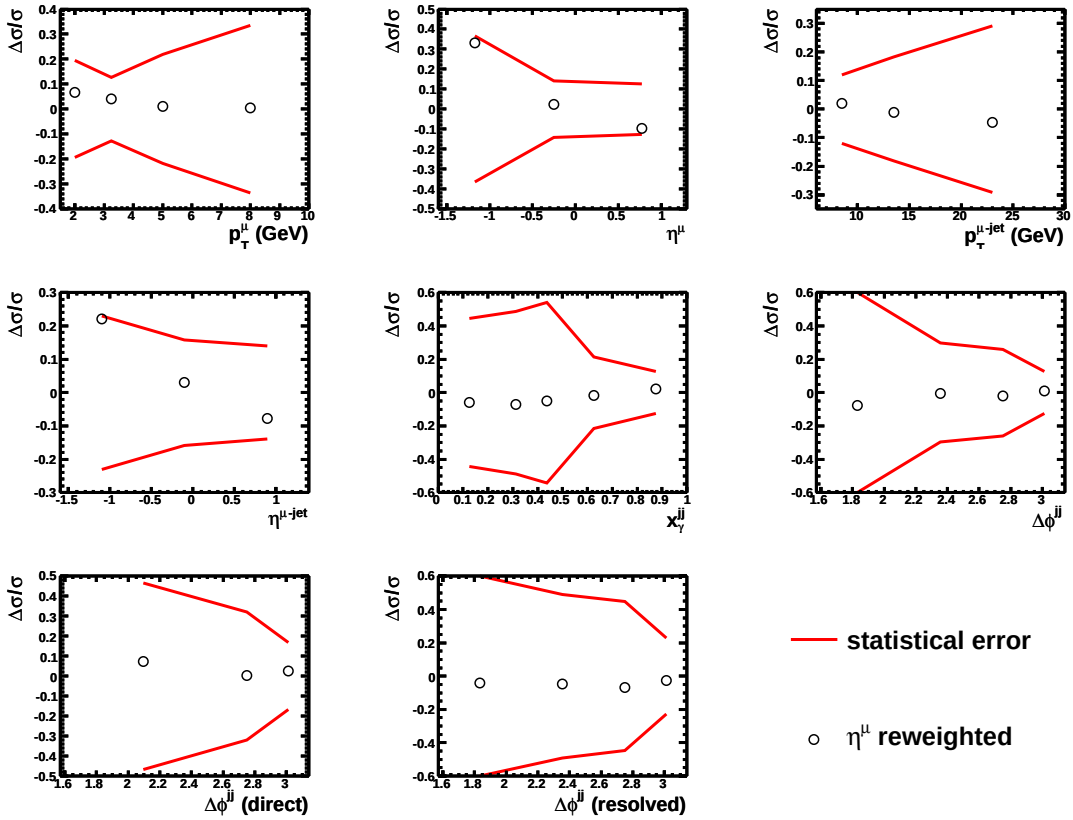

Figure 10.5: Fractional systematic uncertainty due to the η_μ MC description.

Impact parameter correction

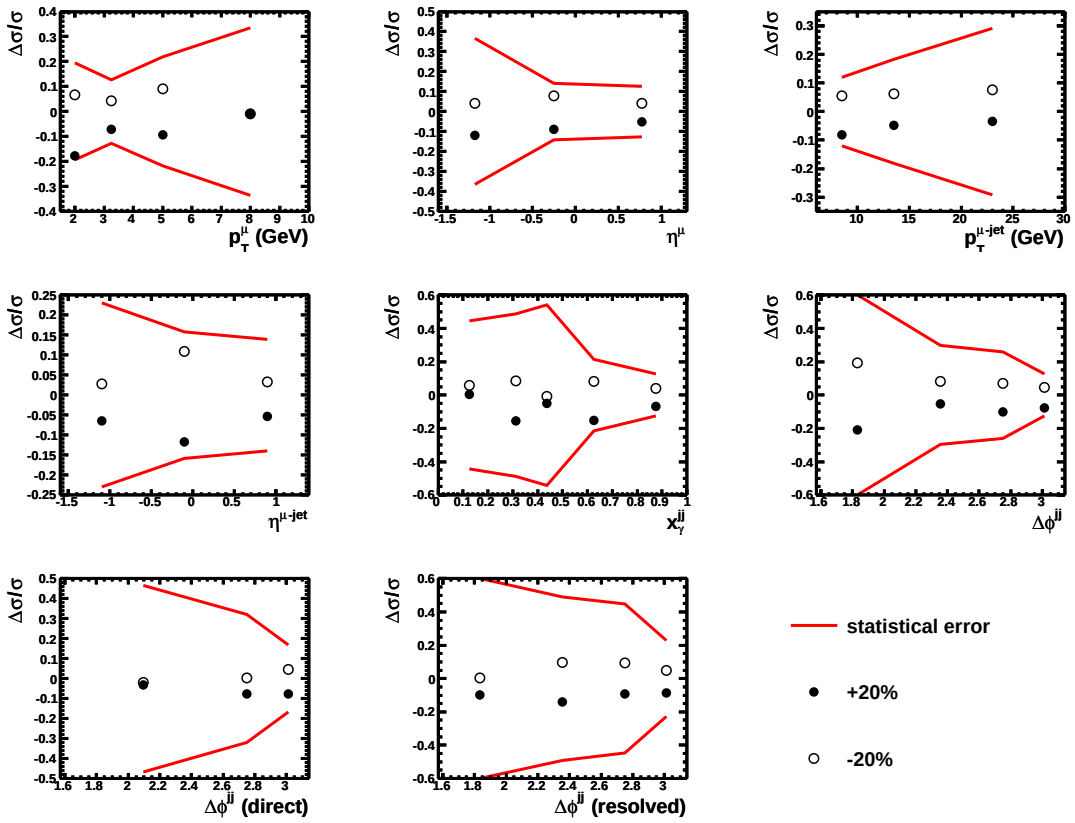

Figure 10.6: Fractional systematic uncertainty due to the impact parameter correction.

p_T^{rel} correction: varying the LF background correction

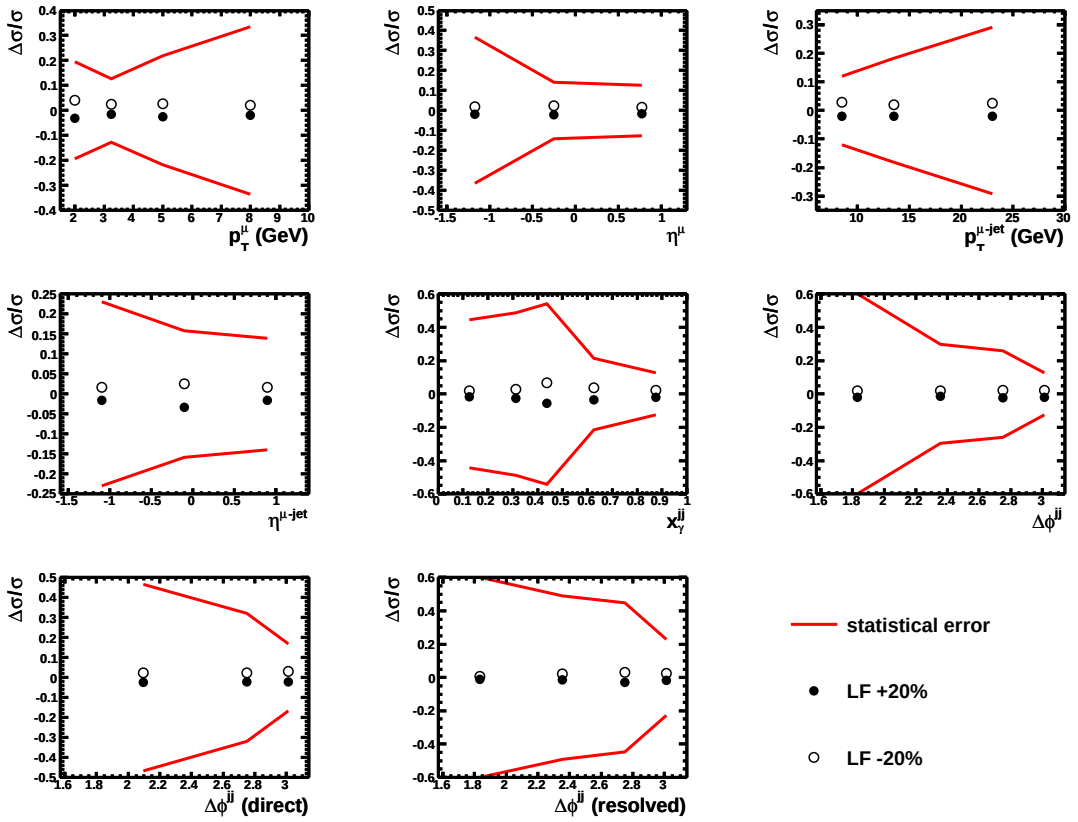

Figure 10.7: Fractional systematic uncertainty due to varying the light flavour background p_T^{rel} correction.

p_T^{rel} correction: varying the charm background correction

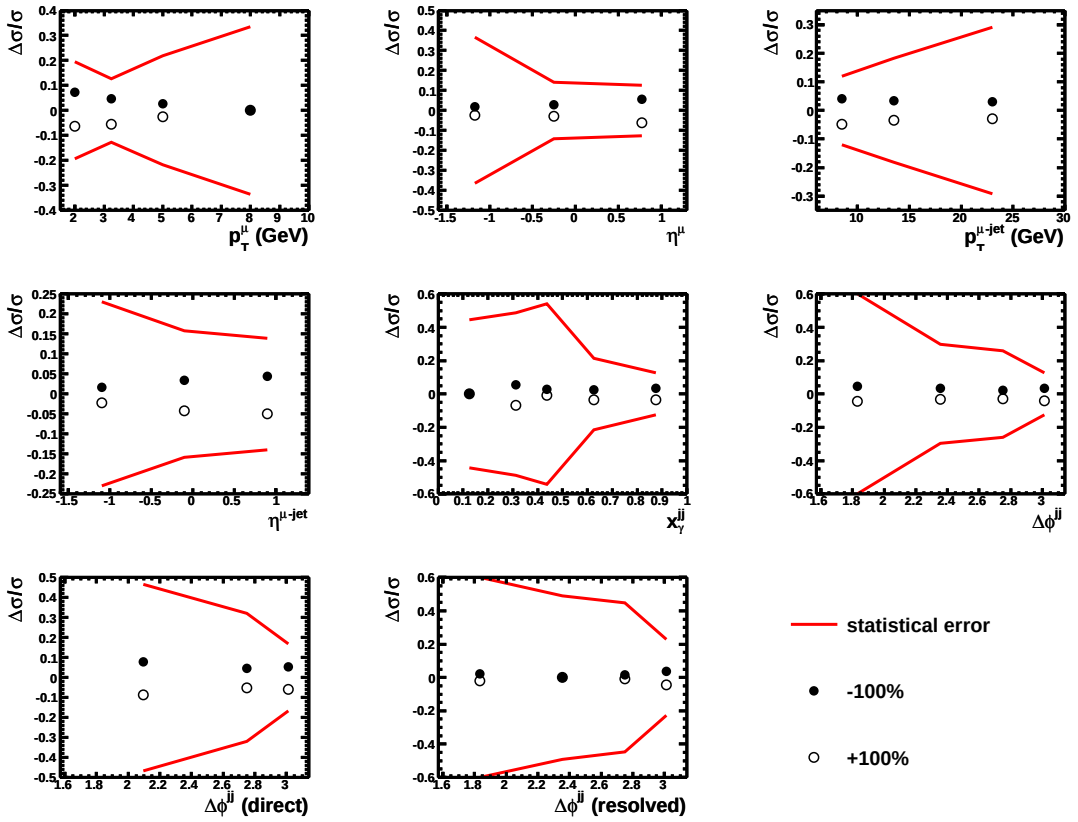

Figure 10.8: Fractional systematic uncertainty due to varying the charm background p_T^{rel} correction.

Physics process contribution

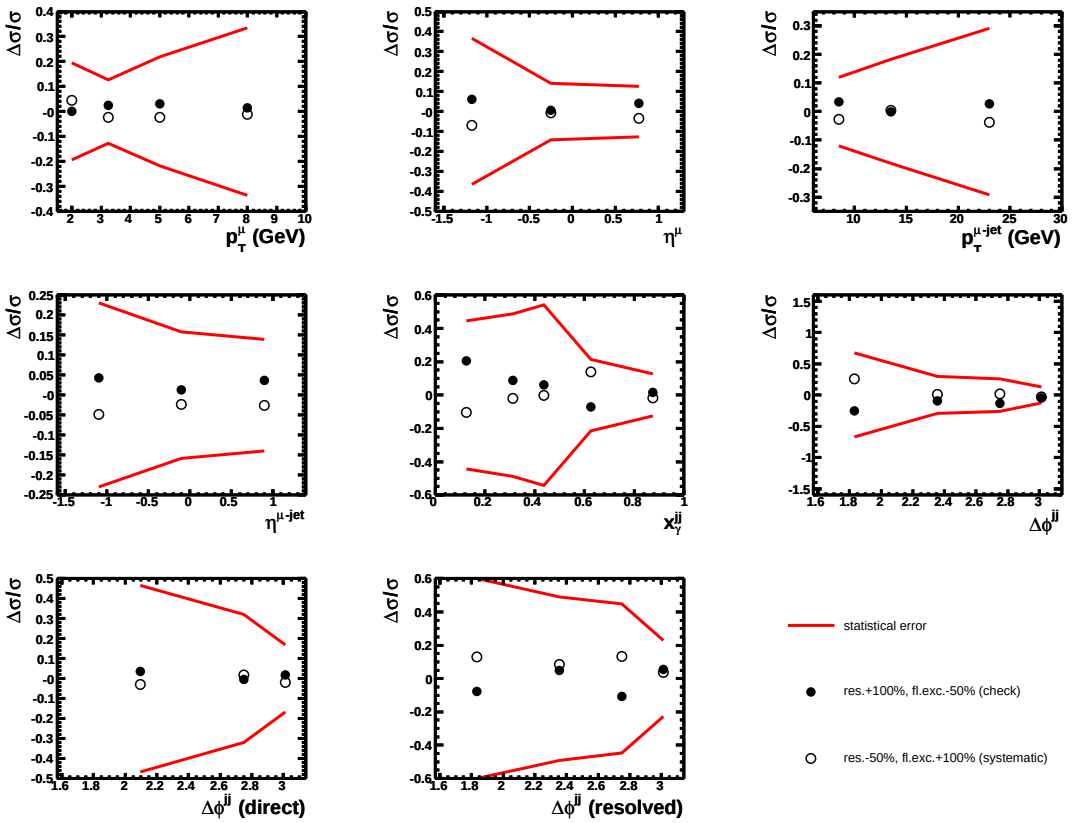

Figure 10.9: Fractional systematic uncertainty due to the variation of the flavour excitation processes by $+100\%/-50\%$ and the contribution of $gg \to b\bar{b}$, $q\bar{q} \to b\bar{b}$ events by $-50\%/+100\%$ simultaneously.

Physics process contribution

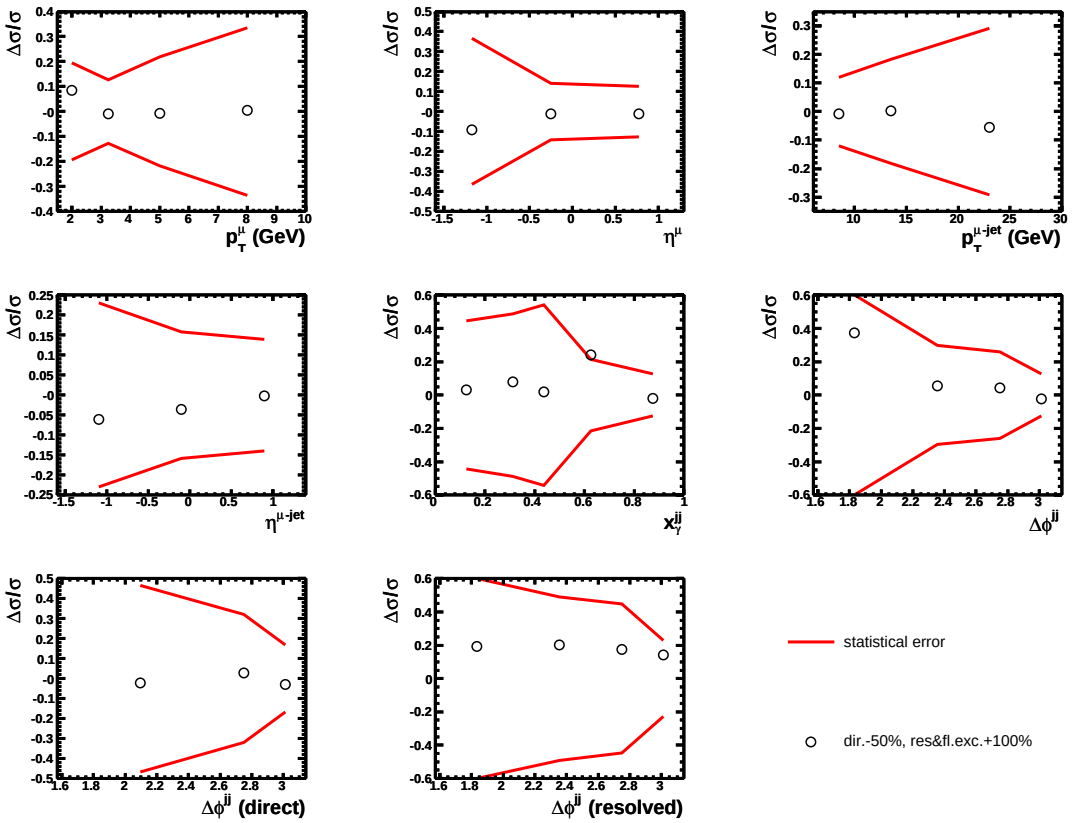

Figure 10.10: Fractional systematic uncertainty due to decreasing the contribution of $\gamma g \to b\bar{b}$ processes in PYTHIA by 20% and increasing all other processes by +100%.

Total systematic uncertainties

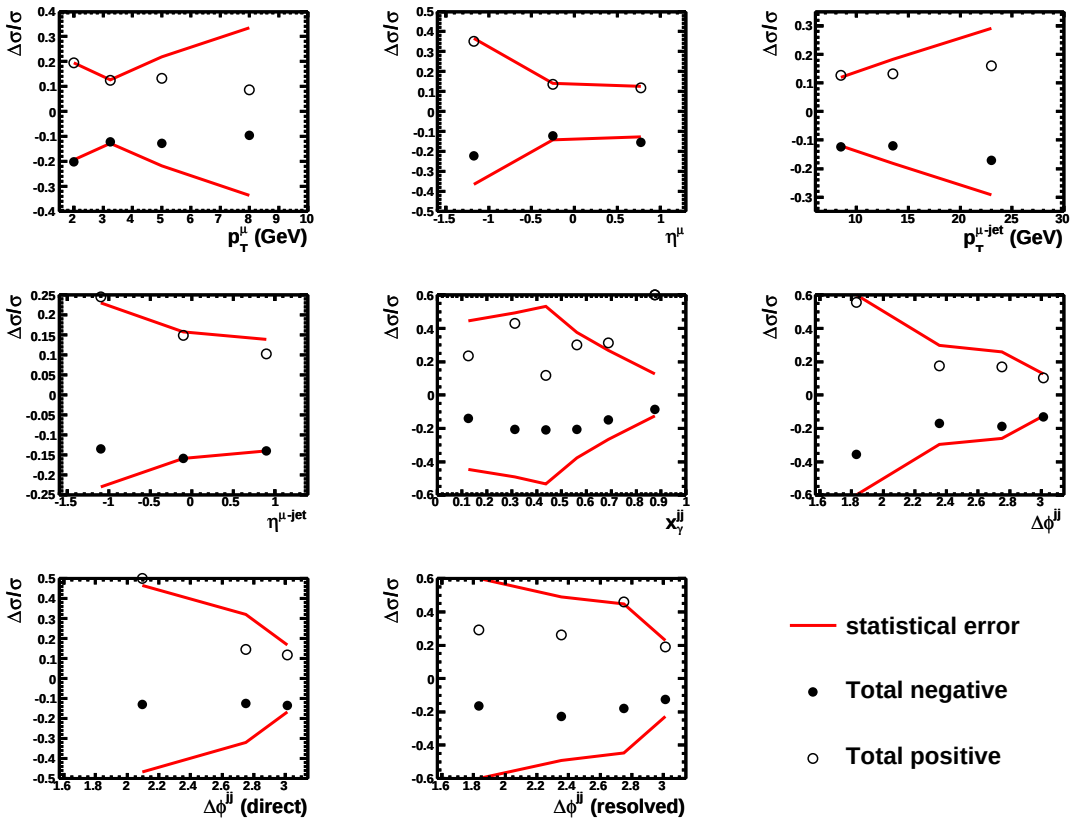

Figure 10.11: Total fractional systematic uncertainty found by summing the individual contributions in quadrature.

Bibliography

[1] ZEUS coll., S. Chekanov et al., JHEP **04**, 133 (2009).

[2] S. Miglioranzi, *Beauty photoproduction at HERA II with the ZEUS experiment*. Ph.D. Thesis, University College London, London, UK, 2006.

[3] S. Miglioranzi. Private Communication.

[4] J.D. Bjorken, Phys. Rev. **179**, 1547 (1969).

[5] G. Miller et al., Phys. Rev. **D 5**, 528 (1972).

[6] T. Eichten et al., Phys. Lett. **B 46**, 274 (1973).

[7] R. Brandelik et al., Phys. Lett. **B 86**, 243 (1979).

[8] ZEUS coll., M. Derrick et al., Phys. Lett. **B 316**, 412 (1993);
H1 coll., I. Abt et al., Nucl. Phys. **B 407**, 515 (1993).

[9] V.N. Gribov and L.N. Lipatov, Sov. J. Nucl. Phys. **15**, 438 (1972);
L.N. Lipatov, Sov. J. Nucl. Phys. **20**, 94 (1975);
Y.L. Dokshitzer, Sov. Phys. JETP **46**, 641 (1977);
G. Altarelli and G. Parisi, Nucl. Phys. **B 126**, 298 (1977).

[10] C.F. von Weizsäcker, Z. Phys. **88**, 612 (1934);
E.J. Williams, Phys. Rev. **45**, 729 (1934).

[11] J.F. Owens et al., Phys. Rev. **D 21**, 54 (1980).

[12] ZEUS coll., M. Derrick et al., Phys. Lett. **B 297**, 404 (1992);
H1 coll., T. Ahmed et al., Phys. Lett. **B 297**, 205 (1992).

[13] ZEUS coll., M. Derrick et al., Phys. Lett. **B 322**, 287 (1994).

[14] ZEUS coll., M. Derrick et al., Phys. Lett. **B 348**, 665 (1995).

[15] ZEUS coll., J. Breitweg et al., Eur. Phys. J. **C 1**, 109 (1998).

[16] R.K. Ellis and P. Nason, Nucl. Phys. **B 312**, 551 (1989).

[17] P. Nason, S. Dawson and R.K. Ellis, Nucl. Phys. **B 303**, 607 (1988).

[18] M.L. Mangano, P. Nason and G. Ridolfi, Nucl. Phys. **B 373**, 295 (1992).

[19] S. Frixione et al., Nucl. Phys. **B 412**, 225 (1994).

[20] M. Cacciari and M. Greco, Phys. Rev. **D 55**, 7134 (1997).

[21] ZEUS coll., S. Chekanov et al., Phys. Rev. **D 70**, 12008 (2004).

[22] H1 coll., A. Aktas et al., Eur. Phys. J. **C 41**, 453 (2005).

[23] ZEUS coll., S. Chekanov et al., Phys. Rev. **D 78**, 072001 (2008).

[24] ZEUS coll., J. Breitweg et al., Eur. Phys. J. **C 18**, 625 (2001).

[25] H1 coll., A .Aktas et al., Eur. Phys. J. **C 47**, 597 (2006).

[26] UA1 coll., C. Albajar et al., Phys. Lett. **B 186**, 237 (1987);
UA1 coll., C. Albajar et al., Phys. Lett. **B 213**, 405 (1988);
UA1 coll., C. Albajar et al., Phys. Lett. **B 256**, 121 (1991);
Erratum-ibid., Phys. Lett. **B 262**, 497 (1991);
UA1 coll., C. Albajar et al., Z. Phys. **C 61**, 41 (1994).

[27] P. Nason, S. Dawson and R.K. Ellis, Nucl. Phys. **B 303**, 607 (1988);
P. Nason, S. Dawson and R.K. Ellis, Nucl. Phys. **B 327**, 49 (1989).

[28] CDF coll., F. Abe et al., Phys. Rev. Lett. **71**, 500 (1993);
CDF coll., F. Abe et al., Phys. Rev. Lett. **71**, 2396 (1993);
CDF coll., F. Abe et al., Phys. Rev. Lett. **75**, 1451 (1995);
CDF coll., F. Abe et al., Phys. Rev. **D 53**, 1051 (1996);
CDF coll., F. Abe et al., Phys. Rev. **D 55**, 2546 (1997);
CDF coll., D. Acosta et al., Phys. Rev. **D 65**, 052005 (2002);
CDF coll., D. Acosta et al., Phys. Rev. **D 66**, 032002 (2002).

[29] DØ coll., S. Abachi et al., Phys. Rev. Lett. **74**, 3548 (1995);
DØ coll., S. Abbott et al., Phys. Lett. **B 487**, 264 (2000);
DØ coll., S. Abbott et al., Phys. Rev. Lett. **84**, 5478 (2000);
DØ coll., S. Abbott et al., Phys. Rev. Lett. **85**, 5068 (2000).

[30] M. L. Mangano, AIP Conf. Proc. **753**, 247 (2005).

[31] CDF coll., D. Acosta et al., Phys. Rev. **D 71**, 032001 (2005);
CDF coll., D. Acosta et al., Phys. Rev. **D 71**, 092001 (2005);
CDF coll., T. Aaltonen et al., Phys. Rev. **D 77**, 072004 (2008).

[32] M. Cacciari et al., JHEP **0407**, 033 (2004).

[33] S. Frixione, P. Nason, and B.R. Webber, JHEP **0308**, 007 (2003).

[34] L3 coll., M. Acciarri et al., Phys. Lett. **B 503**, 10 (2001);
L3 coll., P. Achard et al., Phys. Lett. **B 619**, 71 (2005).

[35] M. Drees, M. Kramer, J. Zunft and P.M. Zerwas, Phys. Lett. **B 306**, 371 (1993).

[36] ALEPH coll., S. Schael et al., JHEP **0709**, 102 (2007).

[37] ZEUS coll., S. Chekanov et al., Nucl. Phys. **B 729**, 492 (2005).

[38] ZEUS coll., S. Chekanov et al., Phys. Rev. **D 76**, 072011 (2007).

[39] G. Ingelman, A. De Roeck and R. Klanner, *Future Physics at HERA*. Workshop proceedings, 1995-1996.

[40] ZEUS Coll. U. Holm (ed.), *The ZEUS Detector. Status Report.* (unpublished), 1993, available on `http://www-zeus.desy.de/bluebook/bluebook.html`.

[41] A. Polini et al., Nucl. Instrum. Meth. **A 581**, 656 (2007).

[42] N. Harnew et al., Nucl. Instrum. Meth. **A 279**, 290 (1989);
B. Foster et al., Nucl. Phys. Proc. Suppl. **B 32**, 181 (1993);
B. Foster et al., Nucl. Instrum. Meth. **A 338**, 254 (1994).

[43] ZEUS Calorimeter Group Coll., A. Andresen et al., Nucl. Instrum. Meth. **A 309**, 101 (1991).

[44] J. Repond et al., *Design And Construction Of The Zeus Barrel Calorimeter (Presented at Int. Conf. on Calorimetry in High Energy Physics, Batavia, IL.)*, 1990, available on `http://www.slac.stanford.edu/spires/find/hep/www?r=anl-hep-cp-90-123 (SPIRES entry)`. ANL-HEP-CP-90-123.

[45] D. Acosta et al., Nucl. Instrum. Meth. **A 354**, 296 (1995).

[46] G. Abbiendi et al., Nucl. Instrum. Meth. **A 333**, 342 (1993).

[47] H. Bethe and W. Heitler, Proc. Roy. Soc. Lond. **A 146**, 83 (1934).

[48] J. Andruszkow et al., Preprint DESY-92-066 (1992);
M. Derrick et al., Z. Phys. **C 63**, 391 (1994);
J. Andruszkow et al., Acta Phys. Pol. **B 32**, 2025 (2001).

[49] W.H. Smith, K. Tokushuku and L.W. Wiggers, *Proc. Computing in High-Energy Physics (CHEP), Annecy, France, Sept. 1992*, C. Verkerk and W. Wojcik (eds.), p. 222. CERN, Geneva, Switzerland (1992). Also in preprint DESY 92-150B;
P.D. Allfrey et al., Nucl. Inst. Meth. **A 580**, 1257 (2007).

[50] G.F. Hartner, *VCTRAK Briefing: Program and Math* (unpublished). ZEUS-98-058, 1998;
G.F. Hartner et al., *VCTRAK (3.07/04): Offline Output Information* (unpublished). ZEUS-97-064, 1997.

[51] E. Maddox, *Study of heavy quark production at HERA using the ZEUS microvertex detector*. Ph.D. Thesis, NIKHEF, Amsterdam, Netherlands, 2004.

[52] P. Billoir, R. Fruhwirth and M. Regler, Nucl. Instrum. Meth. **A 241**, 115 (1985).

[53] D. Nicholass, *The study of D+- and D0 meson production in deep inelastic scattering at HERA II with the ZEUS detector*. Ph.D. Thesis, University College London, London, United Kingdom, 2008. Unpublished.

[54] R. Mankel, *How wide is the HERA II beam spot* (unpublished). Internal ZEUS presentation, 2006.

[55] G. Abbiendi, *Global Tracking of Muons in the Barrel and Rear Region* (unpublished). ZEUS-99-063, internal ZEUS Note, 1999.

[56] V. Innocente, M. Maire and E. Nagy, *MC91: Workshop on Detector and Event Simulation in High Energy physics*, K. Bos and B. van Eijk (eds.), pp. 58–78. Amsterdam, NIKHEF (1991).

[57] V. Chiochia, *Measurement of Beauty Quark Production in Deep Inelastic Scattering at HERA*. Ph.D. Thesis, University of Hamburg, Report DESY-THESIS-2003-031, 2003.

[58] M. Turcato, *Measurement of beauty photoproduction at HERA*. Ph.D. Thesis, Università degli Studi di Padova, Report DESY-THESIS-2003-039, 2003.

[59] J.E. Huth et al., *Research Directions for the Decade. Proceedings of Summer Study on High Energy Physics, 1990*, E.L. Berger (ed.), p. 134. World Scientific (1992).

[60] S. Catani, Y.L. Dokshitzer and B.R. Webber, Phys. Lett. **B 285**, 291 (1992).

[61] S. Catani, Y.L. Dokshitzer, M.H. Seymour and B.R. Webber, Nucl. Phys. **B 406**, 187 (1993).

[62] W.B. Kilgore and W.T. Giele, Phys. Rev. **D 55**, 7183 (1997).

[63] S.D. Ellis and D.E. Soper, Phys. Rev. **D 48**, 3160 (1993).

[64] G. Abbiendi et al., *Observation of* $J/\Psi -> \mu^+\mu^-$ *in the first* 274 nb^{-1} *of 1993 run* (unpublished). ZEUS-93-120, 1993.

[65] H. Abramowicz, A. Caldwell and R. Sinkus, Nucl. Instrum. Meth. **A 365**, 508 (1995).

[66] F. Jacquet and A. Blondel, *Proceedings of the Study for an ep Facility for Europe*, U. Amaldi (ed.), p. 391. Hamburg, Germany (1979). Also in preprint DESY 79/48.

[67] CTEQ coll., H.L. Lai et al., Eur. Phys. J. **C 12**, 375 (2000).

[68] M. Glück, E. Reya and A. Vogt, Phys. Rev. **D 46**, 1973 (1992).

[69] C. Peterson et al., Phys. Rev. **D 27**, 105 (1983).

[70] Hagiwara, Kaoru et al., Phys. Rev. **D 66**, 010001 (2002).

[71] A. Longhin, *Measurement of Beauty Production at HERA with* $D*+\mu$ *Tag.* Ph.D. Thesis, Universita di Padova, Report DESY-THESIS-2004-050, 2003.

[72] K. Abe et al., Phys. Lett. **B 547**, 181 (2002);
B. Aubert et al., Phys. Rev. **D 67**, 031101 (2003).

[73] A.V. Lipatov and N.P. Zotov, Phys. Rev. **D 73**, 114018 (2006).